

RATCHETED RINGS FOR LEIDENFROST SELF-PROPULSION AND DROPLET MIXING

by

Guanqi Wang

A thesis presented for the degree of

Doctor of Philosophy



School of Engineering
Newcastle University

April 2022

Abstract

Liquid droplets deposited on a saw-tooth ratcheted surface will move spontaneously in a unique direction attaining a reasonable terminal velocity (typically, 10 cm/s) provided that the droplets are in the Leidenfrost state. Here, the droplet levitates above the surface on top of a vapour cushion produced by the evaporating liquid. This work aims to explore the potentials of the phenomenon in the field of droplet mixing. New ratcheted surfaces in the shape of a ring were manufactured to constrain empirical studies in a shorter footprint (enabling more conditions to be studied). Experiments were also used to gain new insights into the mechanism, with the purpose of superseding the limited scaling analysis previously given in the literature.

(1) A high-speed camera was used to capture the droplet motion (*e.g.* droplet velocity) and droplet mixing process (*e.g.* colour distribution). A custom programme in MATLAB refined these images to isolate a region of interest (ROI) corresponding to the droplet field. The efficiency of the programme was tested by comparing the results against time-consuming manual measurements performed in ImageJ (Fiji); differences of just 0.75–3.82% were observed.

(2) A new analytical model was developed on the basis of a Leidenfrost droplet, where the deformable nature of the liquid is taken into account for the first time. Droplet deformation was theoretically analysed through a pressure balance, by considering the dynamic pressure (produced by the fast droplet motion), the static hydrodynamic pressure (produced by gravity), and the Laplace pressure (produced by the surface tension). The model indicates that the acceleration and driving force are sensitive to the deformation of the liquid and the geometry of the ratcheted surface (height and length of the ratchets), but shows little dependence on the droplet size and surface temperature.

(3) Four aluminium ratcheted ring designs were employed to study the self-propelled droplets, in a difference of ratchet parameters, ratchet shape and diameter scale. Meanwhile, the droplet deformation around the ratchets was observed via a microscopic lens. These measurements were used to validate the model with respect to different ratchet parameters, surface temperatures (between 300°C and 400°C) and droplet sizes (from 30 μL to 1500 μL).

The model fitted the experimental measurements better than previous reports, having a maximum of 23% deviation. Additionally, it was found that the annular ring design enabled higher terminal velocities than other linear ratchet designs in the literature, up to 0.39 m/s, which is potentially beneficial to energy harvesting and flow chemistry applications.

(4) The four ratcheted rings and a flat substrate were then used to study mixing inside the droplets under the Leidenfrost state. Measurements were collected for a range of different droplet volumes (from 400 μ L to 1200 μ L) and surface temperatures (from 300 $^{\circ}$ C to 400 $^{\circ}$ C). The result shows that it takes a maximum of 5 s for mixing to reach completion under the self-propulsion Leidenfrost state compared to several minutes for the room temperature diffusion benchmark. Therefore, the mixing efficiency has been significantly improved using these Leidenfrost propulsion devices.

Keywords: Leidenfrost effect; image analysis; droplet self-propulsion; analytical model; liquid deformation; mixing

Acknowledgement

I would first like to express my gratitude to Dr Vladimir Zivkovic, Dr Jonathan McDonough and Dr Steven Wang. I could not have approached those targets without the guidance of my supervisory team, either the completion of the project or the publications we have ever tried. Our discussions have always been the moments of stimulation that promoted my understanding, and in the meantime, I appreciate their encouragement and patience along the way before I finally grow up as a junior researcher.

The financial support from China Scholarship Council to carry out the research is thankfully acknowledged.

As an experimenter, I wish to thank the technical support from Iain Strong, Eric Gray, Rob Dixon, Paul Sterling, Ashley Craig and Kevin Brown, without whom my experiment would not have run as smoothly as it did.

Special thanks to my defence committee who generously provided knowledge and expertise.

My appreciation goes out to my officemates, housemates and friends for the fun and pleasure we had over the past four years. Thank you to the cleaning lady Lisa who has always brought the most cheerful greetings and shared her lovely little gifts.

Lastly, thank you to my family for their unconditional support.

List of Publications

Wang, G, McDonough, JR, Zivkovic, V, Long, T, & Wang, S 2021, '**From Thermal Energy to Kinetic Energy: Droplet Motion Triggered by the Leidenfrost Effect**', *Advanced Materials Interfaces*, vol. 8, no. 2, 2001249. <https://doi.org/10.1002/admi.202001249>

Wang, G, McDonough, J, Zivkovic, V, Long, T, Wang, Z & Wang, S 2022, '**Terminal Velocities of a Deformed Leidenfrost Liquid: Experiments and Self-Propulsion Model**', *Physical Review Fluids*, vol. 7, no. 3, 033602. <https://doi.org/10.1103/PhysRevFluids.7.033602>

Wang, G, McDonough, J, Zivkovic, V, Long, T & Wang, S, '**Droplet Mixers under the Leidenfrost State**', *In preparation*

Table of Contents

Abstract	i
Acknowledgement	iii
List of Publications	v
Table of Contents	vii
List of Figures	xi
List of Tables	xvii
Nomenclature	xix
Chapter 1. Introduction	1
1.1 Self-Propelled Leidenfrost Droplets	1
1.2 Areas for Further Research and Problem Statement	3
1.3 Research Aims and Objectives	4
1.4 Novelty	5
Chapter 2. Literature Review	7
2.1 Wetting Theory	9
2.2 Leidenfrost Dynamics	10
<i>2.2.1 Levitation on Smooth Surfaces</i>	<i>10</i>
<i>2.2.2 Special Dynamics</i>	<i>12</i>
2.3 Leidenfrost Self-Propulsion on Ratchet Surfaces	13
<i>2.3.1 Enhanced/Unconventional Propulsion at Micro and Nano Scales</i>	<i>15</i>
<i>2.3.2 The Cold Leidenfrost Self-Propulsion Regime</i>	<i>16</i>
2.4 Solid Leidenfrost Phases	17
2.5 Current Theoretical Advancement	19
<i>2.5.1 Initial Proposals by Linke</i>	<i>19</i>
<i>2.5.2 Jet-thrust Momentum Conversion and Corresponding Models</i>	<i>20</i>
<i>2.5.3 Viscous Stress Induced by Rectified Vapour Flow</i>	<i>22</i>
<i>2.5.4 Additional Considerations Based on Numerical Analysis</i>	<i>23</i>
<i>2.5.5 Friction</i>	<i>24</i>
2.6 Potential Application Proposals	26
<i>2.6.1 Levitated Microreactors</i>	<i>26</i>
<i>2.6.2 Frictionless Transport</i>	<i>26</i>
<i>2.6.3 Leidenfrost Mixer</i>	<i>28</i>

2.6.4 <i>Energy Harvesting</i>	28
2.7 Chapter Summary and Outlook	28
Chapter 3. Methodology	31
3.1 Design of Devices	31
3.2 Droplet Motion Study	32
3.2.1 <i>Experimental Procedure</i>	32
3.2.2 <i>Automatic Droplet Motion Detection</i>	33
3.2.3 <i>Programme Validation</i>	40
3.3 Droplet Mixing Study	42
3.3.1 <i>Experimental Procedure</i>	42
3.3.2 <i>Automatic Colour Detection</i>	44
3.3.3 <i>Program Validation</i>	46
3.3.3 <i>Mixing Time Definition</i>	46
3.4 Chapter Summary	48
Chapter 4. Novel Analytical Model for the Leidenfrost Self-Propulsion	49
4.1 Dynamics for Propulsion	49
4.1.1 <i>Analysis in a Model</i>	49
4.1.2 <i>Reynolds Number Justification</i>	58
4.1.3 <i>Model Validation using Literature Data</i>	59
4.2 Terminal Velocity Prediction	59
4.3 Chapter Summary	60
Chapter 5. Experimental Observations of Leidenfrost Droplets on Ratcheted Rings	63
5.1 Shapes of Self-Propelling Droplets	63
5.1.1 <i>Modified Ring</i>	63
5.1.2 <i>Droplet Height</i>	64
5.1.3 <i>Droplet Width</i>	65
5.1.4 <i>Droplet Deformation</i>	68
5.1.5 <i>Volume Calibration</i>	69
5.2 Dynamics	70
5.2.1 <i>Droplet Velocity</i>	70
5.2.3 <i>Droplet Motion and Model Validation</i>	73
5.3 Energy Conversion Efficiency	80
5.3.1 <i>Latent Heat of the Phase Transition</i>	80

5.3.2 <i>Viscous Dissipation</i>	81
5.4 Chapter Summary	84
Chapter 6. Droplet Mixing under Leidenfrost State	85
6.1 Assumptions and Preliminary Mixing Analysis	86
6.2 Mixing Time Results	89
6.2.1 <i>Diffusion at Room Temperature</i>	89
6.2.2 <i>Convection on ratcheted rings</i>	91
6.2.3 <i>Convection on a Flat Surface</i>	96
6.3 Energy Loss by the Deformed Liquid	99
6.4 Chapter Conclusion	100
Chapter 7 Conclusions and Future Work	101
7.1 Overall Aims	101
7.2 Main Outcomes	101
7.2.1 <i>A General Model for Leidenfrost Self-Propulsion</i>	101
7.2.2 <i>Ratcheted Rings for Leidenfrost Self-Propulsion</i>	102
7.2.3 <i>Droplet Mixing under the Leidenfrost State</i>	102
7.2.4 <i>Automated Image Processing</i>	103
7.3 Further Work	103
References	105
Appendix A. Image Processing	115
Appendix B. Droplet Detection	119
Appendix C. Coloured Droplet Detection	121
Appendix D. Function Derivation (eq. 5.6)	123
Appendix E. Work Calculation	125

List of Figures

<i>Figure 1.1 – A Leidenfrost heat engine. (a) and (b) are the initial design of the heat engine. (c) and (d) improved the design to a continuously operation system. Panels (a) and (b) are taken from [31]. Panels (c) and (d) are taken from [32].</i>	3
<i>Figure 2.1 – ‘Passive’ methods to induce liquid motion (a) Droplet trampolining at Leidenfrost state [21], (b) Leidenfrost droplet motion on a thermal gradient [23], (c) Leidenfrost self-propulsion on a heated ratcheted surface [24], (d) Liquid transport on a ratcheted surface [56, 58, 59]</i>	8
<i>Figure 2.2 – Ideal wetting of a drop on a solid surface. Figure reproduced from [66].</i>	9
<i>Figure 2.3 – (a) Chimneys of vapour induce the Rayleigh-Taylor instability for large Leidenfrost droplets (Biance et al. [15]), (b) Star-shaped droplet oscillation. Figure taken from Ma et al. [25]</i>	11
<i>Figure 2.4 – Capillary Leidenfrost droplets self-propel on a smooth surface [70].</i>	11
<i>Figure 2.5 – Hydrogel trampolining. (a) The hydrogel gradually stopped bouncing on the cold surface, where the audio signal (bottom) did not reflect any evaporation. (b) On a heated surface, the restitution coefficient is maintained as 1 or even above because of the energy injection during evaporation, which kept the hydrogel bouncing in a steam engine way for a considerable time. Figure taken from Scott et al. [10]</i>	12
<i>Figure 2.6 – The report by Linke et al. [24] (a) High-resolution photograph of the liquid-vapour-solid interface, (b) Schematic of the directed vapour flow driven by the pressure gradient $\Delta p = p_A - p_B$, (c) A nucleate boiling event in low temperature regime. Evaporation was enhanced to further improve droplet motion, (d) Typical velocity trend for a self-propelling droplet. Measurement was stable in high temperature regime (main panel) but fluctuated in low temperature regime (inset)</i>	13
<i>Figure 2.7 – Expanded patterns for Leidenfrost self-propulsion. Panel a taken from Soto et al. [82]. Panel b taken from Cousins et al. [43]. Panel c taken from Dupeux et al. [83]</i>	14
<i>Figure 2.8 – Contact angle hysteresis from two kinds of hydrophobic nanostructure (A) and (B) are the SEM (scanning electron microscopy) images of the two. (A) A brass surface coated by Glaco solution. (B) A silicon surface decorated with nanocones and coated by fluorosilanes. (C) Contact angle hysteresis $\Delta \cos \theta$ from the two surfaces. Figure taken from Bourrienne et al. [95].</i>	16

<i>Figure 2.9 – A self-rotation device made of two Leidenfrost solid bodies. An off-centred rod creates the asymmetry of the system to induce solid motion in opposite directions. Figure taken from Dupeux et al. [83].....</i>	<i>17</i>
<i>Figure 2.10 – Design of a frictionless Leidenfrost cart. Figure taken from Ali et al. [101].....</i>	<i>18</i>
<i>Figure 2.11 – Direct force measurement via a glass fibre, deflecting the fibre by a distance of δ. Figure taken from Lagubeau et al. [104].....</i>	<i>21</i>
<i>Figure 2.12 – Vapour flow (arrow direction) rectified by saw-tooth ratchets, via tracer measurement. Figure taken from Dupeux et al. [42].....</i>	<i>22</i>
<i>Figure 2.13 – Directed gas flow (blue arrow in the right-hand panel) induced by creep flow. This mechanism does not rely on the droplet evaporation in the left-hand panel. Figure taken from Würger [80].....</i>	<i>24</i>
<i>Figure 2.14 – Crenelated surface stops a moving droplet. Figure taken from Dupeux et al. [100].....</i>	<i>25</i>
<i>Figure 2.15 Effect of charge separation in a Leidenfrost droplet [108].....</i>	<i>26</i>
<i>Figure 2.16 – A Leidenfrost side-shooter designed by Sugioka et al. [114] 1 Water droplet 2 Hydrophobic substrate 3 Thin-film heater 4a&b Surface tension at the corner 5&6 Net forces acting on the droplet.....</i>	<i>27</i>
<i>Figure 2.17 – A Leidenfrost mixer. (a) Concept of design 1A&B Ratcheted substrate placed in an opposite direction 2 A ring used to constrain the droplet 3 Rotating water droplet 4 Ratchets direction. (b) Internal fluid flow via particle image velocimetry (PIV) measurement. Figure taken from Sugioka et al. [115].....</i>	<i>27</i>
<i>Figure 3.1 – Schematic of the ratcheted rings; (a) top view, (b) side view and (c) 3D view; λ_0 and ε are the ratchet period and height respectively at the outer edge.....</i>	<i>31</i>
<i>Figure 3.2 – Top view of the aluminium sheet with shallow basin; used to isolate thermally-driven diffusive mixing from convective mixing on the Leidenfrost rings.....</i>	<i>32</i>
<i>Figure 3.3 – Image analysis sequence using ImageJ (Fiji) (a-d) and MATLAB (e-i).....</i>	<i>34</i>
<i>Figure 3.4 – Schematic procedure to filter noise according to the custom filter.....</i>	<i>36</i>
<i>Figure 3.5 – Schematic procedure to fill-in the droplet pixels.....</i>	<i>37</i>
<i>Figure 3.6 – Automatic droplet detection via MATLAB; (a) and (b) show the droplet position at times t_1 and t_2. The corresponding centre of mass was detected at points P_1 and P_2 respectively; (c) sketch of droplet trajectory (based on centre of mass); θ is the angle (rad) that the droplet rotated during this time.....</i>	<i>38</i>

Figure 3.7 – Manual droplet detection by ImageJ (Fiji); (a) and (b) show a droplet at two different times; (c) sketch of the droplet’s trajectory according to the manual detection, θ' is denoted as the displaced angle.	40
Figure 3.8 – Programme Validation for Automatic Motion Analysis. Example for a water droplet of 150 μL on ring design 4 at 400 $^{\circ}\text{C}$; (a) droplet velocity trend with an average error of -1.29% according to equation 3.22; (b) top-down contact area of the droplet with an average error of 3.82% according to equation 3.23.....	42
Figure 3.9 – An example of mixing process showing colour difference caused by the mixing.	43
Figure 3.10 – Droplet colour/mixing detection using the RGB model (a) Leidenfrost ring, (b) planar aluminium sheet, (c) hydrophobic paper	44
Figure 3.11 – Validation of automated colour detection (droplet volume of 600 μL , ring 2, surface temperature of 350 $^{\circ}\text{C}$). In this example the automated programme differed from the manually calculated standard deviation by just 0.75%.....	46
Figure 3.12 – Curve fitting for droplet mixing data (large droplet volume of 400 μL , dye droplet volume of 60 μL , ring 1, surface temperature of 400 $^{\circ}\text{C}$). (a) is a result of the data analysis in grayscale matrix, and (b) records only the blue channel.	47
Figure 4.1 – Sketch of a single ratchet period. The droplet sits a distance of h_0 above the ratchet. The droplet has two deformed angles of β and θ . The ratchet has a period of λ and depth of ε . The ratchet period changes from the inner edge (λ_i) to the outer edge (λ_o) whilst the ratchet height (ε) is fixed.....	50
Figure 4.2 – Sketch of a single ratchet period; the droplet sits a distance of h_0 above the ratchet. The ratchet has a period of λ and depth of ε . S is the solid ratchet, L is the levitating droplet and G is gas.	53
Figure 4.3 – Sketch of the geometry distribution based on deformation analysis.....	56
Figure 4.4 – Measured driving force from literature [79]	59
Figure 5.1 – Design of the side-viewing window, allowing for the observation of droplet deformation.....	63
Figure 5.2 – Droplet height plotted as a function of volume. The solid (red) line is fitted by Origin [®] ; (a) regularly-shaped droplets on ring designs 2, 3 and 4, (b) irregularly-shape droplets on ring design 1	65
Figure 5.3 – A small $\sim 300 \mu\text{L}$ droplet is observed to be initially circular. Example on ring 4..	66

Figure 5.4 – A larger ~600 μL droplet is slightly elongated since it fills the entire channel. Example on ring 4..... 66

Figure 5.5 – A ~600 μL droplet on ring design 1 with an initial irregular shape due to an enhanced shear force, which is then gradually overcome by surface tension restoring it to a more regular size/shape 66

Figure 5.6 – Droplet width measurement. Example for a water droplet with a 1300 μL volume on ring design 4 at a surface temperature of 400 $^{\circ}\text{C}$ 67

Figure 5.7 – Terminal droplet width prediction using the model in equation 5.9 68

Figure 5.8 – Microscope images showing liquid deformation on ratcheted substrates at various times: (a) $\lambda_0 > \varepsilon$, and (b) $\lambda_e, \sigma \sim \varepsilon$ 69

Figure 5.9 – Volume-contact area calibrations. The calibration was repeated on a heated ratcheted surface for different directions of motion, at different surface temperatures and for different diameter rings, showing that the calibration can be used at all conditions required for the self-propulsion study 70

Figure 5.10 – Droplet velocity and top-down contact area measurement. Example corresponds to a water droplet 60 μL volume on ring design 4, at a surface temperature of 400 $^{\circ}\text{C}$ 71

Figure 5.11 – Terminal velocity measurement; (a) data from all four ring designs at a surface temperature of 400 $^{\circ}\text{C}$, (b) data from ring design 4 at different surface temperatures..... 72

Figure 5.12 – Droplet acceleration on ring design 1. Experiments were run at surface temperature of 400 $^{\circ}\text{C}$. Horizontal error bars come from the volume calibration. Each line represents a different plot of the model 74

Figure 5.13 – Droplet acceleration on ring design 2; (a) acceleration results at surface temperature of 400 $^{\circ}\text{C}$. Each line represents a different plot of the model; (b) vapour flow analysis on a trapezoidal ratchet..... 75

Figure 5.14 – Droplet’s trajectory 76

Figure 5.15 – Acceleration on ring design 4 at surface temperatures of 450 $^{\circ}\text{C}$, 400 $^{\circ}\text{C}$, 350 $^{\circ}\text{C}$ and 300 $^{\circ}\text{C}$. Each line represents a different plot of the model 77

Figure 5.16 – Effect of droplet volume on initial acceleration on ring design 3, at surface temperature of 400 $^{\circ}\text{C}$. Each line represents a different plot of the model..... 77

Figure 5.17 – Acceleration as a function of the ratchet period 79

Figure 5.18 – Acceleration as a function of the ratchet height 79

<i>Figure 5.19 – Experimental measurement of the rate of mass declining. Measurement for a large slug (5000 μL) on ring design 1, at a surface temperature of 400 $^{\circ}$C.....</i>	<i>80</i>
<i>Figure 5.20 – Curve fitting for the droplet velocity against time</i>	<i>82</i>
<i>Figure 5.21 – Energy conversion efficiency from the driving force to the droplet kinetic energy from self-propulsion.....</i>	<i>83</i>
<i>Figure 5.22 – Energy conversion analysis indicates that nearly zero energy is converted to droplet rotation</i>	<i>83</i>
<i>Figure 6.1 – Internal convective cells for Leidenfrost droplets with different radius. Figure taken from Yim et al. [133].....</i>	<i>86</i>
<i>Figure 6.2 – Sketch of the internal convective cells in a self-propelling droplet. The droplet self-propelled along the outer edge of the ring due to a centripetal force, having an elongated shape. Figure reproduced from [133].....</i>	<i>87</i>
<i>Figure 6.3 – Pure diffusion at room temperature. Example for the dye spread in an 800 μL water droplet. The standard deviation of the pixel numbers within the droplet region decreased by 95% at 219 s</i>	<i>89</i>
<i>Figure 6.4 – Diffusion time in stationary droplets at room temperature.....</i>	<i>90</i>
<i>Figure 6.5 – Convective mixing in Leidenfrost self-propelling droplets. Example for the dye collided with an 800 μL DI water droplet on ring design 4 (400 $^{\circ}$C). The standard deviation within the droplet region decreased by 95% at 1.80 s</i>	<i>91</i>
<i>Figure 6.6 – Effect of droplet volume on the mixing time and droplet velocity; surface temperature of 400 $^{\circ}$C</i>	<i>91</i>
<i>Figure 6.7 – Effect of droplet velocity on the mixing time; surface temperature of 400 $^{\circ}$C. Measurements were taken from similar droplet volumes (986-1070 μL).....</i>	<i>92</i>
<i>Figure 6.8 – Mixing time as a function of the droplet length.....</i>	<i>93</i>
<i>Figure 6.9 – Droplet shape study of the merged droplets; (a) Top-down contact area measurement, (b) Droplet width measurement. Data for pure water droplets is taken from figures 5.5 and 5.7 respectively</i>	<i>94</i>
<i>Figure 6.10 – Impact of surface temperatures on (a) mixing time and (b) droplet velocity</i>	<i>95</i>
<i>Figure 6.11 – Star-shaped oscillation for Leidenfrost drops on a flat surface. Example for a water droplet of 800 μL at surface temperature of 400 $^{\circ}$C</i>	<i>96</i>
<i>Figure 6.12 – Volume-contact area calibrations for droplets on a flat surface</i>	<i>96</i>
<i>Figure 6.13 – Droplet mixing times observed on a heated flat surface (400 $^{\circ}$C).....</i>	<i>97</i>

Figure 6.14 – Violent droplet oscillation after initial collisions; (a) and (b) are the standard deviation of the pixel values within the droplet region (region of interest, ROI), showing a small water droplet (400 μ L) and a large one (1200 μ L) respectively. Extracted images are attached. Surface was heated at 400 $^{\circ}$ C..... 98

Figure 6.15 – Liquid volume trapped by the ratchet cavity 99

Figure 6.16 – Energy loss under the assumption of no droplet rotation 100

List of Tables

Table 3.1 – Summary of ring geometries used in this study.....32

Table 5.1 – Measured numerical coefficient for droplet’s friction analysis 73

Nomenclature

Symbols

A	Contact area of a droplet as viewed from above (m^2)
A'	Contact area of a droplet as viewed from the side (m^2)
A_i	Apparent contact area in each single ratchet as viewed from above (m^2)
$A_{i,1}$	Effective contact area of the deformed liquid lying on the slope of the ratchet (m^2)
A_n	Top-down contact area in the n_{th} image, measured by MATLAB (m^2)
A'_n	Top-down contact area in the n_{th} image, measured by ImageJ_(Fiji) (m^2)
a	Droplet acceleration (m/s^2)
\tilde{a}	Numerical coefficient (m^2/kg)
C_1	Proportion of the deformed liquid approaching the descending slope
C_2	Proportion of the deformed liquid approaching the steep sidewall
$C(T)$	Temperature-dependent properties of the vapour flow
c_1	Constants of integration
c_2	Constants of integration
\tilde{c}_1	Numerical coefficient for droplet width
\tilde{c}_2	Numerical coefficient for droplet height
D	Droplet diameter (m)
D_{diff}	Diffusion coefficient in the Leidenfrost regime (m^2/s)
$D_{diff,0}$	Diffusion coefficient at room temperature (m^2/s)
D_o	Outer diameter of the ring (m)
$D_{StdD,i}$	Pixel value of the i_{th} pixel in the droplet region
$\overline{D_{StdD}}$	Mean pixel values in the droplet region
d_1	Numerical coefficient for the friction caused by kinetic energy loss
d_2	Numerical coefficient for the friction caused by potential energy barriers
E	Total energy of a Leidenfrost droplet (J)
E_v	Kinetic energy from droplet's self-propulsion (J)
F	Net force acting on the droplet (N)
F_f	Driving force for the propulsion (N)
$F_{f,i}$	Driving force in a single ratchet (N)

$F_{i,1}$	Supporting force acting on the deformed droplet, exerted from proportion C_1 (N)
$F_{i,2}$	Supporting force acting on the deformed droplet, exerted from proportion C_2 (N)
G	Gas phase
g	Gravitational acceleration (m/s ²)
g_x	Gravitational acceleration in x direction (m/s ²)
g_y	Gravitational acceleration in y direction (m/s ²)
H_L	Droplet height (m)
h_0	Vapour layer thickness (m)
h_w	Height of the integrated viewing window on the ring holder (m)
I_1	Droplet image in a binary code
I_2	Droplet image in an RGB model
$I_{2,\text{red}}$	Red matrix from an RGB image
$I_{2,\text{green}}$	Green matrix from an RGB image
$I_{2,\text{blue}}$	Blue matrix from an RGB image
I_{gray}	Droplet image in a grayscale model
I_o	Original image in an RGB model
i	A certain row in an image matrix
i_0	Central row in an image matrix
i_{max}	The maximum rows of an image matrix
i_{th}	i -th pixel in an image matrix
j	A certain column in an image matrix
j_0	Central column in an image matrix
j_{max}	The maximum columns of a certain image
k_n	Slope of the droplet position to the ring centre in the n_{th} image, analysed by MATLAB
k_{n-1}	Slope of the droplet position to the ring centre in the $(n - 1)_{\text{th}}$ image, analysed by MATLAB
k'_n	Slope of the droplet position to the ring centre in the n_{th} image, analysed by ImageJ_Fiji
k'_{n-1}	Slope of the droplet position to the ring centre, in the $(n - 1)_{\text{th}}$ image, analysed by ImageJ_Fiji

L	Liquid phase
L_L	Latent heat of evaporation of the droplet (J/kg)
l	Droplet length (m)
l_1	Length beneath the droplet interference from proportion C_1 (m)
l_2	Length beneath the droplet interference from proportion C_2 (m)
l_w	Length of the integrated viewing window on the ring holder (m)
M	Droplet mass (kg)
m	Number of the convective cells in a Leidenfrost droplet
m_i	Mass of each smaller droplet masses (kg)
m_j	Droplet mass within a single ratchet (kg)
N_n	Pixel numbers in a droplet image
$N_{StdD,n}$	Pixel values in a droplet image
n_{th}	Order of a certain image matrix
ΔP	Pressure difference that directs the vapour flow (Pa)
P_v	Power for droplet self-propulsion (J/s)
ΔQ_{in}	Heat transfer during a time interval Δt (J/s)
R_n	Effective radius of circular motion in the n_{th} image, analysed by MATLAB (m)
R'_n	Effective radius of circular motion in the n_{th} image, analysed by ImageJ_Fiji (m)
r	Radius of a convective cell in a Leidenfrost droplet (m)
r_i	Distance from the divided smaller droplet mass to the ring centre (m)
S	Solid phase
S_1	Pixels scanned by the scanning matrix, in the first filter progress
s	Displacement of the droplet during the acceleration process (m)
Δs	Striation thickness (m)
s_D	Diffusion distance across the droplet width (m)
T_L	Temperature inside a Leidenfrost droplet ($^{\circ}C$)
$T_{L,0}$	Temperature inside a droplet at room temperature ($^{\circ}C$)
Th	Threshold value for the maximum/minimum pixels, in the filter progress
Th_1	Threshold value for the number of the dark points, defined in the custom programme in the first filter progress
ΔT	Temperature difference between the droplet and the solid surface ($^{\circ}C$)
Δt	Time interval (s)
t_1	Timing for the first image

t_2	Timing for the second image
t_{diff}	Diffusion time at room temperature (s)
t_D	Mixing time between the convective cells (s)
t_m	Mixing time (s)
$t_{m,i}$	Mixing time in each convective cell in a Leidenfrost droplet (s)
u_x	Vapour flow velocity in x direction (m/s)
$\overline{u_x}$	Average velocity of the vapour flow in x direction (m/s)
V	Liquid volume (m ³)
V_b	Liquid volume that deforms into the ratchet cavity (m ³)
v	Droplet velocity (m/s)
v_i	Tangential speed of each smaller droplet mass (m/s)
v_n	Instant droplet velocity for the n_{th} image, analysed by MATLAB (m/s)
v'_n	Instant droplet velocity for the n_{th} image, analysed by ImageJ_Fiji (m/s)
v''_n	Instant droplet velocity for the n_{th} image, analysed by MATLAB according to the centre of mass (m/s)
v_p	Impact velocity (m/s)
W	Channel width of the ring (m)
W_b	Frictional energy loss (J)
W_f	Total energy from the driving force (J)
$w_{i,1}$	Droplet width (m)
w_w	Width of the integrated viewing window (m)
X_n	Centre of mass in the n_{th} image, detected by MATLAB, from the y -axis
X'_n	Droplet position in the n_{th} image, detected by ImageJ_Fiji, from the y -axis,
x_0	Central point in a certain image, from the y -axis
x_i	i_{th} point in a certain image, from the y -axis
Δx	Distance of the vapour flow (m)
Y_n	Centre of mass in the n_{th} image, detected by MATLAB, from the x -axis
Y'_n	Droplet position in the n_{th} image, detected by ImageJ_Fiji, from the x -axis
y_0	Central point in a certain image, from the x -axis
y_i	i_{th} point in a certain image, from the x -axis

Greek Letters

α	Inclined angle of the teeth relative to the horizontal (rad)
β	Deformed angle of the arc AC relative to the horizontal (rad)
γ	Surface tension (N/m)
ε	Ratchet height (m)
$\bar{\eta}_A$	Average relative errors between MATLAB and ImageJ_Fiji (top-down contact area measurement)
$\eta_{e,v}$	Energy conversion from the latent heat of the phase transition into the self-propulsion
$\bar{\eta}_m$	Average relative errors between MATLAB and ImageJ_Fiji (mixing time measurement)
η_v	Energy conversion efficiency from the driving force to the kinetic energy from self-propulsion
$\bar{\eta}_v$	Average relative errors between MATLAB and ImageJ_Fiji (droplet velocity measurement)
$\bar{\eta}'_v$	Average relative errors between the method with corrected radius and the method by centre of mass tracking (droplet velocity measurement)
θ	Deformed angle of the arc BC relative to the horizontal (rad)
θ_n	Angular displacement of the droplet between two successive images, measured by MATLAB (rad)
θ'_n	Angular displacement of the droplet between two successive images, measured by ImageJ_Fiji (rad)
κ	Thermal conductivity of the vapour (W/(m·K))
λ	Ratchet period (length) (m)
λ_e	Effective ratchet period (length) (m)
$\lambda_{e,i}$	Effective ratchet period at the inner edge of the ring (length) (m)
$\lambda_{e,o}$	Effective ratchet period at the outer edge of the ring (length) (m)
λ_i	Ratchet period at the inner edge of the ring (length) (m)
λ_o	Ratchet period at the outer edge of the ring (length) (m)
μ	Viscosity of the vapour flow at mean temperature of the boiling point of the droplet and the surface temperature (Pa.s)
μ_L	Liquid viscosity at Leidenfrost regime (Pa s)
$\mu_{L,0}$	Liquid viscosity at room temperature (Pa s)
ρ_b	Density of the coloured dye (kg/m ³)

ρ_L	Density of the liquid at its boiling point (kg/m^3)
ρ_v	Density of the vapour flow at mean temperature of the boiling point of the droplet and the surface temperature (kg/m^3)
σ	Standard deviation of the pixel values within the droplet
σ_{\max}	Maximum standard deviation of the coloured pixels within the droplet
σ_{\min}	Minimum standard deviation the coloured pixels within the droplet
σ_n	Standard deviation of the pixel values within the droplet, calculated by MATLAB in the n_{th} image
σ'_n	Standard deviation of the pixel values within the droplet, calculated by ImageJ_Fiji in the n_{th} image
$\sigma(t_m)$	Standard deviation when the mixing just finished
φ	Amplitude of the deformed droplet (m)
χ_1	Number of layer interfaces in a convective cell in a Leidenfrost droplet
χ_2	Number of layer interfaces between the convective cells

Chapter 1. Introduction

The Leidenfrost effect is named after a German scientist J. G. Leidenfrost who carefully described the observation of a water droplet on a superheated spoon in the book “A Tract About Some Qualities of Common Water” (1756):

‘This drop which first fell upon the glowing iron is divided into a few little globes, which nevertheless after a little while are collected in one great globe again....this water globule will lie quiet and without any visible motion, without any bubbling, very clear like a crystalline globe, always spherical, adhering nowhere to the spoon, but touching it in one point.’ [1]

Later studies identified a thin vapour film beneath the droplet, allowing the droplet to slowly evaporate in a long-lived, non-wetting and ultramobile state [2-4]. Levitation was also observed for superheated metal particles on a water bath [5] or between two liquids that have a notable difference of the boiling point [6-9], known as the inverse Leidenfrost effect. A newly interesting discovery is the intense trampolining of hydrogels on a superheated surface. These soft solids, consisting of ~99% water, deform upon impact with the heated surface leading to elastic energy. The vapour trapped beneath owing to the Leidenfrost effect would further deform the body to promote droplet bouncing for a considerable amount of time [10].

There have been a subsequent wealth of studies to understand the minimum temperature (Leidenfrost point [11-13]), vapour thickness [14, 15], droplet stability [15], and so forth. Many of these discussions were framed around increasing the Leidenfrost point to avoid the inhibition of the heat transfer rate in this regime [16-19]. However, new dynamical discoveries in association with the Leidenfrost effect have generated increased excitement over potential new applications. This has led to an increased number of new studies and subsequent identification of new phenomena such as droplet bouncing and tramlining [20, 21], droplet self-propulsion [22-24] and droplet self-excitation [25-28].

1.1 Self-Propelled Leidenfrost Droplets

In 2006, Linke *et al.* observed a remarkable pumping effect for Leidenfrost droplets on a saw-tooth ratcheted surface [24]: droplets were spontaneously entrained at a notable speed of

several cm/s over considerable distance, showing promise as a waste heat recovery device for energy generation. Self-propelled Leidenfrost droplets were also observed on a flat surface. However, only droplets on the order of the capillary length (radius ≤ 1.5 mm) were able to self-propel for these flat surfaces [22]. This is because the capillary Leidenfrost droplet was self-tilted in response to an asymmetric internal flow, whilst the symmetric flow patterns in larger Leidenfrost droplets produced no net force. These convective cells had a surface velocity of ~ 5 cm/s via the measurement of particle image velocimetry (PIV), showing the potential for a new means of enhancing droplet mixing.

The most prominent theory to explain the underlying mechanism for droplet self-propulsion is the viscous stress mechanism [29], where the vapour beneath the droplet flows due to a pressure gradient, which then drags the droplet along with it. A joint effect of droplet bouncing was observed on a sub-family of ratchet designs (micro scale) [30], which provides further potential applications for microfluidic systems.

Wells and Agrawal *et al.* constructed a rotation system of Leidenfrost solids and liquids on a turbine-like substrate, from which the proof-of-concept for energy conversion from thermal to kinetic energy then onto electrical energy was demonstrated (see figure 1.1 below) [31, 32]. This self-propulsion effect also has potential in microfluidic systems for transport and targeted delivery of chemicals in the lab-on-a-chip field [33]. For example, Linke *et al.* [24] proposed that this phenomenon could be used to cool computer microchips without the need for extra pumps to drive the coolant [34]. In conjunction with other dynamical behaviours, a Leidenfrost droplet may possess extra 'turbulent-like' features towards enhancing the internal fluid flows for mixing. The ratchets needed for droplet self-propulsion themselves may contribute to later growth of turbulence when the droplet collides with the ratchets [35]. These Leidenfrost-effect-inspired reactors could enable higher reaction yields owing to fast mixing inside the droplets.

One roadblock stopping the practical exploitation of this self-propulsion is the high-temperature requirement for the phenomenon to actually work. Most available waste heat sources are classified as 'low-grade' (below 200–277 °C [36, 37]), which is often insufficient to produce the interesting dynamical effects. In pursuit of a lower temperature regime for droplet self-propulsion, Dupeux *et al.* used superhydrophobic coatings to extend the

Leidenfrost temperature below the boiling point ($\sim 77\text{ }^{\circ}\text{C}$), together with a reduction of temperature inside the droplet [38]. Previous reports show micro structured fabrications can also create large contact angles, favouring a reduction in the Leidenfrost point [39-41]. The ‘cold’ temperature regime raises hopes for new fields and applications of the Leidenfrost regime in the near future.

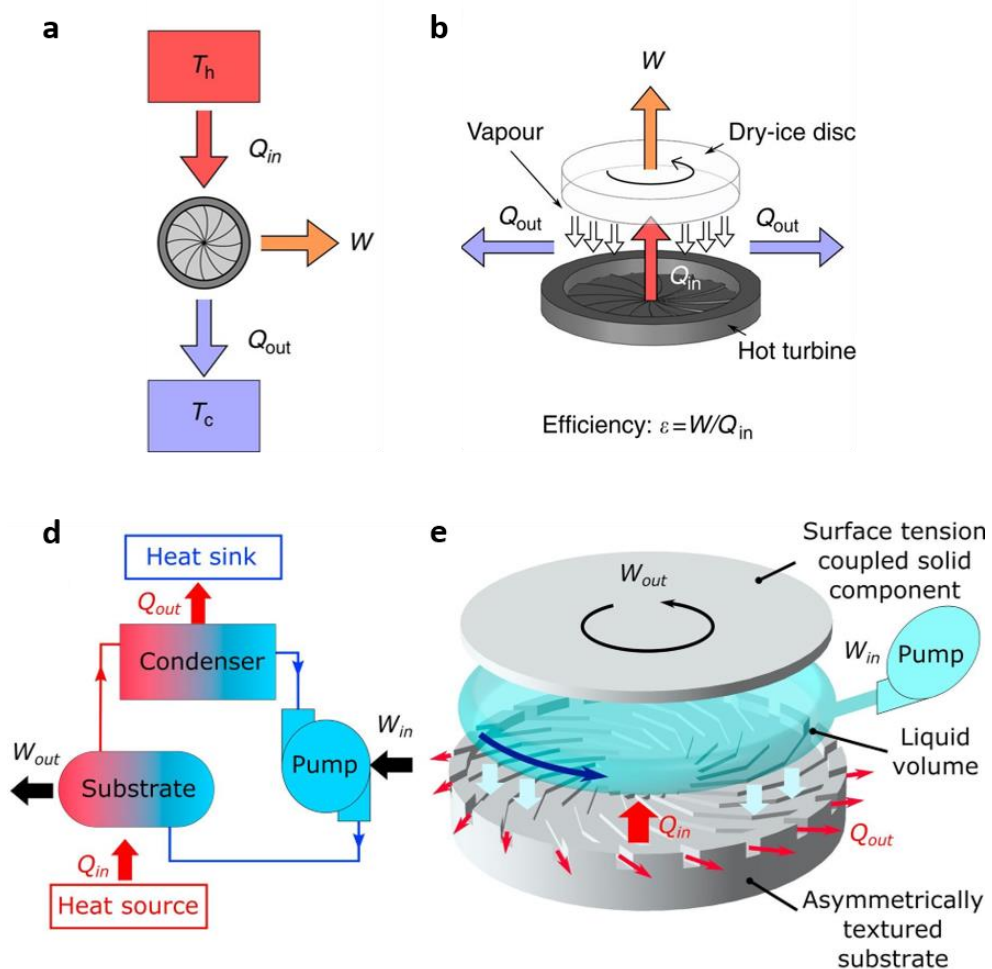


Figure 1.1 – A Leidenfrost heat engine. (a) and (b) are the initial design of the heat engine. (c) and (d) improved the design to a continuously operation system. Panels (a) and (b) are taken from [31]. Panels (c) and (d) are taken from [32]

1.2 Areas for Further Research and Problem Statement

Existing models in the literature only describe the dynamics for “self-propelled Leidenfrost droplets” using a simple scaling analysis based upon rigid solid bodies (usually a dry ice disc) [42]. There is still no quantitative description of the more complex geometries associated with the deformable liquid-vapour interface beneath a liquid droplet. This severely restricts the ability to design Leidenfrost-based systems for the aforementioned applications. It will

therefore be worthwhile to establish a new quantitative first-principles model by taking the liquid deformation into consideration. This will also improve the general understanding of the driving force.

Since a Leidenfrost droplet generates internal convective cells [22] that will combine with other effects such as star-shaped oscillations (on a flat surface) [25] and self-propulsion (on a ratcheted surface) [24], these dynamical behaviours may further generate turbulent-like patterns inside the droplet so as to improve the mixing process. This area has received little attention and also warrants further investigation to test the potential for using these devices for mixing applications.

In terms of empirical studies of this self-propulsion, the conventional design is to fabricate the ratchets in a linear array [24]. Cousins *et al.* constructed concentric circular ridges to trap the Leidenfrost droplets [43]. An alternatively advanced design is to fabricate the ratchets on a ring-shaped substrate, both to save the footprint and to terminate corresponding study under observation.

1.3 Research Aims and Objectives

Based on the above gaps in knowledge, the overall aim of this thesis is to provide a fundamental understanding of the propulsion dynamics for a self-propelled Leidenfrost liquid droplet and explore droplet mixing under the Leidenfrost state. Four main themes are defined: (1) development of a suitable method for recording and analysing the motion of liquid Leidenfrost droplets, (2) development of a new analytical model to describe the propulsion dynamics of these liquid droplets, (3) perform experimental studies on droplet self-propulsion in compact ring devices, (4) study droplet mixing under the Leidenfrost state. To achieve these goals, the following objectives are defined:

1. Experimental study of droplet self-propulsion on several ratcheted ring designs using a high-speed camera, in the difference of droplet size, ratchet parameters and surface temperature;
2. Experimental study of mixing between a self-propelled water droplet and a dye droplet, to be carried out on the four ratcheted rings in the Leidenfrost regime;
3. Automatic detection of droplet motion and mixing through the development of a

custom programme, based on digital image manipulation in ImageJ and coding in MATLAB;

4. A new mechanistic model to quantify the driving force of liquid droplets whilst taking droplet deformation into account in a non-empirical way;
5. To summarize the research and provide an opinion on the directions of the research field.

1.4 Novelty

A custom programme is presented in *Chapter 3* to process the high speed camera videos, which makes data analysis more precise and efficient.

An analytical model is presented in the thesis to describe the dynamics of self-propelled droplets (in *Chapter 4*). The model is constructed with the consideration of droplet deformation for the first time, whereby a theoretical analysis of droplet deformation is performed under a pressure balance between the hydrostatic pressure, dynamic pressure and Laplace pressure. Using the friction model proposed in the literature, a terminal velocity model is proposed in a further step, aiming to direct the optimization of the ratchet design. This has not previously been attempted in the literature.

Four ratcheted surfaces in a ring shape are fabricated, which enables experimental studies in a much smaller footprint compared to the wider literature, which all use linear surfaces that impose restrictions on the measurement of the terminal velocity. Experimental results of the self-propelled droplets (in *Chapter 5*) are shown to be in good agreement with the model (in *Chapter 4*). Meanwhile, these devices demonstrate an excellent method for fast droplet mixing (*Chapter 6*), opening up a potential new research direction.

Chapter 2. Literature Review

The common observation of seemingly random gliding water droplets on a hot kitchen pan is an example of Leidenfrost induced motion. In the Leidenfrost state, a vapour layer insulates and levitates the droplet from the surface, making the droplet highly mobile with little friction [44]. A droplet in the Leidenfrost state can also bounce (*e.g.* figure 2.1a) [21], analogously to the bouncing observed on hydrophobic surfaces [45-47]. It briefly contacts the surface [48] that induces a directed rebound by the presence of the texture gradients [49-53]. Directed droplet motion can also be induced by an asymmetry of surface temperature (*e.g.* figure 2.1b) [23, 54] or surface topology (*e.g.* figure 2.1c) [24]. Additionally, in the presence of phase contact, a ratcheted surface can also induce liquid transport due to local differences in wetting angles. Figure 1d(i) demonstrates liquid transport on a ratcheted surface via a pulsed electric field [33, 55-57]. These ratcheted surfaces also exist in nature. For example, Shorebirds have beaks containing ratcheted capillaries that are able to transport water in combination with mechanical tweezering motion (*e.g.* figure 1d(ii)) [58]. Araucaria leaves also contain ratchet-like structures to direct liquid motion (*e.g.* figure 1d(iii)) [59]. In these examples, it is the combination of an external energy source with the surface and liquid properties that introduces the anisotropy necessary for propulsion. However, the transport speed is only a few mm/s [55].

Remarkably, on a ratcheted surface, a Leidenfrost droplet will self-propel in a well-defined direction with a high velocity (order of ~ 0.1 m/s; *e.g.* figure 2.1c) [24]. These velocities are much higher than other passive transport effects such as the Marangoni effect [60-64]. These systems with no other external energy fields (other than the heated surface) are designated as Leidenfrost self-propulsion devices, first introduced by Linke *et al.* [24]. Leidenfrost self-propulsion has since inspired several studies to understand the origins and fundamentals of this phenomenon, leading to further developments in micro/nano fabrication technologies as well as several interesting applications. In view of the recent interest in this area, Stewart traced the dynamical discoveries of the Leidenfrost effect back to the very first story on the phenomenon in 1732 [4]. Earlier, Quéré paid effort to describe the Leidenfrost dynamics in the *Annual Review of Fluid Mechanics* [65]. The purpose of this chapter is to highlight the state-of-the-art in the Leidenfrost self-propulsion area to identify the present gaps in knowledge and corresponding future research directions.

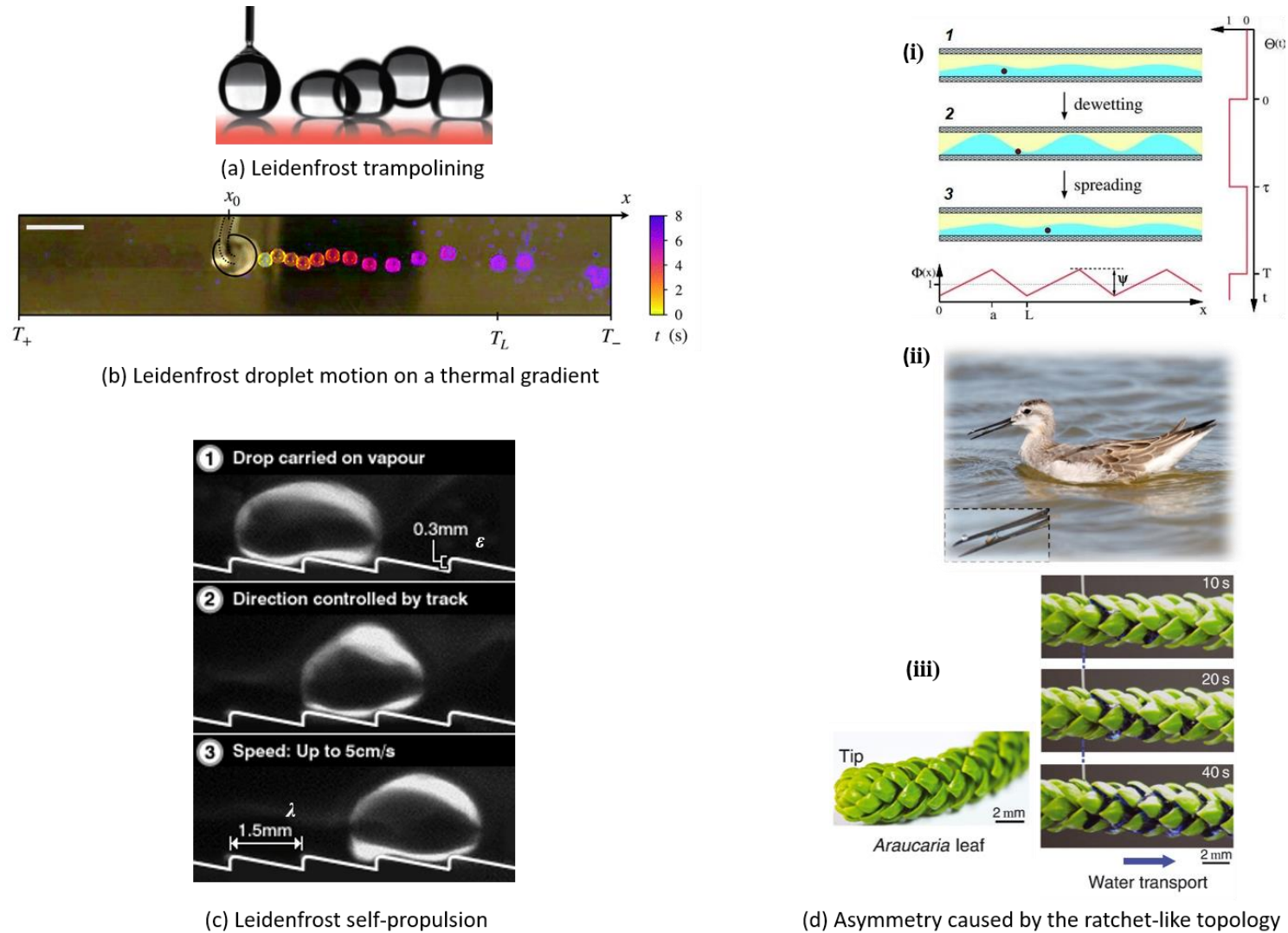


Figure 2.1 – ‘Passive’ methods to induce liquid motion | (a) Droplet trampolining at Leidenfrost state [21], (b) Leidenfrost droplet motion on a thermal gradient [23], (c) Leidenfrost self-propulsion on a heated ratcheted surface [24], (d) Liquid transport on a ratcheted surface [56, 58, 59]

2.1 Wetting Theory

In statics, the degree to which a liquid drop will spread on a solid surface can be described by Young's equation:

$$\gamma_{SV} = \gamma_{SL} + \gamma \cos \theta_{eq} \quad (2.1)$$

where γ_{SV} , γ_{SL} , and $\gamma \equiv \gamma_{LV}$ denote the respective solid-vapour, solid-liquid and liquid-vapour surface tensions, and θ_{eq} is the contact angle that the droplet makes with the solid surface at equilibrium. Under most conditions, the droplet partially wets the surface ($0^\circ < \theta_{eq} < 90^\circ$) as demonstrated in figure 2.2. Complete wetting occurs when $\theta_{eq} = 0^\circ$ where the drop completely covers the solid surface. Conversely, complete drying corresponds to $\theta_{eq} = 180^\circ$, though this is rarely observed. Generally, if the contact angle exceeds 90° , the surface is described as being hydrophobic. In the particular case of a Leidenfrost droplet that levitates on a vapour cushion, only one surface tension is involved; γ_{SV} and γ_{SL} disappear from 2.1: Here, the index S is replaced by V , which yields $\theta_{eq} = 180^\circ$ that represents a non-wetting state.

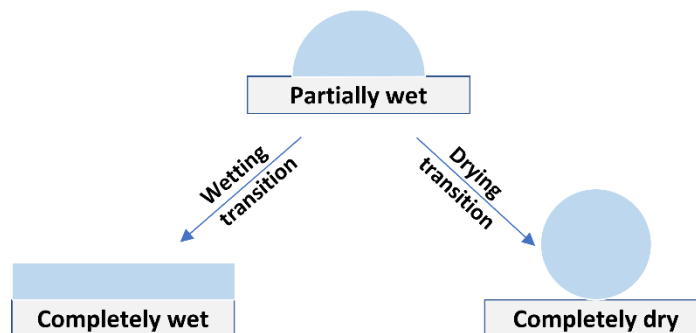


Figure 2.2 – Ideal wetting of a drop on a solid surface. Figure reproduced from [66]

From a practical point of view, most solids are not homogeneous due to the natural roughness or chemical heterogeneity. This leads to a difference of the contact angles between the front and the rear of the droplet, which is referred to as the contact angle hysteresis. This difference in contact angles generates a force that enables droplets on inclined surfaces to resist motion due to gravity. The magnitude of the so-called contact angle hysteresis is on the order of the contact angle itself, which itself qualitatively depends on 'how' and 'where' the drop is deposited on the surface. More detailed theoretical knowledge on the phenomenon of wetting and spreading is referred to the reviews by Bonn *et al.* [66] and Quéré [67].

2.2 Leidenfrost Dynamics

2.2.1 Levitation on Smooth Surfaces

The Leidenfrost effect occurs when a liquid or solid “contacts” a surface significantly hotter than the boiling (liquid) or sublimating (solid) points, resulting in the formation of a vapour layer that insulates and suspends the liquid/solid from the surface. The vapour beneath a Leidenfrost body is expelled isotropically [42], and in this regard, the body randomly hovers over a flat surface. The vapour thickness is thin ($10 \sim 100 \mu\text{m}$ [15]) which confirms the dominant role of conductive heat transfer ($\kappa\Delta T/h_0$, per unit area) over convection ($h\Delta T$, per unit area). Here, ΔT is the temperature difference between the droplet and the surface, κ is the thermal conductivity of the vapour ($\sim 0.038 \text{ W}\cdot\text{m}^{-1}\cdot\text{K}^{-1}$ at $250 \text{ }^\circ\text{C}$), h_0 is the vapour layer thickness, and h is the convection heat transfer coefficient (roughly $25\text{--}250 \text{ W}/(\text{m}^2\cdot\text{K})$ for gases). Radiation becomes comparable when the temperature exceeds $1000 \text{ }^\circ\text{C}$ [65]. Herein, the lifetime of the liquid/solid is drastically increased owing to the lower heat transfer rate [15].

When the droplet’s size is comparable to the capillary length (see equation 2.1), the droplet stays quasi-spherical owing to the cohesion provided by the surface tension. Note, in equation 2.1, γ and ρ_L are the surface tension and liquid density at the boiling point respectively, and g is gravity. When the droplet size increases, gravity begins to dominate the role of surface tension, leading to a constant droplet height, where $H_L = 2l_c$ [15, 65].

$$l_c = \left(\frac{\gamma}{\rho_L g} \right)^{\frac{1}{2}} \quad (2.1)$$

Levitation may enter a stage of Rayleigh–Taylor instability for large droplets, where the vapour in the centre rises and forms a chimney before it finally bursts as evident in figure 2.3a [15]. A slight curvature of the flat surface will prohibit the instability, whereby a Leidenfrost droplet undergoes star-shaped oscillations as shown in figure 2.3b. The vibration of these evaporating droplets has since been described, though the underlying mechanism was initially poorly understood. It has recently been suggested that the oscillating hydrodynamics are a result of local differences in the vapour thickness that create large shear stresses around the droplet’s liquid-vapour interference, which then induces large pressure oscillations beneath the droplet’s centre [25, 68, 69]. Nevertheless, the oscillations present the opportunity for a Leidenfrost-effect-induced stirred tank reactor.

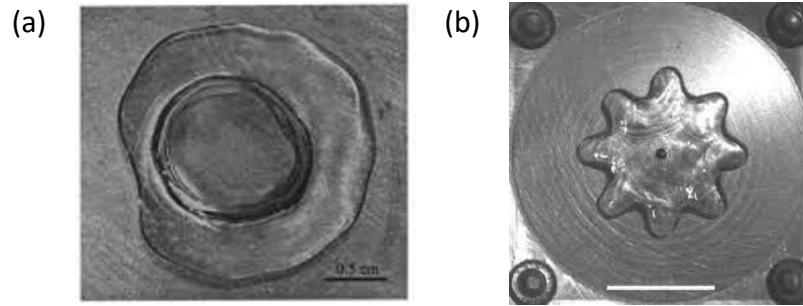


Figure 2.3 – (a) Chimneys of vapour induce the Rayleigh-Taylor instability for large Leidenfrost droplets (Biance et al. [15]), (b) Star-shaped droplet oscillation. Figure taken from Ma et al. [25]



Figure 2.4 – Capillary Leidenfrost droplets self-propel on a smooth surface [70]

A newly discovered dynamical behaviour is the self-propulsion of capillary Leidenfrost droplets on a smooth surface [22]. These so-called “Leidenfrost wheels” (see figure 2.4) were self-titled by an asymmetric internal fluid flow such that the vapour expulsion was anisotropic, inducing a viscous drag towards the drop from above. Large droplets that failed to self-propel instead developed symmetric internal flow patterns. These convective cells had a surface velocity of ~ 5 cm/s measured through particle image velocimetry (PIV), suggesting a promising method for fast droplet mixing. In the video by Chiu and Sun [71], a pure water droplet (radius of 1.1 mm) mixed with a fluorescent droplet (radius of 1.1 mm) mixed in only 0.05 s.

2.2.2 Special Dynamics

The inverse Leidenfrost phenomenon was reported in 1969: hot metal particles were observed to levitate above a liquid base [5]. It was the large heat flux between the metal particles and liquid that formed a bubble wall that suspended the metal particles. Afterwards, the inverse Leidenfrost phenomenon was observed between two liquids. This included droplet self-propulsion due to the different vapour thicknesses between the front and back edges of the levitated drop [6-9]. The lifetime of these suspended droplets depended on the heat energy stored in the Leidenfrost body. Upon eventual cooling, the body finally sinks into the second liquid (the liquid substrates tend to have a very low boiling point) [5, 7]. The maximum particle size that can be suspended is determined by the surface tension.

In 2006, Linke *et al.* [24] found that droplets of different types can self-propel on a saw-tooth ratcheted surface, provided that the solid surface is heated above the Leidenfrost point of the droplet, T_L [15, 72]. Droplets self-propelled along the descending slope of the ratchet, reaching a remarkable terminal velocity in a short amount of time (see figure 2.6). Leidenfrost self-propulsion is marked as a modern breakthrough in the dynamical discoveries on Leidenfrost effect [4, 65]. Theoretically, any vaporisable material has the ability to self-propel on a ratcheted surface as long as the Leidenfrost state is obtained.

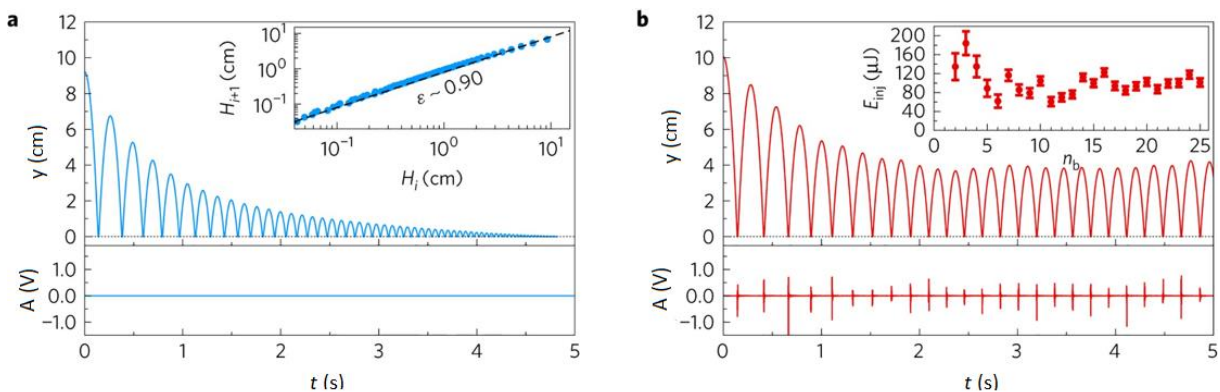


Figure 2.5 – Hydrogel trampolining. (a) The hydrogel gradually stopped bouncing on the cold surface, where the audio signal (bottom) did not reflect any evaporation. (b) On a heated surface, the restitution coefficient is maintained as 1 or even above because of the energy injection during evaporation, which kept the hydrogel bouncing in a steam engine way for a considerable time. Figure taken from Scott *et al.* [10]

A somewhat related phenomenon has also been observed that converts thermal to kinetic energy, which may provide an alternative strategy for building a waste heat engine. Hydrogels are three-dimensional hydrophilic polymer networks that can absorb relatively large volumes of water making them remarkably elastic. Usually, when elastic materials impact solid surfaces, the kinetic energy is converted into elastic potential energy and a small amount of heat as the material deforms. It is the dissipation of this heat that results in energy loss, causing the kinetic energy to decline over time (see figure 2.5a). However, hydrogel spheres impacted on hot surfaces have shown the ability to continually rebound for several minutes (see figure 2.5b) [10, 73, 74]. In this case, the energy loss is compensated by an overpressure upon deformation caused by the evaporation of the absorbed liquid and resulting ejection of the vapour. Thus, the droplets will continually bounce provided there is sufficient liquid remaining and a heat source. Restitution coefficients greater than unity have even been observed, meaning hydrogel spheres placed on heated surface will seemingly spontaneously start bouncing. Another system of such mechanical energy injection can be realised via two hydrogels colliding in a microwave, as the contact region will create intense electromagnetic hotspots that causes the same type of overpressure evaporation [75].

2.3 Leidenfrost Self-Propulsion on Ratchet Surfaces

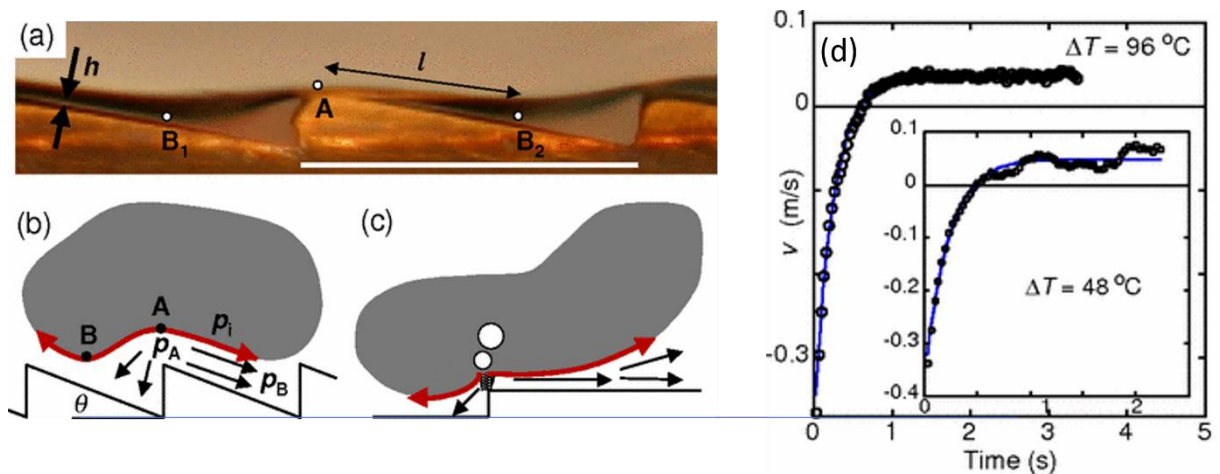


Figure 2.6 – The report by Linke et al. [24] | (a) High-resolution photograph of the liquid-vapour-solid interface, (b) Schematic of the directed vapour flow driven by the pressure gradient $\Delta p = p_A - p_B$, (c) A nucleate boiling event in low temperature regime. Evaporation was enhanced to further improve droplet motion, (d) Typical velocity trend for a self-propelling droplet. Measurement was stable in high temperature regime (main panel) but fluctuated in low temperature regime (inset)

In the initial report, Linke *et al.* [24] also found droplet self-propulsion was influenced by the droplet size, temperature regime and ratchet parameters. In detail, puddles or slugs were observed to break into small droplets unless a confined channel was provided. Propulsion was enhanced in a low temperature regime, owing to the nucleate boiling effect when the droplet made partial contact with the surface (see sub-figures 2.6c and 2.6d). Whereas a full Leidenfrost regime produced stabilized droplet motion due to a fully developed vapour layer. Later studies by Ok *et al.* [76] and Grounds *et al.* [77] further quantified a more significant improvement in the low temperature regime, which was called a transition regime [78].

Linke *et al.* [24] initially proposed different mechanisms to account for the droplet self-propulsion. Considering the deformed liquid gave rise to a pressure difference along the ratchet slope (see sub-figures 2.6a and 2.6b, showing a difference of Laplace pressure), it was suggested that self-propulsion may stem from the viscous drag induced by a pressure-driven flow in the vapour. However, this did not explain the self-propulsion of a solid sublimatable disc (dry ice) which does not deform. Subsequently, a debate emerged within the literature on the underlying mechanism for Leidenfrost self-propulsion. New mechanisms such as a “rocket effect” (jet thrust) [79], thermal creep flow [80], viscous mechanism [42], asymmetric wettability [49], and self-rotation-induced propulsion [81] were proposed. More in-depth studies based on numerical [29] and experimental [42] approaches seem to bring the debate to an end: a rectified vapour flow by the asymmetric ratchet drags the droplet along (see Section 2.5 for further discussion).

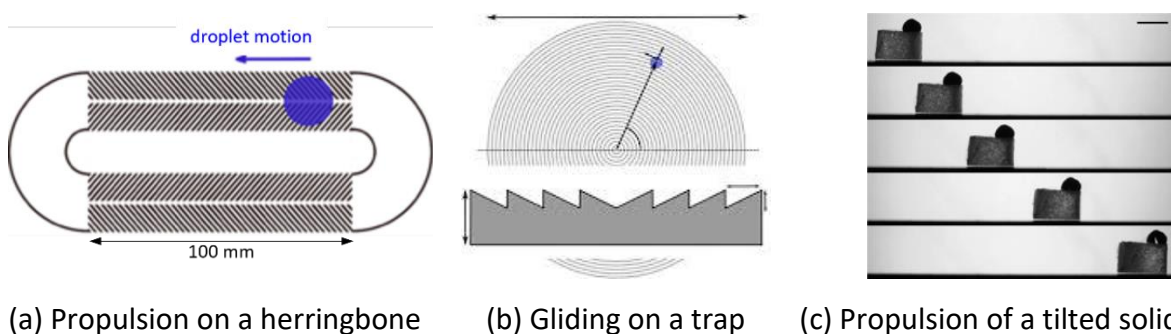


Figure 2.7 – Expanded patterns for Leidenfrost self-propulsion. Panel a taken from Soto *et al.* [82]. Panel b taken from Cousins *et al.* [43]. Panel c taken from Dupeux *et al.* [83]

Nevertheless, Linke *et al.*'s device has inspired a rich variety of designs for droplet control. On the one hand, ratchets were scaled down at micro/nano scale [76], on the other hand patterns

were expanded to other asymmetric shape such as herringbones (figure 2.7a) [82, 84] and concentric ridges (figure 2.7b) [43]. Even a simply tilted solid can self-propel on a flat surface (figure 2.7c) [83]. All these designs can rectify the evacuation of vapour and consequently generate propulsion. In a broader scope, a dynamical Leidenfrost self-propulsion could be created using external forces. For instance, Soto *et al.* [85] designed a substrate with pores through which air was blown to levitate objects. The air flow was directed by the embedded herringbones and that levitated the object which then 'surfed' on the air cushion.

2.3.1 Enhanced/Unconventional Propulsion at Micro and Nano Scales

Micro and nano scaled patterns have been manufactured as a step towards micro- and nano-fluidic applications using techniques such as micromilling [76], pulsed laser source [30, 86] and anisotropic reactive ion etching [49, 50]. Though the Leidenfrost point could be increased by surface roughness effect [16, 19, 87-90], droplet velocities were up to 0.4 m/s in a low temperature regime [76, 91, 92].

Specifically, Ok *et al.* [76] identified a threshold temperature (T_{Th}) to trigger droplet propulsion, which was lower than the corresponding Leidenfrost point on the specific surface. This had also been observed by Linke *et al.* [24], who noted that higher droplet acceleration with higher terminal velocities existed in a lower temperature regime, even though the insulating vapour layer was not fully developed. This low temperature regime corresponds to the transition boiling regime [78], where the liquid partially contacts the surface. The heat transfer rate is greatly enhanced in the transition boiling regime, leading to an increased evaporation rate that enhances propulsion. To evidence the local surface contact, Alex *et al.* [77] used a microphone to monitor the sound produced by the droplets. Little sound was recorded in the Leidenfrost regime, whereas signals showed notable amplitudes in the transition boiling regime, enabling both regimes to be differentiated.

When structures were further reduced to nano scales, a Leidenfrost droplet hovered randomly [49], corresponding to a scenario that the droplet treats the substrates as a flat surface [76]. When the droplet was released from a considerable height, directional droplet motion was observed given that the nanostructured patterns were designed with preferential wettability [49, 50]. The Weber number, as defined in equation 2.2, was selected as the criterion for the two scenarios as it compares the droplet inertia to its surface tension.

$$We = \frac{\rho_L v_p^2 D}{\gamma} \quad (2.2)$$

Here, v_p is the impact velocity and D is the droplet diameter. At increased Weber number, the boiling regime transfers from gentle boiling to transition boiling [49, 78, 93, 94]. Hence, the directional motion is a coexistence of several dynamical effects. Firstly, a Leidenfrost droplet made brief contact with the solid surface at a considerable Weber number [48, 93, 94], inducing preferential spread of the droplet owing to the anisotropic wetting properties [51, 53]. Secondly, a capillary droplet would bounce when impacted onto a superhydrophobic surface (see figure 2.1a) [10, 20, 21, 45, 48, 73, 74]. The droplet could re-bounce in a quasi-elastic regime, where the restitution coefficient approaches unity (defined by the ratio of relative speeds after and before collision) [20, 74].

2.3.2 The Cold Leidenfrost Self-Propulsion Regime

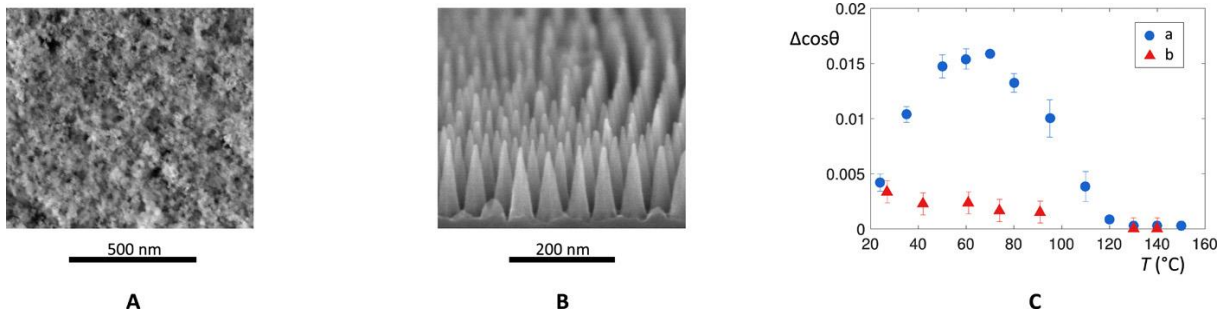


Figure 2.8 – Contact angle hysteresis from two kinds of hydrophobic nanostructure | (A) and (B) are the SEM (scanning electron microscopy) images of the two. (A) A brass surface coated by Glaco solution. (B) A silicon surface decorated with nanocones and coated by fluorosilanes. (C) Contact angle hysteresis $\Delta \cos \theta$ from the two surfaces. Figure taken from Bourriane et al. [95]

Extending the Leidenfrost self-propulsion below the usual Leidenfrost temperatures is important for practical applications. Superhydrophobic coatings have been used to make the surface water-repellent, leading to a notable reduction of the Leidenfrost point [95, 96]. The domain where a droplet exhibits self-propulsion has extraordinarily extended to a regime below the boiling point [38], suggesting a much thinner vapour film to induce self-propulsion. In this ‘cold’ self-propulsion regime, the droplet does not levitate but sits on a fixed vapour thickness that scales with the surface roughness. The pinning effect from the contact angle

hysteresis [97] eventually prohibits droplet motion, indicating a threshold temperature for droplet self-propulsion. In Dupeux *et al.*'s study [38], a colloidal solution set the threshold temperature around 77 °C. The pinning effect is weak on a surface with conical structures (figure 2.8B), suggesting a much lower threshold temperature for droplet self-propulsion. This hydrophobic surface coating technique may therefore unlock the capability to recover lower grade/quality waste heat for energy harvesting applications.

Dubnack *et al.* [98] further considers the stability of the colloidal solutions used by Dupeux *et al.* [38]. They chose to use silanization for superhydrophobic treatment, and nanostructures were textured on the ratchet tops using laser-induced periodic surface structures, which consequently modified surface roughness and wetting properties. Droplet self-propulsion was observed around 120 °C, which is still far below the usual Leidenfrost self-propulsion temperatures.

2.4 Solid Leidenfrost Phases

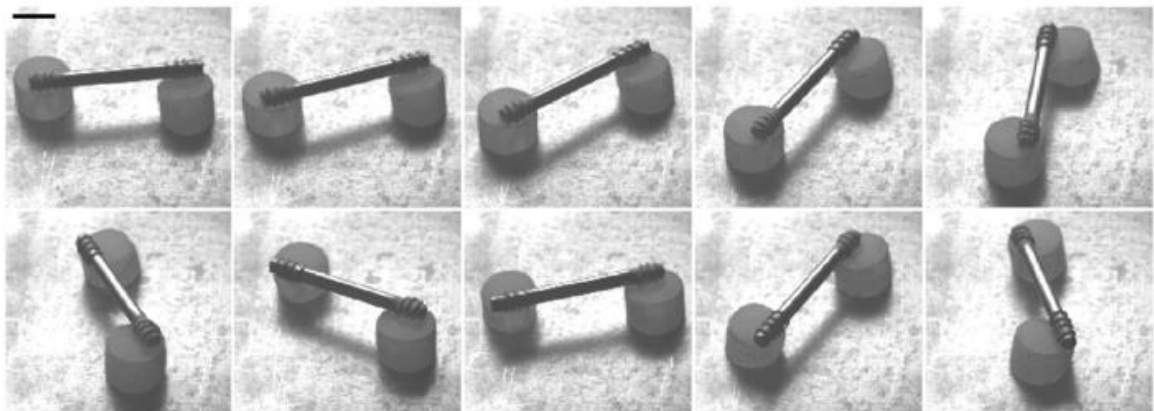


*Figure 2.9 – A self-rotation device made of two Leidenfrost solid bodies. An off-centred rod creates the asymmetry of the system to induce solid motion in opposite directions. Figure taken from Dupeux *et al.* [83]*

Beyond the study with pure droplets, solids that sublime have also been studied. The use of dry ice platelets in the mechanism study simplified the system by eliminating droplet deformation [29, 42, 79, 99]. Dry ice was even used to demonstrate a proof-of-concept of electricity generation by Wells *et al.* [31], who attempted to exploit the kinetic energy from the high-speed Leidenfrost self-propulsion. Since solids can be sculpted into different shapes, a “continuous ratchet” was created by tilting a piece of dry ice (see figure 2.7c) [83]. The

absence of the ratchets made this transportation mode more efficient in two ways. First, this approach is theoretically more scalable because the absence of the ratchets eliminates the potential for the levitated object to strike the steps. Second, the absence of the ratchets also reduces the apparent friction associated with the energy loss of the deformed liquid (friction will be analysed in Section 3.5) [100], meaning the acceleration phase for a Leidenfrost solid is longer, which enhances the terminal velocity (increasing the energy conversion efficiency). Likewise, tilted solid camphor can self-propel on a smooth surface [83], and a droplet in capillary length can tilt itself to self-propel not only on a solid surface [22] but also on a liquid substrate [6-9]. Figure 2.9 shows a self-rotational system on the basis of the special properties in Leidenfrost solid bodies [83].

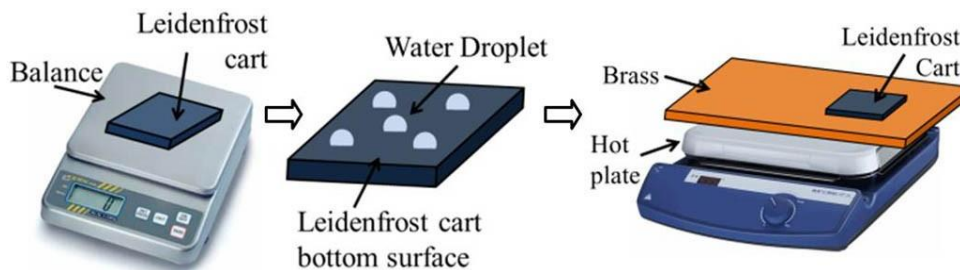


Figure 2.10 – Design of a frictionless Leidenfrost cart. Figure taken from Ali *et al.* [101]

More interestingly, Ali *et al.* [101] designed a frictionless cart driven by Leidenfrost droplets. The design of the so-called Leidenfrost cart is shown in figure 2.10. Several droplets were placed underneath a solid plate, behaving as the ‘wheels’ of the cart when they self-propelled on a ratcheted surface. The cart exhibited very minor friction by the presence of the vapour cushion [65]. However, the vapour thickness became thinner when increasing the loaded mass, as expected, which finally prevented the cart from sliding as the pinning effect raised the friction. In this study, the cart consumed considerable energy because of the high Leidenfrost point.

A diverse system of levitation may alter the heat transfer mechanism, then finding its application in the field of spray quenching applications. For instance, Edalatpour *et al.* [102] recently discovered a three-phase Leidenfrost effect that hugely increased the Leidenfrost point to 550 °. In the three-phase system, a piece of frozen water was surrounded by a small quantity of meltwater and the whole object was levitated on its vapour layer. Convection in

the thin meltwater film is no longer ignorable in addition to the conduction in the thin vapour film, leading to an abrupt increase of the Leidenfrost point and the heat flux.

2.5 Current Theoretical Advancement

The exact mechanism for the Leidenfrost self-propulsion and the friction exerted by the ratchets has been the subject of debate for some time. Some of the proposed theories have been experimentally validated, whilst others have been supported by numerical analysis. This section of the review will outline and compare these proposed mechanisms, including in-depth discussion of the self-propulsion phenomenon itself. Studies based on experimental studies will be carefully described, while theories from numerical analysis will be briefly introduced as it is beyond the scope of the research.

2.5.1 Initial Proposals by Linke

Linke *et al.* [24] proposed different mechanisms to explain the phenomenon they observed. Their viscous mechanism involves the evaporated vapour beneath the droplet being rectified by the deformed droplet shape, which then exerts a viscous drag on the droplet. As shown in figures 2.6a and 2.6b, the negative and positive curvature differences between points A and B_2 indicates a local difference of the Laplace pressure, as defined in equation 2.3.

$$\Delta p = \frac{\gamma}{r} \quad (2.3)$$

Here, Δp is the pressure difference between the droplet's internal pressure and the external pressure in the vapour film and r is the local radius of the curvature of the droplet. This pressure differential between point A and point B_2 subsequently induces a vapour flow down the declining slope of the steps, while part of the vapour escapes laterally into and out of the plane of figure 2.6b (black arrows, also see figure 2.12 for clarification). Therefore, a net 'forward' driving force causes the vapour to flow 'forward' in each ratchet period. Because of the interfacial viscous force (*i.e.* no-slip boundary condition), this vapour flow then 'drags' the droplet in the same direction.

A model of Poiseuille vapour flow between two parallel plates [103] was applied for the viscous analysis. Experimental measurement was needed to deduce the driving force for lack of models on pressure difference (which is a question of force analysis) and vapour thickness (which is a question of heat transfer analysis).

They also pointed out thermocapillary flow may also induce propulsion (along the red arrows in sub-figures 2.6b and 2.6c), which then leaves an open question for later studies on the role of viscous drag and thermal creep [29, 80].

2.5.2 Jet-thrust Momentum Conversion and Corresponding Models

Using a piece of dry ice to reproduce the Leidenfrost self-propulsion, Lagubeau *et al.* [104] pointed out the insignificance of deformability of the moving body. Instead, a “rocket effect” was proposed to explain the forward propulsion of the Leidenfrost body. Specifically, the vapour is rapidly expelled from the Leidenfrost body during evaporation which is then rectified by the presence of the ratchets, resulting in a directed vapour flow in the opposite direction to the motion of the dry ice (*i.e.* Newton’s 3rd law of motion).

An elegant model was subsequently proposed to develop the theory. First, a model of the vapour thickness was proposed based upon the conservation of matter. That is, the flow rate of the evaporated mass (scaled as equation 2.4) equates to the rate of mass evaporation, which was itself considered using Fourier’s heat conduction law across the vapour film beneath the droplet (scaled as equation 2.5):

$$\dot{M} \sim \rho h_0 R U \quad (2.4)$$

$$\dot{M} \sim \frac{\kappa \Delta T R^2}{L h_0} \quad (2.5)$$

In these equations, U is the vapour flow velocity, h_0 is the vapour film thickness, R is the radius of levitated body, κ is the thermal conductivity of the vapour, L is the latent heat of evaporation and ΔT is the temperature difference between the bottom of the Leidenfrost body and the ratchet surface (assuming to be constant).

A lubrication approximation was used for the flow rate analysis in equation 2.6, given that the film thickness was much smaller than the radius of the levitated body, *i.e.* $h_0 \ll R$:

$$U \sim \frac{h_0^2 \Delta P}{\mu R} \quad (2.6)$$

Here, μ is the vapour viscosity and ΔP is the overpressure induced by the weight of the Leidenfrost body (equation 2.7; where ρ_0 and H_0 are the density and height of the Leidenfrost body respectively). The pressure difference then drives the vapour flow.

$$\Delta P \sim \rho_0 H_0 g \quad (2.7)$$

Combining equations 2.4–2.7 then provided a scaled representation of the film thickness, h_0 . Under the assumption of momentum conservation, the driving force for propulsion, $F_f = \dot{M}U$, was given by equation 2.8 (where $C = (\mu\kappa\Delta T/L\rho\rho_0gH_0)^{1/2}$).

$$F_f \sim (C^4 \rho \rho_0^2 g^2 H_0^2 / \mu^2) \left(\frac{R}{C}\right)^{\frac{3}{2}} \quad (2.8)$$

Assuming that the model suits a water droplet, C is constant for large droplets at a specific temperature because the droplet has a stable height of ~ 5 mm [15].

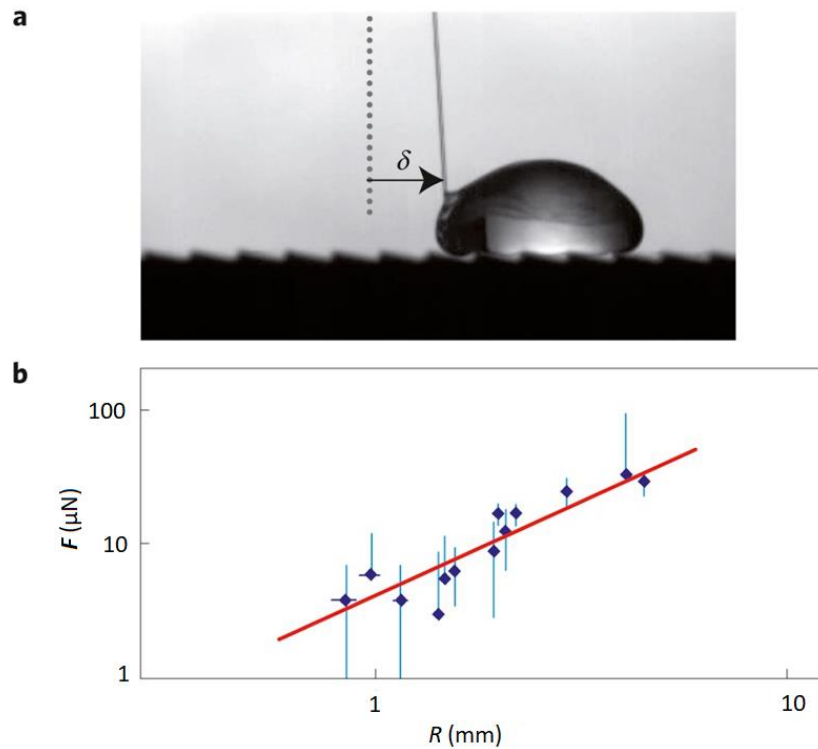


Figure 2.11 – Direct force measurement via a glass fibre, deflecting the fibre by a distance of δ . Figure taken from Lagubeau et al. [104]

This model suggested an exponent of 1.5 for the power law relationship between the driving force, F_f , and the droplet radius R . A method of direct force measurement was proposed as shown in figure 2.11a to confirm this. Here, a glass fibre was used to hold a propelling droplet in place, where the elastic tension of the fibre balanced the driving force. The elastic force in response to the horizontal distance, $K\delta$, was taken as an equivalent value for the driving force acting on the droplet via the interaction of the vapour and the ratchets. The vertical elastic

force was ignored in the analysis. A line of best fit through the experimental data gave a slope of 1.47, seemingly validating the jet thrust mechanism (solid line in figure 2.11b).

2.5.3 Viscous Stress Induced by Rectified Vapour Flow

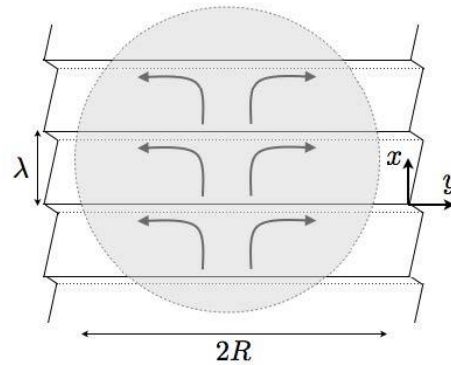


Figure 2.12 – Vapour flow (arrow direction) rectified by saw-tooth ratchets, via tracer measurement. Figure taken from Dupeux *et al.* [42]

Following the proposed jet thrust mechanism, the same group made a later clarification following the further careful consideration of the vapour flow behaviour beneath the Leidenfrost body. This was deemed to be critical for properly discriminating between the viscous stress drag and the vapour rocket mechanisms. To avoid the experimental error induced by liquid deformation, dry ice was selected as the subject of their investigation [42]. Small glass beads were chosen as tracers to visualise the vapour flow. Tracking the displaced beads confirmed that the vapour flow was isotropic on a flat plate but anisotropic on a ratcheted surface. The majority of the beads had a positive x velocity (self-propelled direction on the order of 10 cm/s), though some fell off the step backwards, a similar conclusion to that of Linke *et al.* [24]. Furthermore, they found that the beads escaped from the ratchets symmetrically perpendicularly to the direct of motion (figure 2.12), with almost the same velocity as the forward velocity. This effect occurred within each individual ratchet, meaning that a net gas flow in the positive x direction was produced. Consequently, the dry ice platelet above the ratchets was dragged along the descending slope of the teeth. Based on the experiments, they calculated the Reynolds number to be around 0.1. Here, they defined the Reynolds number using $Re = (\rho U^2 / \lambda) / (\eta U / h_0^2)$, which compared inertia in the numerator with viscous resistance in the denominator. This result aligned with the viscous stress mechanism proposed by Linke *et al.* [24]. Meanwhile, they clarified that the Reynolds number

had been overestimated in their previous jet thrust study where inertial propelling force was considered.

Their revised model analysis was again in the spirit of the Poiseuille flow, yielding the driving force scaling as:

$$F_f \sim \frac{Mgh}{\lambda} \quad (2.9)$$

In equation 2.9, the thickness of the vapour flow was simply taken as the ratchet height (ε , see definition in figure 2.1c), leading to $h/\lambda \sim \alpha$. Here, λ is the ratchet period (see definition in figure 2.1c) and α is the inclined angle of the teeth relative to the horizontal.

In their effort to explore the mechanism underlying the Leidenfrost self-propulsion a ratchet rectified vapour flow was clearly pictured. The model in equation 2.9 subsequently gives a general overview how the dynamics could be affected by the droplet size (*e.g.* radius R). Yet the deformable nature of a droplet raises the question of whether the model suits a Leidenfrost liquid candidate. Assuming complete deformation, in which the liquid closely reaches the ratchet slope, a vapour thickness model could be established based on the work in reference [79]. For insufficient deformation, the boundary condition for the analytical solution of the effective vapour flow may be changed when considering the component of the accompanied air flow. Beyond that, it is natural to question if a quantitative model could be established, in particular for a deformed liquid candidate.

2.5.4 Additional Considerations Based on Numerical Analysis

Most studies now agree that the evaporated vapour is rectified before dragging the levitated body (whether it is a liquid droplet or solid disc). However, Würger [80] suggested yet an alternative mechanism: gas was directed by the thermal creep that does not rely on droplet evaporation (see figure 2.13). Steffen *et al.* [29] later ‘proved’ the insignificance of the thermal flow component via a numerical simulation of the Boltzmann equation, which confirmed the dominant role of the pressure-driven flow. In particular, the pressure-driven flow also explains the observation of ‘reversible’ Leidenfrost self-propulsion [86, 105], where the vapour is directed in the opposite direction because of the different parameter of the ratchets, resulting

in motion in the ‘opposite’ direction (‘opposite’ direction refers to motion from right to left relative to the ratchets in figure 2.13, whereas the ‘correct’ direction is from left to right).

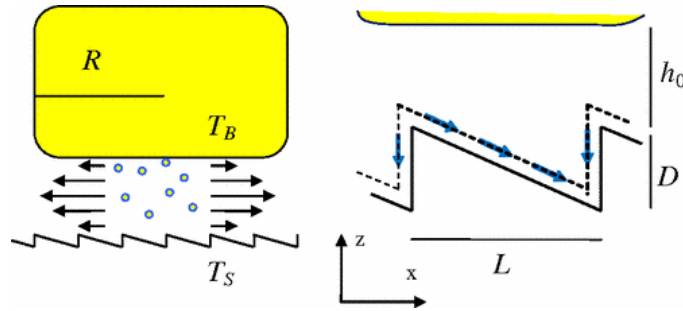


Figure 2.13 – Directed gas flow (blue arrow in the right-hand panel) induced by creep flow. This mechanism does not rely on the droplet evaporation in the left-hand panel. Figure taken from Würger [80]

In line with the viscous mechanism in Section 2.5.3, Baier *et al.* [99] conducted numerical analysis that gives access to the vapour flow in three dimensions, where they aimed to give a definitive quantitative description for solid propulsion [99]. This study provides a detailed flow field including the flow along the declining slope as well as the lateral flow along the groove. It has made a breakthrough to supersede the simple scaling analysis previously conducted [42], which may provide a better understanding of the experimental results moving forward; though the error between the experimental data and predictions by the updated model are still under consideration. Note that this model was only developed for Leidenfrost solids, because the deformation of the liquid will make the analysis more complicated.

2.5.5 Friction

During motion, the primary driving force for propulsion is eventually balanced by friction, a consequence of energy loss due to deformation around the ratchets (liquid) and air resistance (liquid and solid), which ultimately gives rise to the terminal velocity of the Leidenfrost bodies on the heated ratcheted surfaces (since the resisting force generated by friction grows as the velocity increases). Some have applied Stokes’ law to analyse the frictional drag component exerted by the surrounding air [24, 30]. In fact, the air resistance is negligible. The friction resulting from the ambient air is scaled by $\rho v^2 R^2$, having an order of $0.1 \mu\text{N}$, which is 2-3 order of magnitude smaller than the driving force (see the measurement in figure 2.11). Instead, the

main energy loss occurs due to deformation of the liquid around the ratchets and the dissipated kinetic energy as the Leidenfrost liquid droplets strike the ratchets.

Dupeux *et al.* [100] subsequently fabricated a surface with symmetric crenelations (see figure 2.14) to demonstrate the energy loss. As expected, a droplet with an initial velocity decelerated very fast due to the soft strikes against the ratchets. The friction consists of two components. First, the deformed liquid loses kinetic energy when striking the ratchets, and the kinetic energy scales as $\rho_L R^2 \varepsilon v^2$ at the volume $R^2 \varepsilon$. Second, the deformed liquid has to overcome potential energy barriers $\rho_L g R^2 H^2$. It corresponds to a friction scaling as equation 2.10 at a displacement of λ , where b_1 & b_2 are numerical coefficients to be fitted from experiments:

$$F_b = b_1 \rho_L g R^2 \frac{\varepsilon^2}{\lambda} + b_2 \rho_L R^2 v^2 \frac{\varepsilon}{\lambda} \quad (2.10)$$



Figure 2.14 – Crenelated surface stops a moving droplet. Figure taken from Dupeux *et al.*

[100]

For a Leidenfrost self-propulsion system (see figure 2.6), this area warrants further research to better understand the role of friction. This includes the confirmation of the importance of liquid deformation and further study into how the motion of the droplet influences the friction (*i.e.* sliding and/or rotation). For example, recent evidence for rotation on a smooth hot surface is provided by Bouillant *et al.* [22], where small water droplets were found to self-rotate. Viscous dissipation within these rotating droplets may also need to be taken into account [106, 107].

2.6 Potential Application Proposals

2.6.1 Levitated Microreactors

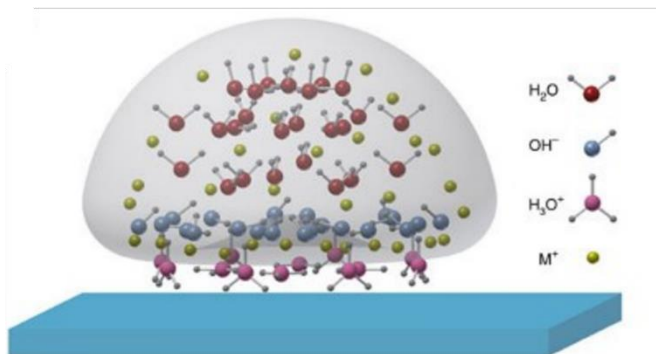


Figure 2.15 Effect of charge separation in a Leidenfrost droplet [108]

Levitation of Leidenfrost droplets inhibits surface contamination and therefore the adsorption of unwanted surface analytes. It is therefore proposed as an additional method to improve the sensitivity analysis in microfluidic devices, *e.g.* for mass spectrometry [109, 110]. Moreover, Lee *et al.* suggested that film boiling is a green-chemistry pathway to produce metal nanoparticles and nanoporous metals by disposing conventional toxic reducing agents [111]. In the study by Bain *et al.* [112], chemical reactions were significantly accelerated in a Leidenfrost droplet because of interfacial effects. There is speculation that temperature gradient in a Leidenfrost droplet [113] would induce an effect of charge separation, as shown in figure 2.15, so as to enhance the process of nanofabrication [108].

2.6.2 Frictionless Transport

Leidenfrost droplets do not contaminate the substrate as they are suspended by a vapour film; the small value of which also makes the motion near-frictionless ($F_b \sim 10 \mu\text{N}$ for $R \sim 3\text{mm}$ [104]). The motion on the heated ratcheted surfaces has a predictable direction with a very appreciable terminal velocity compared to other passive liquid transport phenomena. The simple Leidenfrost cart studied by Ali *et al.* [101] shows that the transported object does not necessarily need to be vaporisable. Theoretically, the ‘wheels’ of this cart can be continuously replenished to enable low-friction transport across heated surfaces. Alternatively, an artificial air flow can also suspend objects and control the propulsion direction; Dan *et al.* [85] designed a substrate with pores for air injection, eliminating the need to supply thermal energy entirely (the underlying principle of the air hockey table). Sugioka *et al.* [114] further proposed a ‘side-

shooter' design that could move droplets at higher velocities (~ 0.15 m/s). Figure 2.16 demonstrates the concept: A stationary droplet (symbol "1", in blue colour) suddenly transformed into a Leidenfrost state by applying a sudden heat flux to the thin-film heater (symbol "3", in red colour), exerting a vapour film between the droplet and the thin-film heater. The vapour film was asymmetrically deformed, which induced asymmetric surface tension forces acting on the droplet. The droplet then set into motion by the external force. Here, the droplet sit on a hydrophobic surface to reduce the pinning effect by contact hysteresis [47]. The droplet propelled with a velocity comparable to that on a ratcheted surface, whilst avoiding the more complex ratcheted surface pattern.

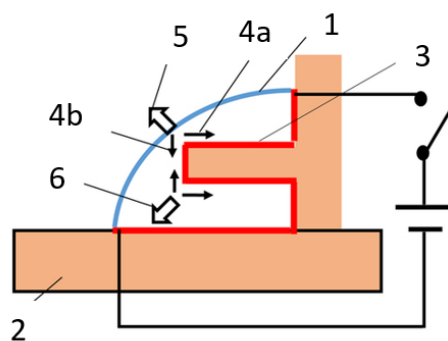


Figure 2.16 – A Leidenfrost side-shooter designed by Sugioka et al. [114] | 1 Water droplet | 2 Hydrophobic substrate | 3 Thin-film heater | 4a&b Surface tension at the corner | 5&6 Net forces acting on the droplet

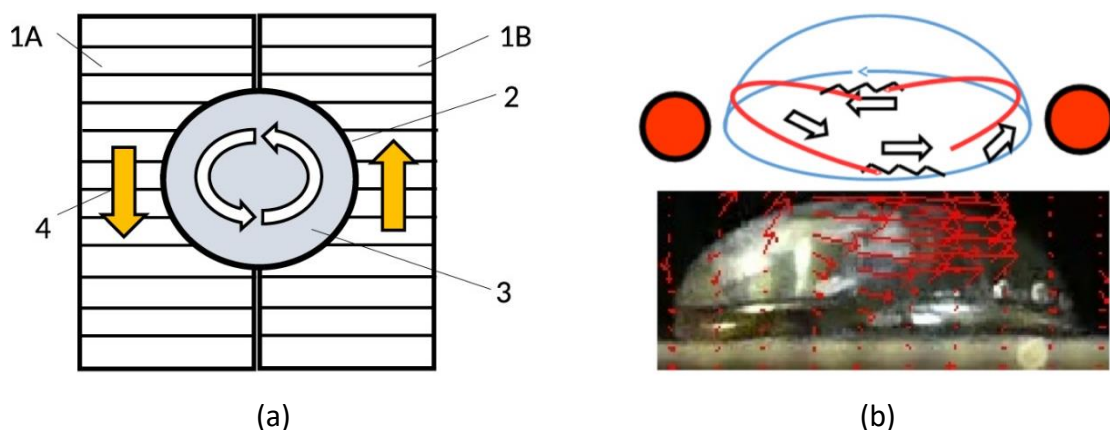


Figure 2.17 – A Leidenfrost mixer. (a) Concept of design | 1A&B Ratcheted substrate placed in an opposite direction | 2 A ring used to constrain the droplet | 3 Rotating water droplet | 4 Ratchets direction. (b) Internal fluid flow via particle image velocimetry (PIV) measurement.

Figure taken from Sugioka et al. [115]

2.6.3 Leidenfrost Mixer

In another example, the new discovery of internal convection in a Leidenfrost droplet inspires a new technique for droplet mixing. Such concept introduced by Sugioka *et al.* [115] was demonstrated in figure 2.17, as called a Leidenfrost mixer. By paring opposing sets of ratcheted surfaces, a Leidenfrost droplet generated convective internal flows to mix pearl pigments in seconds. Whereas no spreading existed in an equivalent stationary water droplet. In comparison with the flow rate in an electrokinetic system (on the order of ~ 1 mm/s), the velocity field in this system has greatly increased to the level of 0.1 m/s, implying the Reynolds number (Re) were increased by a factor of 100 to yield a high theoretical mixing efficiency.

2.6.4 Energy Harvesting

In terms of self-propulsion on a ratcheted surface, the high velocities make it promising for the generation of useful energy from waste heat. Gary *et al.* [31, 32] have subsequently attempted to construct a Leidenfrost heat engine for the generation of electricity. In the initial proof of concept (panels a and b in figure 1.1) [31], asymmetric ratchets were manufactured in a turbine-like surface, where a Leidenfrost solid (which is dry ice) rotated to generate work from the heated surface. Though the efficiency from heat to motion is low ($\sim 10^{-6}$), electricity generation was evidenced through electromagnetic induction. Subsequently, they proposed a heat engine system based on a thermodynamic cycle (panels c and d in figure 1.1) [32]. In this work, a liquid stream rotating on a ratcheted ring served as the rotor of the engine. The consumed liquid can be fed by an external pump, which makes the system continuous. The closed thermodynamic cycle is believed to have potential applications in deep space and planetary exploration as the environment there would potentially benefit the energy efficiency of the system (*e.g.* the vacuum ambient pressure). Further, the typical temperature differences would support different feedstocks (*e.g.* H_2O , CO_2 or CH_4) to support energy generation [32].

2.7 Chapter Summary and Outlook

Liquid droplets (or solid discs) when subjected to the Leidenfrost effect on specially textured ratcheted surfaces exhibit self-propulsion behaviour, provided the droplet/solid covers at least one ratchet period. In general, a liquid droplet may obtain a constant terminal velocity as the deformed liquid loses energy in the face of soft strikes by the rigid ratchets. At millimetre scales, the terminal velocity of liquid droplets is typically ~ 0.1 m/s. Faster

acceleration occurs at intermediate temperatures, where a transition boiling regime enhances the heat transfer rate. Nucleate boiling at lower temperatures tends to inhibit the droplet propulsion, and higher temperatures lead to the full development of an insulating vapour layer that decreases the evaporation rate (film boiling). By further scaling down the saw-tooth ratchets to micron or sub-micron scales, smaller droplets are able to be propelled on the surface at a speed up to 0.4 m/s. Further, superhydrophobic coatings make it possible to reduce the critical temperature for propulsion, even below the boiling point (*e.g.* ~ 77 °C for water), although the velocity tends to decrease in these ultra-low temperature regimes as well.

Inspired by the conventional ratchet designs, other asymmetric textures can also generate propulsion by a rectified vapour flow. Likewise, a tilted solid can also self-propel even on a flat surface. More interestingly, an artificial directed air flow enables propulsion. These studies are helpful to open further opportunities in practical applications.

A Leidenfrost body may acquire a rich number of dynamical behaviours at the same time. When released from a sufficient height, a capillary droplet makes a brief contact with the surface before it bounces back. On a surface with preferential wettability, the droplet spreads in a preferential direction during the brief contact. Herein, a small Leidenfrost droplet can be directed to rebound.

Experimental evidence and numerical simulations have suggested a pressure-driven flow as the mechanism. A quantitative model is still lacking, in particular for a deformable liquid candidate. Current viscous mechanism is limited to a scaled model representation, which is not useful for quantification, prediction, or design. A general model on Leidenfrost self-propulsion together with a friction model analysis may assist to build a model on terminal velocities, which is helpful to propose an optimized ratchet design.

One of the potential exciting applications envisaged in the literature is electricity generation for space exploration. However, it is obvious that the efficiency of this process will be very low because of the dominant energy consumption required to sustain levitation in comparison to other thermodynamic heat engines. Although there is some scope for improving the operating temperature via a combination of changing the operating temperature, using hydrophobic

coatings, and optimisation of the geometries. On the other hand, a Leidenfrost droplet generates convective internal flows, which suggests a promising approach for droplet mixing. It is envisaged that new application will emerge in the future that are better suited to exploit the unusual behaviour of these Leidenfrost self-propulsion devices.

Chapter 3. Methodology

This chapter will describe the experimental setup for analysing Leidenfrost droplet motion and mixing on Leidenfrost rings. This includes descriptions of how experiments were performed to minimise bias, the recording of raw image data using CCD/CMOS cameras with high frame rates, the use of open-source ImageJ (Fiji) software for processing the raw image files, and the automated analysis of the processed images using a custom programme written in MATLAB. The use of MATLAB saves considerable time enabling more experiments to be performed whilst Fiji provides the ability to manual process the results to compare with and validate the efficacy of the automated MATLAB results.

3.1 Design of Devices

The ratcheted surfaces in this project were arranged in a ring shape as shown in figure 3.1 (all purchased from GYROSCOPE.COM and used without further modification). The use of rings instead of linear ratcheted surfaces as commonly used in the literature enables the terminal velocity of the droplets to be reached in a much smaller footprint. Table 3.1 summarises the geometric parameters of the ring designs. The effects of ratchet height (ε), ring diameter, ratchet period (λ), and ratchet shape were considered. The ratchets were either triangular or trapezoidal (having a ‘flat top’). Here, λ_e is used to describe the effective period of the trapezoidal ratchet, namely $\lambda_e = \lambda - |\text{Flat Top Length}|$. Note, the ratchet period at the inner edge (λ_i) of the ring was different to the outer edge (λ_o) as a result of the manufacturing process, so an average value is presented.

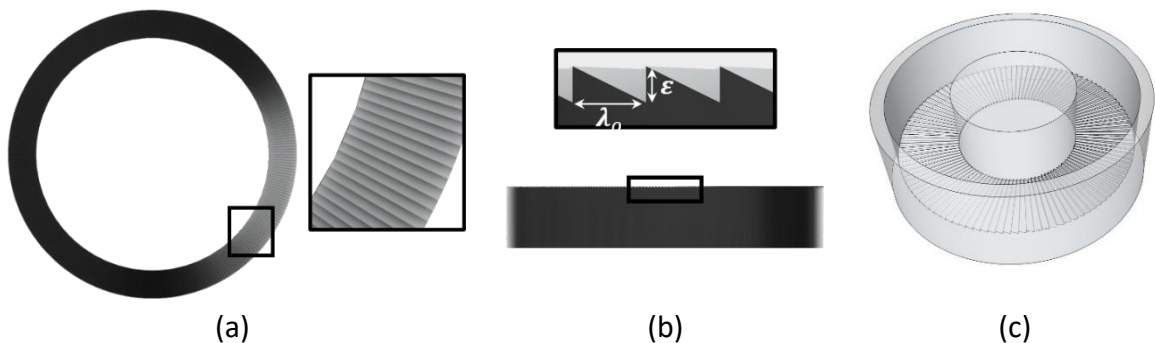






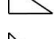
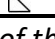


Figure 3.1 – Schematic of the ratcheted rings; (a) top view, (b) side view and (c) 3D view; λ_o and ε are the ratchet period and height respectively at the outer edge

Table 3.1 – Summary of ring geometries used in this study

Ring Design	Outer Diameter (mm)	Inner Diameter (mm)	Ratchet Shape	λ (mm)	λ_e (mm)	ε (mm)	Flat Top Length (mm)
1			o. 	1.05	1.05		-
			i. 	0.85	0.85		-
2	103	83	o. 	1.14	0.87	0.5	0.27
			i. 	0.91	0.86		0.05
3			o. 	3	3		-
			i. 	2.41	2.41		-
4	38	18	o. 	1.07	0.79	0.4	0.28
			i. 	0.5	0.5		-

o. and *i.* represent the outer and inner side of the ring respectively

Other surfaces such as ‘flat’ aluminium sheets and flat super hydrophobic paper were also used for benchmarking the Leidenfrost ring behaviour, in order to separate the contributing factors towards droplet mixing. The ‘flat’ aluminium sheet was slightly curved to form a shallow basin to prevent the droplets from moving (see figure 3.2).

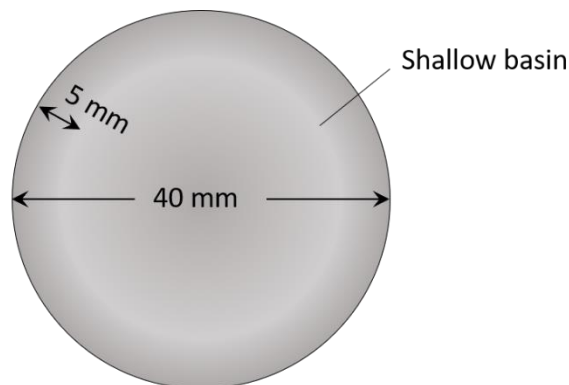


Figure 3.2 – Top view of the aluminium sheet with shallow basin; used to isolate thermally-driven diffusive mixing from convective mixing on the Leidenfrost rings

3.2 Droplet Motion Study

3.2.1 Experimental Procedure

In *Chapter 4*, deionised water droplets with various volumes were used to study the fundamental dynamics of the Leidenfrost self-propulsion on the ratcheted rings. The ratcheted surface was heated by a hot plate (Bibby Sterilin, HC502). In order to ensure a full Leidenfrost regime [77], droplet motion at temperatures of 300 °C, 350 °C, 400 °C and 450 °C were tested. A thermocouple (Fisher Scientific; operating range: -200 to ~1370 °C) was used

to measure the surface temperature prior to each experiment by contacting the thermocouple with the surface. Experiments commenced after the surface temperature readings stabilised.

The droplets were deposited onto the surface using a micro-pipette. There is a 'standard' direction of self-propulsion on these ratcheted surfaces, defined as left to right relative to the geometry in figure 3.1b (based on observations from the experiments and wider literature [24, 42, 76, 116, 117]). Therefore, in this study the droplets were deposited so that they had an initial negative velocity (moving from right to left in figure 3.1b). These droplets would then rapidly decelerate, before coming to a stop, then accelerating in the 'positive' direction (moving from left to right in figure 3.1b). This method ensured the removal of experimental bias from the droplet acceleration measurements (preventing any uncontrolled and unwanted initial 'positive' velocity).

The droplet motion was recorded using a high-speed camera that captured image sequences with a 20 ms timestep interval. A stabilized light source (Fibreoptic Lightguides, model 21727) was applied to ensure the brightness in each image was stable, which was found to be important for the automatic image analysis. Droplet velocities (v), top-down contact areas (A), droplet centre-of-mass, and droplet acceleration (a) were subsequently available from the image analysis. ImageJ (Fiji) and a custom MATLAB program were used to automatically detect the moving droplets by tracking the centre of mass.

3.2.2 Automatic Droplet Motion Detection

In ImageJ (Fiji) [118], two separate sequences of images were imported; one sequence containing the moving droplet and one sequence with a 'blank' ring (no droplet), as shown in sub-figures 3.3a and 3.3b. Both sequences were then cropped to remove the background, leaving just the rings. The sequence without a moving droplet was then subtracted from the sequence with a moving droplet using the inbuilt image calculator function, which removed the pixels of the ring containing no droplets, leaving pure droplet data as shown in figure 3.3c. These images were then converted to a greyscale 8-bit type, smoothed, and transformed to a binary-type image as shown in figure 3.3d. Here, the droplet was now defined by the dark pixels in the image. After this, the further image processing continued in MATLAB.

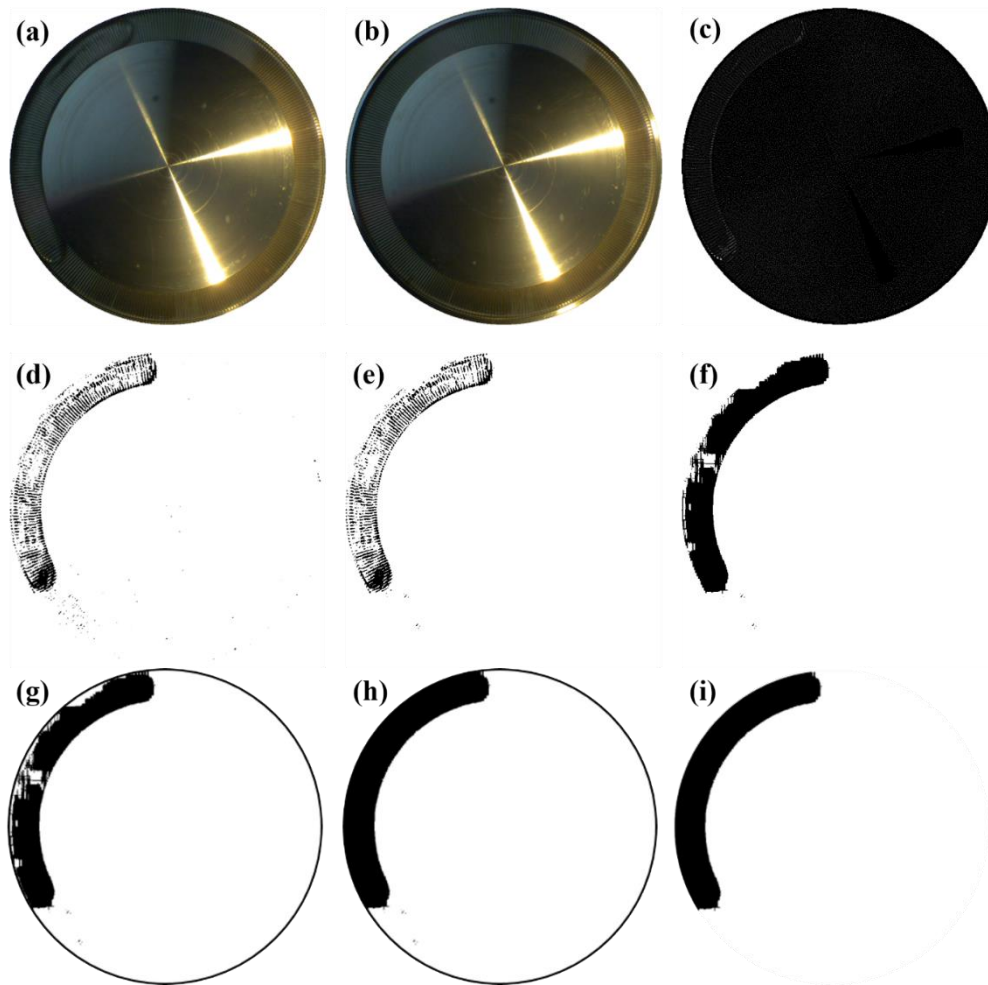


Figure 3.3 – Image analysis sequence using ImageJ (Fiji) (a-d) and MATLAB (e-i)

In MATLAB, the images were read as separate matrices where the droplet and the background pixels were differentiated by their binary values (where 0 = droplet, 1 = background). The custom programme (see *Appendix A*) started with the definition of a threshold filter to remove the random noise from the droplet (observable in figure 3.3d). Here, the pixels around each point (i, j) in the image matrix were analysed, where the total value of the pixels in a predefined scanning area were summed and compared to a threshold value Th (the size of this scanning area was tuned to best suit the particular image – e.g. 34x34 pixels were used in Figure 3.4). If the total value was lower than Th , any dark pixels were considered to be noise rather than the actual droplet. A 3x3 pixel filter matrix was subsequently defined around (i, j) , and any values in this filter were changed to be white (value of 1).

In a second pass, a smaller scanning matrix (e.g. 10x10 pixels) and a larger filter matrix (6x6 pixels) were applied to refine the removal of noise. This preserved nearly all of the pixels corresponding to the droplet whilst eliminating the noise (figure 3.3e). The threshold values

were defined through trial and error, with $Th_1 = 31$ and $Th_2 = 15$ often used for the two filter passes in this research. This method was suitable because of the lower density of the noisy dark points compared to droplet pixels.

The dark points in the droplet then needed to be filled-in to remove the white space, as observable in figure 3.5. The white space between any two dark points along a horizontal line (e.g. point (i, j) and point $(i, (j + 30))$) were first filled-in by defining a vector of dark points between these two points. A similar function was applied in the vertical direction, which resulted in a single filled-in region of dark points corresponding to the droplet (figure 3.3f). By constraining the position of the two candidate points, errors caused by the ‘false’ point connection would only occur when the droplet image appeared in the x - or y -axis. Besides, the error connections were usually very small since the vectors were defined in a scale much smaller than the frame size.

However, there was still some white-space left inside the droplets which needed to be corrected. First, the boundary of the ring was added to the images based using the equation for a circle (equation 3.1).

$$(i - i_0)^2 + (j - j_0)^2 = \left(\frac{i_{max}}{2}\right)^2 \quad (3.1)$$

Here, (i_0, j_0) represents the centre of the ring and i_{max} is the maximum number of the row in the image matrix. As shown in figure 3.3g, the white spaces could be labelled as separate regions, from which the smaller regions were removed by defining a threshold value of area, producing a near-complete outline of the droplet in that particular video frame (figure 3.3h). This was deemed to be a valid solution because the droplet moved along the outer edge of the rings due to the centripetal force. A similar approach of region separation was applied to the dark points to remove the extra noise and produce the final isolated droplet after removing the boundary (figure 3.3i).

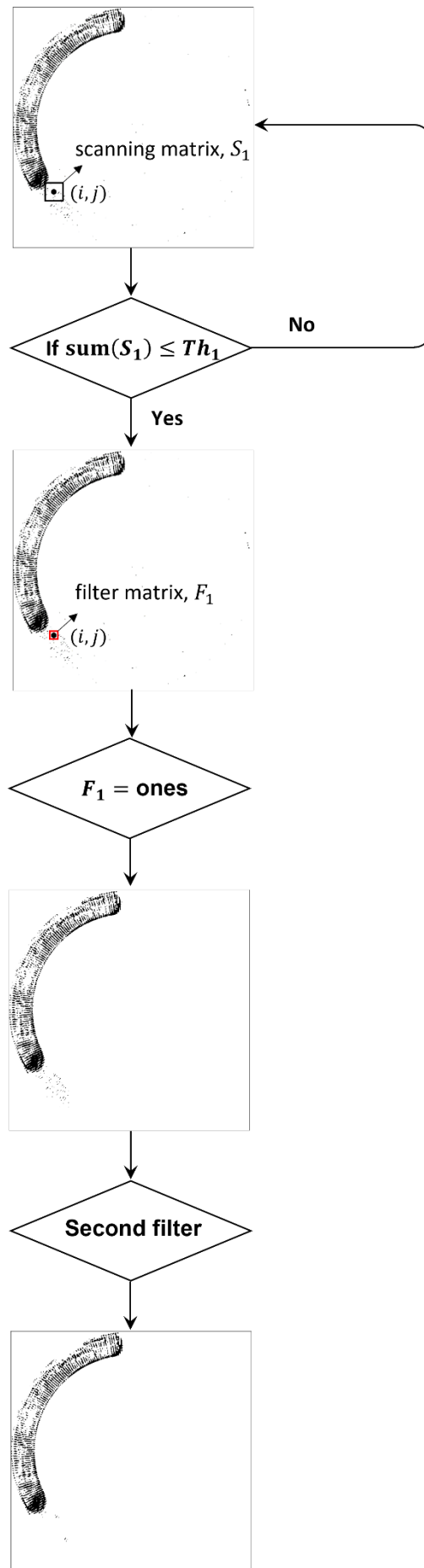


Figure 3.4 – Schematic procedure to filter noise according to the custom filter

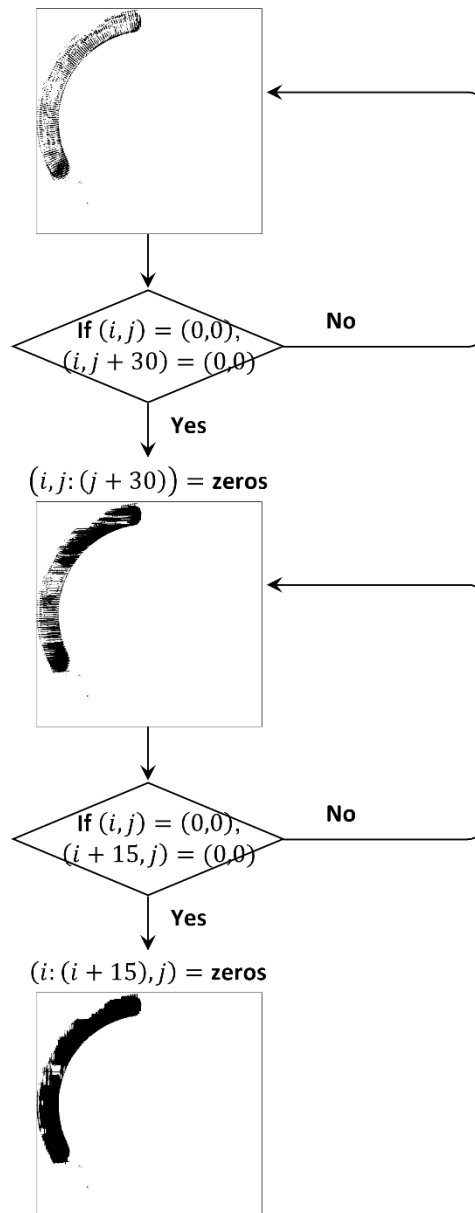


Figure 3.5 – Schematic procedure to fill-in the droplet pixels

The motion of each droplet could then be automatically tracked via another custom programme (*Appendix B*). Here, the angular motion of the droplet was tracked by the centre of mass, which could be defined by 2D coordinates: $P_n(X_n, Y_n)$. Specifically, the centre of mass was calculated using equations 3.2 & 3.3, where n denotes the order of the image to be processed, N_n is the number of the dark points that represent the droplet in the n_{th} image and (x_i, y_i) are a pair of coordinates of the i_{th} point in the droplet. For reference, figure 3.6 shows the centres of mass detected in two successive video frames, where the angle between them defines the motion.

$$X_n = \frac{\sum_{i=1}^{N_n} x_i}{N_n} \quad (3.2)$$

$$Y_n = \frac{\sum_{i=1}^{N_n} y_i}{N_n} \quad (3.3)$$

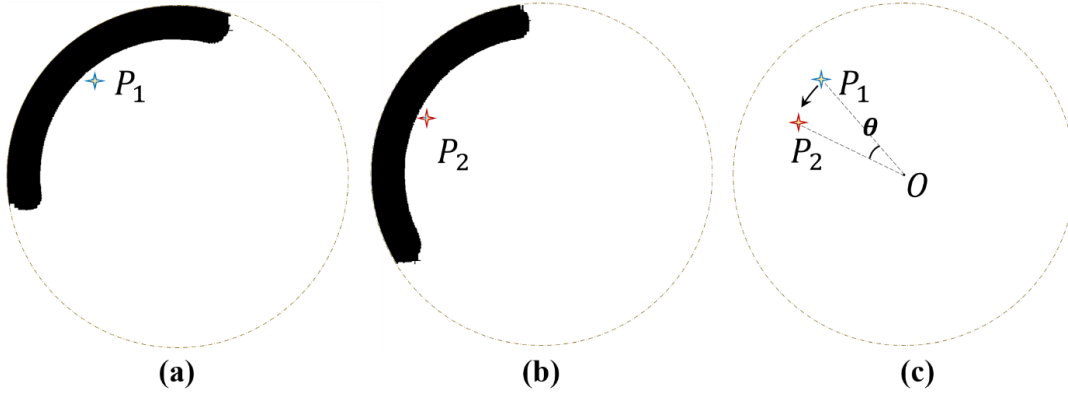


Figure 3.6 – Automatic droplet detection via MATLAB; (a) and (b) show the droplet position at times t_1 and t_2 . The corresponding centre of mass was detected at points P_1 and P_2 respectively; (c) sketch of droplet trajectory (based on centre of mass); θ is the angle (rad) that the droplet rotated during this time

The droplet's angular displacement (θ_n) between two successive images was calculated according to the changed slope of the line OP_n (see figure 3.6c), where $O(x_0, y_0)$ is the centre of the ring (i.e. centre of the circular motion):

$$\theta_n = \tan^{-1} \frac{k_n - k_{n-1}}{1 + k_{n-1}k_n} \quad (3.4)$$

Here, k_n and k_{n-1} are the slopes of the line OP_n and OP_{n-1} :

$$k_n = \frac{Y_n - y_0}{X_n - x_0} \quad (3.5)$$

$$k_{n-1} = \frac{Y_{n-1} - y_0}{X_{n-1} - x_0} \quad (3.6)$$

The angular velocity (ω_n) of the droplet was then calculated as the ratio of the displaced angles over time:

$$\omega_n = \frac{\theta_n}{t_2 - t_1} \quad (3.7)$$

Assuming the rotating droplet has a global angular velocity (ω_n), equation 3.8 describes the tangential speed of each smaller mass (e.g. the pixel point captured in the image). Here, $r_{i,n}$ is the distance of the particle from the ring centre (calculated in equation 3.9).

$$v_i = \omega_n r_{i,n} \quad (3.8)$$

$$r_{i,n} = \sqrt{(x_i - x_o)^2 + (y_i - y_o)^2} \quad (3.9)$$

The total kinetic energy of the rotating droplet is integrated as the sum of the kinetic energy of each smaller mass, yielding an expression in terms of the angular velocity by substituting equations 3.8-3.9 to equation 3.10:

$$E_{v,n} = \sum_{i=1}^N \frac{1}{2} m_i v_i^2 \quad (3.10)$$

Alternatively, the droplet kinetic energy is translationally expressed by

$$E_{v,n} = \frac{1}{2} M v_n^2 \quad (3.11)$$

where M and v_n respectively denote the droplet mass and droplet velocity. Assuming each smaller mass (i.e. each pixel point) has similar individual mass m_i , which means $M = N m_i$, the droplet linear velocity is expressed by equation 3.12 according to a classical energy balance.

$$v_n = \omega_n \sqrt{\frac{\sum_{i=1}^N [(x_i - x_o)^2 + (y_i - y_o)^2]}{N}} \quad (3.12)$$

Accordingly, the effective radius of the droplet rotation is defined by equation 3.13a.

$$R_n = \sqrt{\frac{\sum_{i=1}^N [(x_i - x_o)^2 + (y_i - y_o)^2]}{N}} \quad (3.13a)$$

For a system with little difference of the distances $r_{i,n}$ (in respect to the order of magnitude of $r_{i,n}$), the effective radius can be simply estimated by equation 3.13b. The suitability of either method would be dependent of the application and the level of accuracy required. For instance, if $r_i = [14,15,16,17,18,19]$, equations 3.13a and 3.13b yield $R_n=16.59$ and $R_n=16.50$ respectively, with a difference of only 0.5%!

$$R_n = \frac{\sum_{i=1}^N \sqrt{[(x_i - x_o)^2 + (y_i - y_o)^2]}}{N} \quad (3.13b)$$

The top-down contact area of the droplet (A_n) was computed by calculating the total number of pixels in the whole image, and calculating the fraction of the image taken up by the pixels of the droplet (equation 3.14). The droplet pixels were detected using a threshold in the programme (*i.e.* the dark points in figure 3.3i). Similarly, the total imaged ring area was determined by counting the pixels that the ring image covered. In equation 3.14, i_{max} and j_{max} are the maximum numbers of the row and column in the image matrix, representing the length of the ring image in horizontal and vertical direction respectively. Technically, i_{max} equals j_{max} because the ring had a circular design. D is the actual outer diameter of the ring.

$$\frac{A_n}{D^2} = \frac{N_n}{i_{max} \cdot j_{max}} \quad (3.14)$$

3.2.3 Programme Validation

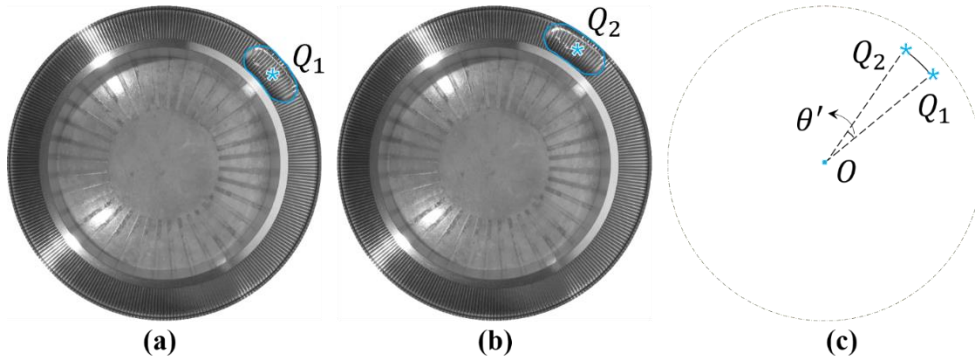


Figure 3.7 – Manual droplet detection by ImageJ (Fiji); (a) and (b) show a droplet at two different times; (c) sketch of the droplet's trajectory according to the manual detection, θ' is denoted as the displaced angle.

In ImageJ (Fiji) the droplet was manually detected to validate the automated detection programme described in Section 3.2.2. Figure 3.7a & 3.7b show two example images where the droplet position was tracked by manually selecting the droplet's centre of geometry (denoted as $Q_n(X'_n, Y'_n)$), while the top-down contact area was measured through the manual outline of the droplet.

The droplet's angular displacement (θ'_n) between two successive images was similarly calculated according to the changed slope of the radius OQ_n :

$$\theta'_n = \tan^{-1} \frac{k'_n - k'_{n-1}}{1 + k'_{n-1}k'_n} \quad (3.15)$$

Where k'_n and k'_{n-1} are the slopes of the radius OQ_n and OQ_{n-1} :

$$k'_n = \frac{Y'_n - y_o}{X'_n - x_o} \quad (3.16)$$

$$k'_{n-1} = \frac{Y'_{n-1} - y_o}{X'_{n-1} - x_o} \quad (3.17)$$

The angular velocity (ω_n) of the droplet was again calculated as the ratio of the displaced angles over time (equation 3.18), with the corresponding linear velocity obtained by multiplying this by the radius of the circular motion (equation 3.19).

$$\omega'_n = \frac{\theta'_n}{t_2 - t_1} \quad (3.18)$$

$$v'_n = \omega'_n R'_n \quad (3.19)$$

This radius was just the distance of OQ :

$$R'_n = |OQ_n| = \sqrt{(X'_n - x_o)^2 + (Y'_n - y_o)^2} \quad (3.20)$$

The top-down contact area (A'_n) was computed after the area scaling factor of the image was set according to equation 3.21. The actual contact area (A_n) was simply determined by multiplying the droplet area in pixels by this scaling factor.

$$'scale' = \frac{i_{max} j_{max}}{D \quad D} \quad (3.21)$$

Examples of the results are plotted in figure 3.8, which shows there was an excellent agreement between the manually and automatically detected results. Error analysis, according to equations 3.22 & 3.23, quantified the similarity. Here, $\bar{\eta}_v$ and $\bar{\eta}_A$ are the averaged relative errors of the velocity and area respectively.

$$\bar{\eta}_v = \frac{100\% \times \sum_i^n \frac{v_n - v'_n}{v'_n}}{n} \quad (3.22)$$

$$\bar{\eta}_A = \frac{100\% \times \sum_i^n \frac{A_n - A'_n}{A'_n}}{n} \quad (3.23)$$

(a)

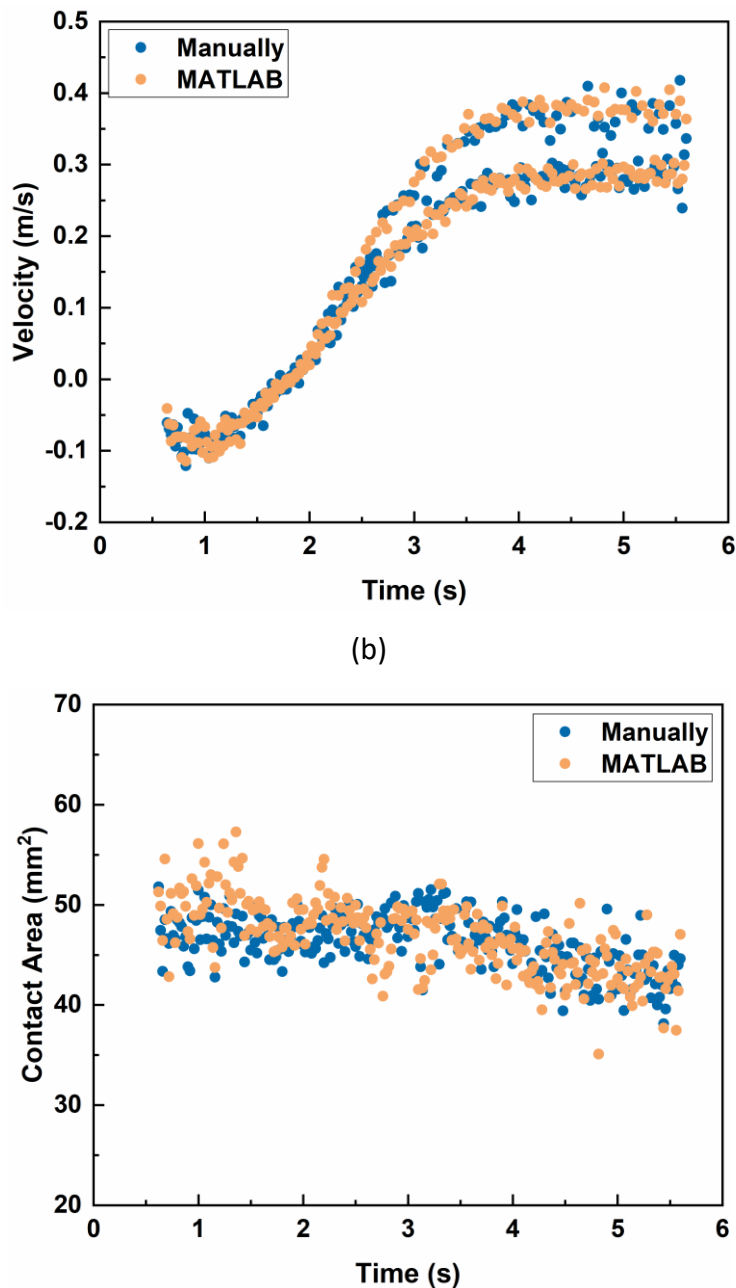


Figure 3.8 – Programme Validation for Automatic Motion Analysis. Example for a water droplet of $150 \mu\text{L}$ on ring design 4 at 400°C ; (a) droplet velocity trend with an average error of -1.29% according to equation 3.22; (b) top-down contact area of the droplet with an average error of 3.82% according to equation 3.23

3.3 Droplet Mixing Study

3.3.1 Experimental Procedure

A coloured dye was initially used to study the mixing efficiency by observing its spread within large self-propelling deionised water slugs. This dye comprised a mixture of food colour (PME, sky blue) with deionised water and had a density of $\rho_b = 3 \text{ g/L}$. Hence, the system is homogeneous and all in the aqueous phase. Mixing was investigated by depositing a small

dye droplet (60 μL) onto the ratcheted surface so that it would then collide with another larger deionised water slug (volume of 600 μL to 1500 μL) already in motion on the ring. Both droplets had similar relative velocities in each group of experiments. The Leidenfrost mixing was studied at surface temperatures of 400 $^{\circ}\text{C}$ and 300 $^{\circ}\text{C}$. A high-speed camera was used to observe the mixing process with an 8-10 ms timestep sampling interval. A ring light (6.2 inch) was set above the ratcheted ring to provide uniform illumination to minimise the influence on colour detection (critical for properly observing the mixing times).

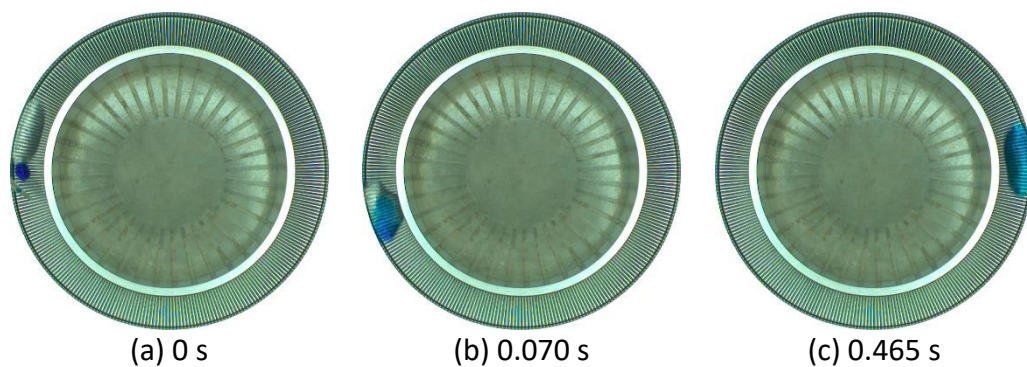


Figure 3.9 – An example of mixing process showing colour difference caused by the mixing

As shown in figure 3.9, the colour of the two droplets were notably different prior to collision (figure 3.9a). The colour difference gradually diminished over time during mixing (figure 3.9b), until the dye was completely mixed with the slug resulting in a homogeneous colour (figure 3.9c). Here, the pixel values within the droplet had a significant deviation from the mean colour at the start of collision, whereas little difference existed once mixing was complete. Accordingly, the boundary of the droplet field was selected as the region of interest (ROI) and the standard deviation (σ) of the pixel values within this ROI was used to assess the mixing process. The standard deviation would decrease during mixing then reach a minimum and stabilise, indicating the end of the mixing process. A custom programme written by MATLAB was developed to automatically detect the colour change.

Similar droplet mixing experiments were performed on a 'flat' aluminium surface and hydrophobic paper for benchmarking. The 'flat' surface was placed on the hotplate and heated to 400 $^{\circ}\text{C}$ to isolate the effect of thermally-driven diffusion. The mixing study on the hydrophobic paper was performed at room temperature ($\sim 8-10$ $^{\circ}\text{C}$), and these results were

used to isolate the effects of diffusion. The same custom programme for colour detection was used for all surfaces.

3.3.2 Automatic Colour Detection

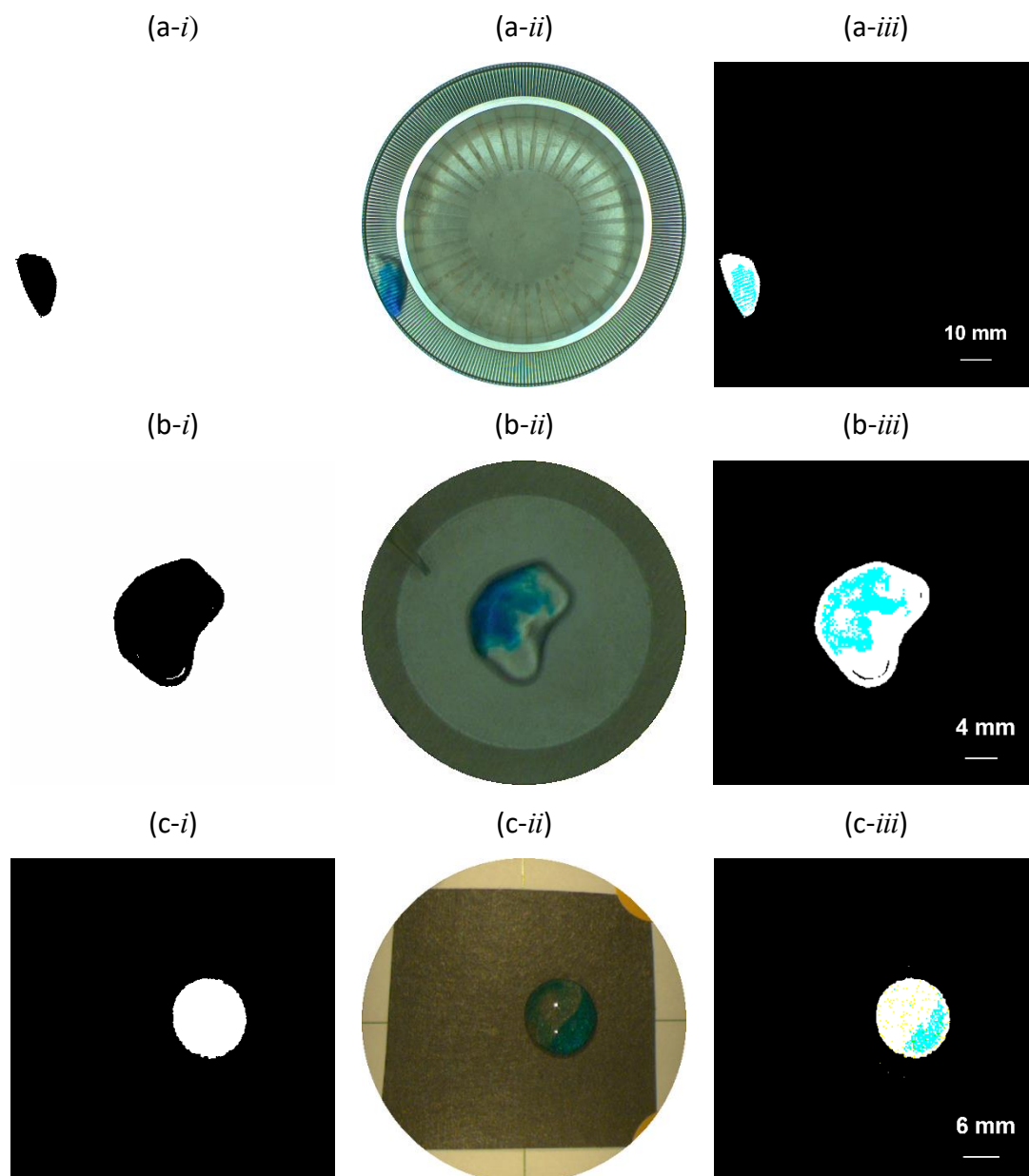


Figure 3.10 – Droplet colour/mixing detection using the RGB model | (a) Leidenfrost ring, (b) planar aluminium sheet, (c) hydrophobic paper

The same droplet detection approach to the one reported in Section 3.2.2 was first used to select the ROI for the colour detection analysis (figure 3.10a-*i*). This also used the binary image format (where 0 = droplet, 1 = background). In the second phase of the analysis, a custom image calculator was written in MATLAB which compared these binary images to the original

ones using equation 3.24 (see *Appendix C*). Here, I_0 , I_1 and I_2 are the matrices that represent the original images (figure 3.10a-ii), the binary images (figure 3.10a-i) and the resulting images (figure 3.10a-iii) respectively. Hence, the ROI in the coloured model in figure 3.10a-iii would reflect the internal mixing characteristics of the droplet.

$$I_2 = I_0 - I_0 * I_1 \quad (3.24)$$

$$I_{gray} = \frac{1}{3}(I_{2,red} + I_{2,green} + I_{2,blue}) \quad (3.25)$$

As known, a specific colour can be expressed by an RGB colour model, which in turn aims to reproduce the colour. The blue shades are consisted of a number of colour codes (not only (0,0,255)). Therefore, it may be not sufficient to consider one blue channel in terms of the colour difference. For simplicity, a simple grayscale matrix (I_{gray}) was defined according to equation 3.25, in order to avoid individual analysis of the three colour matrices (red- $I_{2,red}$, green- $I_{2,green}$, and blue- $I_{2,blue}$).

The same ROI detection and RGB function was also applied to process the images from the 'flat' aluminium surface and hydrophobic paper benchmarks (figure 3.10b & 3.10c respectively). The processing time of these benchmarks was shorter because fewer images were captured.

The standard deviation (σ) of the grayscale image matrix captured the overall colour data distribution in each image of the moving droplet [119]. In the custom calculator (*Appendix C*), the pixel number within the ROI was represented as $N_{StdD,n}$ in the n_{th} image. The corresponding pixel value within the ROI was denoted as $D_{StdD,i}$ for the i_{th} pixel. Therefore, the standard deviation within the ROI in the n_{th} image was defined in equation 3.26.

$$\sigma_n = \frac{\sqrt{\sum_{i=1}^{N_{StdD}} (D_{StdD,i} - \overline{D_{StdD}})^2}}{N_{StdD}} \quad (3.26)$$

Here, $\overline{D_{StdD}}$ is the mean of the counted pixel values within the ROI:

$$\overline{D_{StdD}} = \frac{\sum_i^{N_{StdD}} D_{StdD,i}}{N_{StdD}} \quad (3.27)$$

3.3.3 Program Validation

In ImageJ (Fiji) [118], the ROI from the original images was manually outlined. The standard deviation of the selected ROI was then directly measured in the grayscale image format (equation 3.28). An example of the manually measured result is shown in figure 3.11, showing a very close agreement with the automated analysis.

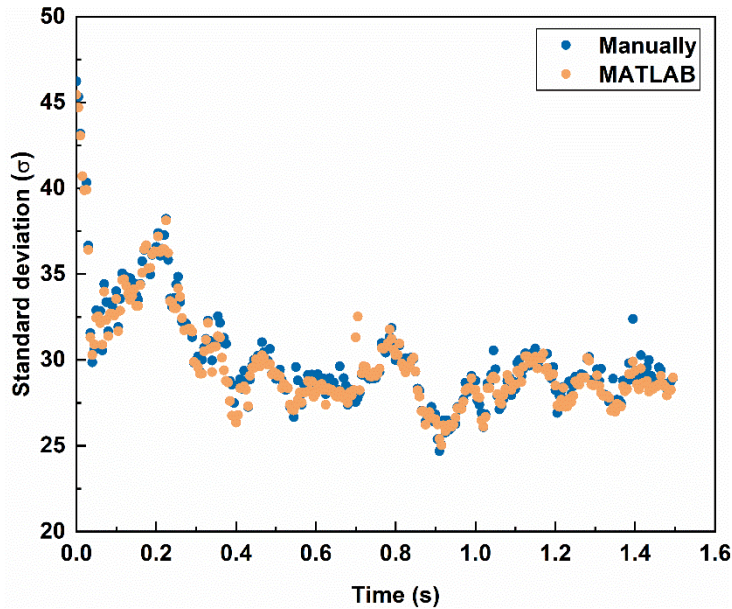


Figure 3.11 – Validation of automated colour detection (droplet volume of 600 μL , ring 2, surface temperature of 350 $^{\circ}\text{C}$). In this example the automated programme differed from the manually calculated standard deviation by just 0.75%

Quantitative error analysis (equation 3.28) further confirmed the efficiency of the programme. Here, σ_n is the standard deviation calculated by the custom programme for the n_{th} image, σ'_n is the corresponding value measured by ImageJ (Fiji), and $\bar{\eta}_m$ is the averaged relative error between analysed images.

$$\bar{\eta}_m = \frac{100\% \times \sum_i^n \frac{\sigma'_n - \sigma_n}{\sigma'_n}}{n} \quad (3.28)$$

3.3.3 Mixing Time Definition

As expected, the standard deviation within the ROI was at a maximum when the droplets initially merged, then the standard deviation decreased over time toward a steady state value as mixing occurred (figure 3.12a). As seen in figure 3.12b, the dataset tracking only the blue channel does not reflect much about the colour diffusion.

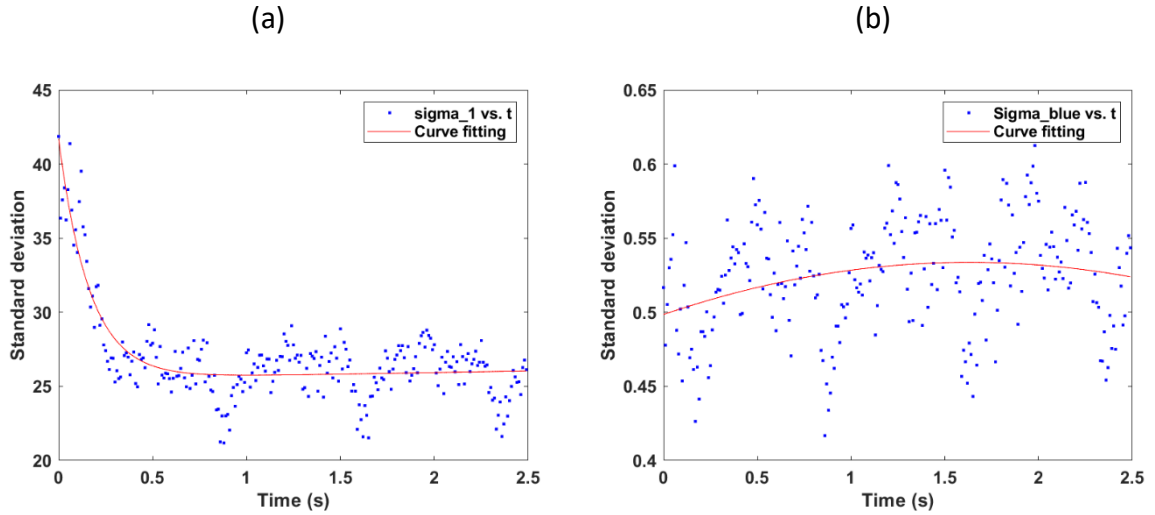


Figure 3.12 – Curve fitting for droplet mixing data (large droplet volume of 400 μL , dye droplet volume of 60 μL , ring 1, surface temperature of 400 $^{\circ}\text{C}$). (a) is a result of the data analysis in grayscale matrix, and (b) records only the blue channel.

It was expected that the measured standard deviation of the colour should become constant once mixing was complete. However, as shown in figure 3.12, the standard deviation value fluctuated with a stable amplitude and frequency once it reached steady state due to unavoidable brightness fluctuations produced by the light source in the high-speed camera videos. To remove the influence of this behaviour, a simple curve fitting application in MATLAB was applied (red line in figure 3.12, chosen 2-term exponential model). The mixing time, t_m , was subsequently defined at the point where the standard deviation decreased by 95% from its original value (equation 3.29) [120, 121]. Here, σ_{max} and σ_{min} are the maximum and minimum values of the fitted curve.

$$\sigma(t_m) = \sigma_{max} - 0.95 * (\sigma_{max} - \sigma_{min}) \quad (3.29)$$

Note, mixing was typically complete within only a few seconds (see figure 6.6 in *Chapter 6*), but the droplet's evaporation occurred on the order of minutes according to experimental observations. This means that the mixing process occurred on a much faster timescale than evaporation, so the data trends subsequently reported are unlikely to be influenced by droplet evaporation effects.

3.4 Chapter Summary

Leidenfrost self-propulsion and Leidenfrost mixing analysis were performed on four ratcheted ring designs with different diameter, shape, and ratchet ratio (ratio of ratchet period to ratchet height). A high-speed camera was used to record the motion of droplets and the dye diffusion process as droplets collided. The effects of droplet volume and surface temperature were studied, and benchmarked against planar surfaces. The numerous digital images were processed through a custom programme written in MATLAB which automated the analysis of droplet motion and colour detection. Comparing with the time-consuming manual analysis performed in ImageJ (Fiji), the programme has an average error of no more than 5%. For the droplet motion analysis, the programme could track the centre of mass of the droplets (to define the angular velocity) and calculate the droplet's top-down contact area. For the mixing analysis, the standard deviation of the pixel values within the droplet area was isolated, and used to define the mixing time.

Chapter 4. Novel Analytical Model for the Leidenfrost Self-Propulsion

The origin for the Leidenfrost self-propulsion phenomenon has been debated [42, 79, 80] since its first publication [24], and there has not yet been a first principles model description that perfectly matches nor explains experimental observations. The viscous mechanism due to a pressure-driven vapour flow appears to be the dominant phenomena behind droplet self-propulsion [29, 42]. Some quantitative understanding of the motion has also been obtained by neglecting liquid deformation by replacing the liquids with rigid Leidenfrost solids (*e.g.* dry ice) [99]. Although this latter study provides a 3D description of the flow field, the error between the experimental data and model predictions is still subject to further interpretation because large errors are observable. Ultimately, the existence of a liquid droplet model is still lacking, affecting the progress of potential applications of these Leidenfrost devices such as their use as heat engines to generate electricity [31, 32] or as a new means to move and mix liquids for flow chemistry [115].

In this chapter, a new analytical model that can be generalised to describe the self-propulsion phenomenon for both solid and liquid Leidenfrost bodies is described. Herein, the liquid deformation around the ratchets will be taken into account for the first time. A detailed force analysis in response to the deformation has been performed in order to find a quantitative description of the driving force. This new model supersedes the limited scaling analysis already conducted in the literature [42] by revealing how the ratchet geometry influences the driving force, showing the individual influence of droplet size, ratchet design, operating temperature and liquid deformation on the dynamics of the motion. This new quantitative model can be used to guide the construction of novel Leidenfrost devices for use as heat engines to generate electricity, or for flow chemistry applications.

4.1 Dynamics for Propulsion

4.1.1 Analysis in a Model

First, a single groove with a width of λ and height of ε is considered (figure 4.1), where a Cartesian coordinate system is set up with x parallel to the slope of the ratchet and y perpendicular to the slope. In this cross-sectional view, C represents the lowest point of liquid within each ratchet, which divides the deformation into two parts. Arc AC follows the slope of the ratchet and is responsible for producing the directed vapor flow that drags the droplet.

Arc BC hangs over the vertical step of the ratchet; the evaporated vapor mainly flows downwards then into and out of the plane of the diagram [24, 42]. C_1 & C_2 are used to describe the resulting proportions of AC & BC , since C can fall anywhere between A and B .

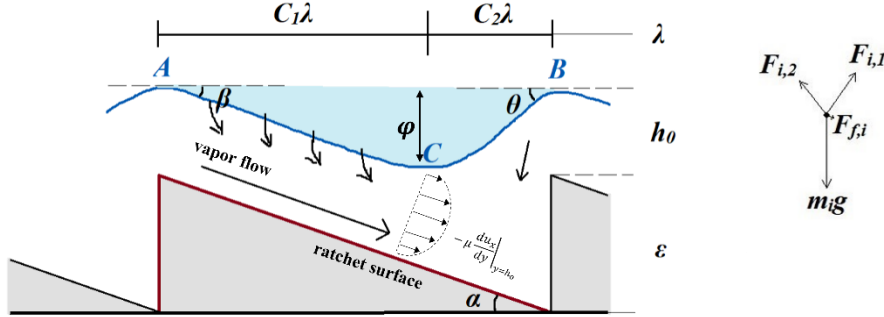


Figure 4.1 – Sketch of a single ratchet period. The droplet sits a distance of h_0 above the ratchet. The droplet has two deformed angles of β and θ . The ratchet has a period of λ and depth of ε . The ratchet period changes from the inner edge (λ_i) to the outer edge (λ_o) whilst the ratchet height (ε) is fixed.

The depth of the deformed droplet (see φ in figure 4.1) is ~ 0.6 mm. This is larger than the ratchet height (ε), so it can be assumed that the deformed arc AC closely approaches the ratchet slope. The underlying reason for $\varphi < \varepsilon$ results from a balance between the hydrodynamic pressure ($\rho_L g H_L$) and the Laplace pressure ($\gamma\varphi/(\pi(\lambda/2)^2)$) [100].

The main forces acting on the droplet are also shown in figure 4.1. $F_{i,1}$ and $F_{i,2}$ are the forces exerted perpendicular to the lines AC and BC respectively as the vapour is expelled from the droplet. The weight force acting downward due to gravity is simply $m_j g$. The driving force produced by the rectified vapour flow is $F_{f,i}$, which will be described by this new model.

The pressure-driven vapour flow along the line AC behaves as a Poiseuille flow in a channel [24, 30, 42]. It is assumed to be incompressible with constant density ρ_v and viscosity μ , and the velocity distribution of the vapour flow is described by Navier-Stokes equations at steady state (where only the x direction is considered). Additionally, gravity also plays a partial effect with $g_x = g \sin \alpha$ and $g_y = -g \cos \alpha$. The continuity equation, and the x and y direction momentum balances for the vapour flow are shown in equations 4.1 to 4.3 respectively:

$$\frac{\partial u_x}{\partial x} = 0 \quad (4.1)$$

$$\frac{\partial P}{\partial x} = \rho_v g_x + \mu \frac{\partial^2 u_x}{\partial y^2} \quad (4.2)$$

$$\frac{\partial P}{\partial y} = \rho_v g_y \quad (4.3)$$

Equation 4.1 implies that the vapour velocity does not vary in the x -direction. Therefore, $\partial^2 u_x / \partial y^2$ in equation 4.2 is a function of y only. Integrating equation 4.3 gives $P = -\rho_v g \cos \alpha y + g(x)$, which then implies that $\partial P / \partial x$ is a function of x only. Therefore, equation 4.2 can be integrated twice with respect to u_x and y to give [103]:

$$u_x = \frac{1}{2\mu} \left(\frac{\partial P}{\partial x} - \rho_v g_x \right) y^2 + c_1 y + c_2 \quad (4.4)$$

Here, c_1 and c_2 are both constants of integration, which can be found by applying the no-slip boundary condition at both $y = h_o$ (the thickness of the vapour layer) and $y = 0$ (at the ratchet surface) (see figure 4.1); *i.e.* the two boundary conditions are $u_x = 0$ at $y = 0$ and $u_x = v$ at $y = h_o$.

$$u_x = \frac{1}{2\mu} \left(\frac{\partial P}{\partial x} - \rho_v g_x \right) (y^2 - h_o y) + \frac{v}{h_o} y \quad (4.5)$$

To derive an expression for dP/dx , it is assumed that the pressure around point C is close to atmospheric pressure since the system is open. Therefore, the overpressure ΔP that induces the directed vapour flow is generated by the supporting force from the slope as shown in equation 4.6 [122].

$$\Delta P = \frac{F_{i,1}}{A_{i,1}} \quad (4.6)$$

Where $A_{i,1}$ is the effective contact area of the deformed liquid lying on the slope of the ratchet, given by $w_{i,1} C_1 \lambda / \cos \beta$. Here, $w_{i,1}$ is the width of the droplet into and out of the plane shown in figure 4.1.

Equations 4.7a and 4.8a show the force balances in the vertical and horizontal directions. The driving force due to the rectified vapour flow, $F_{f,i}$ can be neglected considering its low value as measured experimentally. For example, a droplet of 30 μL weighs $\sim 300 \mu\text{N}$ while its net

driving force is only $\sim 17 \mu\text{N}$ [79]. Equations 4.7b and 4.8b subsequently show the force balances when $F_{f,i}$ is neglected.

$$\text{(vertical)} \quad F_{i,1} \cos \beta + F_{i,2} \cos \theta = m_j g + F_{f,i} \sin \beta \quad (4.7a)$$

$$F_{i,1} \cos \beta + F_{i,2} \cos \theta \approx m_j g \quad (4.7b)$$

$$\text{(horizontal)} \quad F_{i,1} \sin \beta + F_{f,i} \cos \beta = F_{i,2} \sin \theta \quad (4.8a)$$

$$F_{i,1} \sin \beta \approx F_{i,2} \sin \theta \quad (4.8b)$$

Here, m_j represents the part of the mass of the droplet within each single groove. Equations 4.7b and 4.8b can be combined to give:

$$F_{i,1} \approx \frac{m_j g \sin \theta}{(\cos \beta \sin \theta + \sin \beta \cos \theta)} = \frac{m_j g \sin \theta}{\sin(\theta + \beta)} \quad (4.9)$$

The pressure gradient dP/dx acts between points A and C in figure 4.1. The distance between these points is simply $C_1 \lambda / \cos \beta$ by Pythagoras. Therefore, the pressure difference can be approximated as follows:

$$\frac{dP}{dx} \approx -\frac{\Delta P}{\Delta x} = -\frac{F_{i,1}}{A_{i,1} \Delta x} = -\frac{m_j g \sin \theta}{\sin(\theta + \beta) \left(\frac{w_{i,1} C_1 \lambda}{\cos \beta} \right) \left(\frac{C_1 \lambda}{\cos \beta} \right)} \quad (4.10)$$

Substituting this into equation 4.5 gives the vapour velocity as a function of the vertical distance away from the ratchet, which also depends on the liquid/vapour properties (θ , β , m_j , ρ_v , and C_1), ratchet geometry parameters ($w_{i,1}$, λ , and α) and gravity (g).

$$u_x = \frac{1}{2\mu} \left(\frac{m_j g \sin \theta \cos^2 \beta}{w_{i,1} C_1^2 \lambda^2 \sin(\theta + \beta)} + \rho_v g \sin \alpha \right) (h_o y - y^2) + \frac{v}{h_o} y \quad (4.11)$$

As shown in figure 4.1, there is a no-slip boundary condition between the rectified vapour flow and the droplet. Therefore, the corresponding driving force within each groove, $F_{f,i}$, is the result of the shear force at the boundary, where $y = h_o$:

$$\begin{aligned} F_{f,i} &= -\mu \frac{du_x}{dy} A_{i,1} \Big|_{y=h_o} \\ &= \frac{h_o}{2} \left(\frac{m_j g \sin \theta \cos \beta}{C_1 \lambda \sin(\theta + \beta)} + \frac{\rho_v g w_{i,1} C_1 \lambda \sin \alpha}{\cos \beta} \right) - \mu \frac{v}{h_o} \frac{w_{i,1} C_1 \lambda}{\cos \beta} \end{aligned} \quad (4.12)$$

The deformed angles θ & β in equation 4.12 are both related to the height of the deformed triangle ABC (see φ in figure 4.2), implying that:

$$C_1 \lambda \tan \beta = C_2 \lambda \tan \theta \quad (4.13)$$

The proportions of the C_1 and C_2 in equation 4.13 are simply related according to:

$$C_1 + C_2 = 1 \quad (4.14)$$

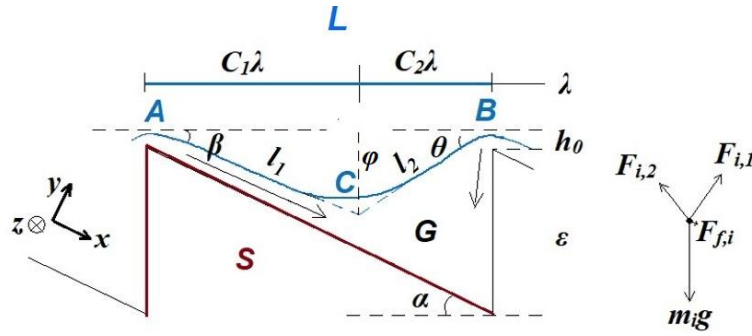


Figure 4.2 – Sketch of a single ratchet period; the droplet sits a distance of h_0 above the ratchet. The ratchet has a period of λ and depth of ε . S is the solid ratchet, L is the levitating droplet and G is gas.

Substitution of equation 4.14 into equation 4.13 gives equation 4.15, that itself can be rearranged to equation 4.16.

$$C_1 \lambda \tan \beta = (1 - C_1) \lambda \tan \theta \quad (4.15)$$

$$C_1 = \frac{\sin \theta \cos \beta}{\sin(\theta + \beta)} \quad (4.16)$$

Applying this result enables the complex geometric terms in equation 4.12 to be simplified into a more practical/convenient expression:

$$F_{f,i} = \frac{gh}{2} \left(\frac{m_j}{\lambda} + \rho_v A_i \frac{\sin \alpha \sin \theta}{\sin(\theta + \beta)} \right) - \frac{\mu A_i}{h_0} \frac{\sin \theta}{\sin(\theta + \beta)} v \quad (4.17)$$

Here it is assumed that the width of the droplet ($w_{i,1}$) is constant, so that A_i (the apparent contact area when looking down on the droplet) is given by $A_i = w_{i,1} \lambda$.

It is only the horizontal component of $F_{f,i}$ that contributes to the forward motion of the droplet, giving an effective driving force of $F_{f,i} \cos \beta$ within each single ratchet. Therefore, the total driving force for the whole droplet is expressed as $F_f = \sum F_{f,i} \cos \beta$ (the sum refers to

the sum of each individual ratchet covered by the droplet)./ Applying this then gives a total driving force of:

$$F_f = \frac{gh_o}{2} \left(\frac{M}{\lambda} + \rho_v A \frac{\sin \alpha \sin \theta}{\sin(\theta + \beta)} \right) \cos \beta - \frac{\mu A \sin \theta \cos \beta}{h_o \sin(\theta + \beta)} v \quad (4.18)$$

where M is the total mass of the droplet and A is the total area of the droplet as viewed from above. The contact area A can either be measured experimentally or approximated for large droplets by considering the ratio of the volume to height V/H_L and assuming that H_L will remain constant [15, 65] (see *Chapter 5*).

In equation 4.18, the sine functions can be replaced by corresponding length functions which provides more intuitive meaning. In figure 4.2, l_1 & l_2 are used to represent the lengths of the two deformed sides. According to the law of sines it follows that $l_1/\sin \theta = \lambda/\sin(\pi - [\theta + \beta])$, meaning $\sin \theta/\sin(\theta + \beta) = l_1/\lambda$. Hence, the second term $\rho_v A \sin \alpha \sin \theta/\sin(\theta + \beta)$ is no more than $\rho_v A(l_1/\lambda)$, where ρ_v is 0.42 kg/m³ at 250 °C (physical properties taken at the average temperature of the surface temperature and the droplet temperature). The first term M/λ is around 4 orders of magnitude larger considering ρ_L is ~10³ kg/m³ at its boiling point, and $H_L \sim 4\text{-}5$ mm and $\lambda \sim 1$ mm. The strict inequalities suggest that the gravity term in equation 4.18 has nearly zero impact on the dynamic process. Equation 4.18 then simplifies to just:

$$F_f = \frac{Mgh_o \cos \beta}{2\lambda} - \frac{\mu A l_1}{h_o \lambda} v \cos \beta \quad (4.19)$$

The velocity term in equation 4.19 is to be considered as follows. When the surface temperature is ~400 °C, the droplet's temperature is ~100 °C, and the temperature of the vapour flow is taken as 250 °C (an average of the two). The corresponding vapour viscosity and thickness at this temperature are $\mu \sim 1.82 \times 10^{-5}$ Pa s and $h_o \sim 100$ μm respectively [15, 79], and the ratchet period λ is ~1 mm. Experimentally, the ultimate droplet velocity v is no more than 0.4 m/s.

For a 30 μL droplet with corresponding contact area (A) of ~15.4 mm², the driving force due to the mass term in equation 4.19 is 15 μN, whereas the velocity term is only 0.8 μN. Similarly, for a larger droplet of 580 μL volume ($A \sim 135.6$ mm²), experimentally the mass-term in equation 4.19 is 270 μN whereas the velocity term is 7.4 μN. Accordingly, the velocity term in

equation 4.19 is negligible, so the equation can be even further simplified to equation 4.20, which is the same scaled expression derived for a rigid solid [42], but importantly, now derived entirely from first principles:

$$F_f = \frac{Mgh_o \cos \beta}{2\lambda} \quad (4.20)$$

To avoid measuring h_o experimentally, a simple mass balance is considered. First, the mass lost from the droplet over time is equal to the heat transfer rate across the vapour film (described by Fourier's law [79]) divided by the specific latent heat (equation 4.21). The mass lost from the droplet is also equal and opposite to the vapour mass flow rate, which is given by equation 4.22 below.

$$\frac{dm_{j,1}}{dt} = -\frac{\kappa \Delta T}{L_L h_o} A_{i,1} \quad (4.21)$$

$$\frac{dm_{j,1}}{dt} = -\rho_v \overline{u_x} w_{i,1} h_o \quad (4.22)$$

Here, κ is the thermal conductivity of the vapour, L_L is the specific latent heat of evaporation, ΔT is the temperature difference between the base of the droplet and the ratchet surface, and $\overline{u_x}$ is defined as the weighted-average flow velocity expressed as:

$$\overline{u_x} = \frac{1}{h_o} \int_0^{h_o} u_x dy \quad (4.23)$$

Combining equation 4.11 with equations 4.21–4.23 gives the thickness of the vapour flow (which assumes that the ' vy/h_o ' term in equation 4.11 is negligible as discussed above):

$$h_o = C(T)^{\frac{1}{4}} (\tilde{a})^{\frac{1}{4}} \lambda^{\frac{1}{2}} \quad (4.24a)$$

$$\tilde{a} = \frac{A_i \sin^2 \theta}{m_j \sin^2(\theta + \beta) + \rho_v A_i \lambda \sin \alpha \sin \theta \sin(\theta + \beta)} \quad (4.24b)$$

The $C(T)$ term ($= 12\mu\kappa\Delta T/\rho_v gL_L$) describes the temperature-dependent properties of the vapour flow. The same simplifying assumptions made to equation 4.17 is applied to equation 4.24, leading to:

$$h_o = C(T)^{\frac{1}{4}} \left(\frac{A \sin^2 \theta}{M \sin^2(\theta + \beta)} \right)^{\frac{1}{4}} \lambda^{\frac{1}{2}} \quad (4.25)$$

Substituting equation 4.25 into equation 4.20 gives the driving force:

$$F_f = \frac{Mg}{2} \lambda^{-\frac{1}{2}} C(T)^{\frac{1}{4}} \left(\frac{A}{M} \right)^{\frac{1}{4}} \left(\frac{\sin \theta \cos^2 \beta}{\sin(\theta + \beta)} \right)^{\frac{1}{2}} \quad (4.26)$$

For large droplets with a constant droplet height, the mass can be approximated by $M = \rho_L H_L A$. The corresponding expression for droplet acceleration is simply obtained from $F = Ma$:

$$a = \frac{g}{2} \lambda^{-\frac{1}{2}} C(T)^{\frac{1}{4}} \left(\frac{A}{M} \right)^{\frac{1}{4}} \left(\frac{\sin \theta \cos^2 \beta}{\sin(\theta + \beta)} \right)^{\frac{1}{2}} \quad (4.27)$$

Since the curve AC closely follows the shape of the slope of the ratchet, it is proposed that $\varphi \sim C_1 \varepsilon$ according to similar triangles (triangles AEC and ABF, see figure 4.3), from which a slightly alternative expression for the driving force and acceleration is arrived as shown in equations 4.28 and 4.29:

$$F_f = C_1^{\frac{1}{2}} \frac{Mg}{2} C(T)^{\frac{1}{4}} \left(\frac{A}{M} \right)^{\frac{1}{4}} \left(\frac{1}{\lambda^2 + \varepsilon^2} \right)^{\frac{1}{4}} \quad (4.28)$$

$$a = C_1^{\frac{1}{2}} \frac{g}{2} C(T)^{\frac{1}{4}} \left(\frac{A}{M} \right)^{\frac{1}{4}} \left(\frac{1}{\lambda^2 + \varepsilon^2} \right)^{\frac{1}{4}} \quad (4.29)$$

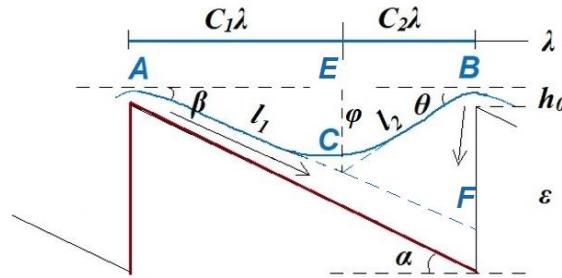


Figure 4.3 – Sketch of the geometry distribution based on deformation analysis

Due to liquid deformation, surface tension acts along the curved liquid-vapour interface and produces a force of $\int \gamma dl$ acting parallel to the interface. Here, γ represents the surface tension and dl refers to a small segment of the length of the curved liquid-vapour interface. The horizontal component of the force generated along arc BC will be balanced by the horizontal component of the surface tension force generated along arc AC. There will also be a net vertical component to this force, which can be defined with respect to either arc AC or

arc BC . For example, the vertical force component of the surface tension acting along the arc BC can be expressed as $\int \sin \theta \gamma dl_2$, where l_2 refers to the length along the liquid-vapour interface between points B and C . Assuming that the surface tension is constant, this integrates to give a vertical force of $\gamma\varphi$ (where $\varphi = \int \sin \theta dl_2$ based on simple trigonometry; see figure 4.3). If assuming that the BC arc is approximately circular, then the effective cross-sectional area of the droplet is $0.5\pi(C_2\lambda)^2$ (i.e. approximately half the area of a circle – πr^2 , where $r = C_2\lambda$). By dividing the vertical force component by this area, the Laplace pressure induced by the surface tension is calculated. This Laplace pressure will then oppose the droplet's hydrostatic pressure ($\rho_L g H_L$) and dynamic pressure ($1/2\rho_L v^2$) according to equation 4.30. From this equation, the values of C_2 and $C_1 (= 1 - C_2)$ can be predicted without the need for any empirical observation.

$$\rho_L g H_L + \frac{\rho_L v^2}{2} = \frac{\gamma\varphi}{0.5\pi(C_2\lambda)^2} \quad (4.30)$$

For example, the droplet velocity is $v \sim 0-0.4$ m/s according to the experiments in this thesis. Thus, for a ratchet with $\lambda \sim 1$ mm and $\varepsilon \sim 0.5$ mm (where $H_L = 5$ mm [15, 65] and $\varphi \sim C_1\varepsilon$ as already mentioned), it is predicted that $C_1 \sim 0.46-0.62$. The deformed proportion then increases to $C_1 \sim 0.59-0.72$ when the ratchet ratio increases to $\lambda : \varepsilon = 1.5 \text{ mm} : 0.5 \text{ mm}$.

Equations 4.28 and 4.29 suggest that the driving force and acceleration are not only dependent on droplet radius/height as the model suggested for a solid Leidenfrost body [42, 79], but also on the ratchet geometry, the surface temperature, and the liquid deformation into the grooves of the ratchets. In practice though, both the driving force and acceleration are insensitive to the droplet height and temperature, because $C(T)^{1/4}$ and $(A/M)^{1/4}$ will remain relatively constant over a large temperature range (100's °C) (which will be described in *Chapter 5*). Therefore, on a ratcheted surface, the driving force should be a function of the droplet radius R alone, with an exponent of ~ 2 (which comes from replacing the first term in equation 4.28 with $M = \rho_L \pi R^2 H_L$, applying to large droplets with a flattened shape). Following this, the model predicts that the acceleration will be similar for droplets with different volumes. The model is also internally consistent. For instance, if the deformed angles, θ and β , are set to 0, then equation 4.26 collapses to the form of equation 4.20, which is the same model derived for rigid non-deformable models (such as a disc of dry ice) [42].

4.1.2 Reynolds Number Justification

The model derived from dynamics study (Section 4.1.1) starts with an assumption of Poiseuille flow, for which the Reynolds number needs to be justified:

$$Re = \frac{\rho_v \bar{u}_x h_o}{\mu} \quad (4.31)$$

The average velocity \bar{u}_x has been defined in equation 4.23. Applying the same analysis done in equation 4.18, the gravity and velocity terms of equation 4.23 can be ignored, yielding equation 4.32:

$$\bar{u}_x = \frac{h_o^2}{12\mu} \cdot \frac{m_j g}{A_i \lambda} \cdot \frac{\cos \beta}{C_1} \quad (4.32)$$

According to Linke *et al.* [24], the deformation proportion of C_1 is no less than 0.5, in line with the experimental observations in this work (see Section 5.1.4 in *Chapter 5*). Herein, the average velocity has the maximum value given when $\beta = 0$ and $C_1 = 0.5$:

$$\bar{u}_x \leq \frac{h_o^2}{6\mu} \cdot \frac{m_j g}{A_i \lambda} \quad (4.33)$$

Applying $m_j = \rho_L A_i H_L$ for large droplets flattened by gravity, equation 4.34 is further simplified:

$$\bar{u}_x \leq \frac{h_o^2}{6\mu} \cdot \frac{\rho_L H_L g}{\lambda} \quad (4.34)$$

Substituting equation 4.34 into 4.31 then gives an expression for the maximum Reynolds number:

$$Re \leq \frac{\rho_v \rho_L H_L g h_o^3}{6\mu^2 \lambda} \quad (4.35)$$

For a rough estimate of the Reynolds number, the physical properties of the vapour flow at the relevant experiment temperatures can be used. For instance, for a surface temperature of ~ 300 °C, the vapour film will be at ~ 200 °C (an average of the solid and the liquid). The physical properties are consequently: $\rho_L \sim 1000$ kg/m³, $\rho_v \sim 0.46$ kg/m³ and $\mu_v \sim 1.6 \times 10^{-5}$ Pa.s respectively. The length scales in this research imply $\lambda \sim 1$ mm, $h_o \sim 100$ μ m [15, 79] and $H_L \sim 5$ mm [15], giving $Re \leq 15$ according to equation 4.35 which confirms a strong laminar

characteristic for the directed vapour flow. If the solid surface instead has a temperature of ~ 400 °C, the vapour film density will be $\rho_v \sim 0.42$ kg/m³ and the viscosity will be $\mu_v \sim 1.82 \times 10^{-5}$ Pa.s, yielding a Reynolds number as low as $Re \leq 10.6$. Therefore, the Reynolds number calculation suggests a laminar vapour flow over the range of several hundred °C, justifying the Poiseuille flow assumption.

4.1.3 Model Validation using Literature Data

A simple validation of the driving force model can be performed by using data already published in the literature [79]. The model in equation 4.28 predicts that the driving force should be proportional to the droplet radius to the power of 2. Figure 4.4 confirms that the gradient of the droplet radius vs measured force data is 1.78 ± 0.24 , which matches the prediction within experimental error.

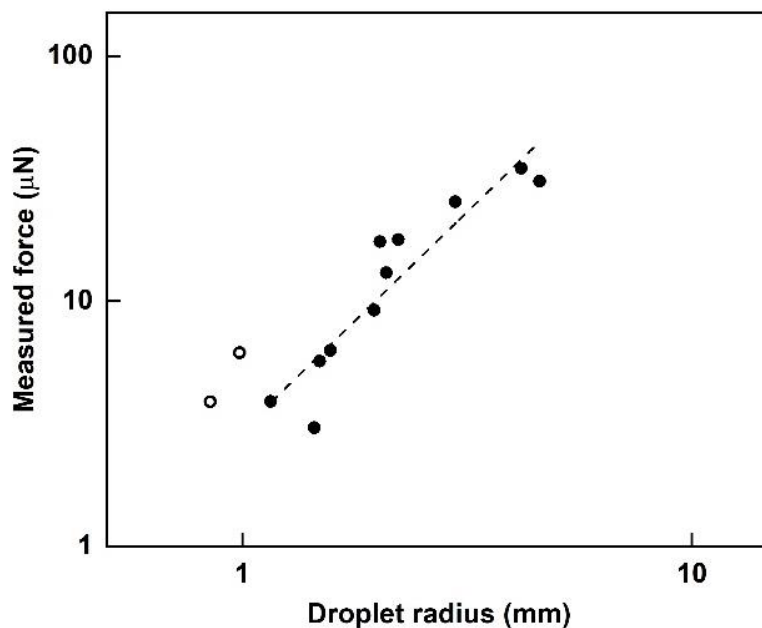


Figure 4.4 – Measured driving force from literature [79]

4.2 Terminal Velocity Prediction

Extension of the new driving force model (equation 4.28) will help derive a model for the terminal velocity when it is combined with a suitable friction model from the literature [100]. As discussed in the literature review, the self-propelling droplet experiences most of its friction from the ratchet cavities. Specifically, the friction results from the loss of kinetic energy when the deformed droplet collides with the steps and the potential energy barriers from

these ratchets. The deformation theory further quantifies the volume of the deformed liquid scaling as $A\varphi$, indicating a loss of kinetic energy of $\sim\rho_L A\varphi v^2$ when the droplet travels a distance of λ , together with an energy loss of $\sim\rho_L g A\varphi^2$ due to the potential barriers. Therefore, the friction force is approximately evaluated according to equation 4.36a:

$$F_b = d_1\rho_L A v^2 \frac{\varphi}{\lambda} + d_2\rho_L g A \frac{\varphi^2}{\lambda} \quad (4.36a)$$

$$F_b = d_1\rho_L A v^2 \frac{\varphi}{\lambda} \quad (4.36b)$$

Here, d_1 & d_2 are numerical coefficients that have the same order of magnitude according to Dupeux *et al* [100]. The other parameters in equation 4.36a imply that only the first term dominates the friction, given that the droplet has a terminal velocity of 0.1–0.4 m/s.

When the droplet reaches its terminal velocity, the driving force (equation 4.28) should be balanced by the friction (equation 4.36b). Equating these expressions enables a model for the terminal velocity to be derived as shown in equation 4.37, where the geometry relations of $\varphi = C_1\varepsilon$ and $M = \rho_L A H_L$ have been used:

$$v = C_1^{-\frac{1}{4}} \left(\frac{g H_L}{2d_1} \right)^{\frac{1}{2}} \left(\frac{C(T)A}{M} \right)^{\frac{1}{8}} \left(\frac{\lambda}{\varepsilon} \right)^{\frac{1}{2}} \left(\frac{1}{\lambda^2 + \varepsilon^2} \right)^{\frac{1}{8}} \quad (4.37)$$

Equation 4.37 suggests that the terminal velocity is mainly influenced by the ratchet design (C_1 , λ & ε). In particular, the ratchet ratio (λ/ε) takes a dominant role, and should be nearly independent of the surface temperature ($C(T)$) and droplet size (H_L) as already discussed.

4.3 Chapter Summary

A new analytical model that describes the dynamics of the self-propelling droplets has been derived from first principles. This new analytical model identifies four influencing parameters: liquid deformation, surface temperature, droplet size and ratchet geometric parameters. The importance of the liquid deformation and the ratchet parameters is included for the first time, which is the key novelty of this model. The model is validated through a combination of literature data and justified assumptions (*e.g.* Reynolds number scale). In conjunction with the previous friction analysis reported in the literature, a new terminal velocity model is further developed, which provides some instruction for designing an optimized ratchet configuration.

The model predicts that the ratchet ratio in particular plays a dominant role in determining the droplet's terminal velocity.

Chapter 5. Experimental Observations of Leidenfrost Droplets on Ratcheted Rings

In this chapter, the experimental results of the Leidenfrost self-propulsion phenomenon will be summarised and compared with the model developed in *Chapter 4*. The variables considered are droplet volume, surface temperature and ring design/configuration. The chapter starts by first considering the physical shapes of the self-propelling droplets in order to attain a basic understanding of their behaviour. This includes a quantitative description of the droplet height, droplet width and droplet deformation due to the ratchet topology. Then, the dynamics of self-propulsion are considered in the form of terminal velocity and acceleration, which are subsequently used to validate the predictions of the model derived in *Chapter 4*. Finally, a brief discussion of the energy conversion efficiency of this phenomenon is conducted.

5.1 Shapes of Self-Propelling Droplets

5.1.1 Modified Ring

A modified ring holder with an integrated viewing window was manufactured that enabled the droplet deformation at the presence of the ratchets to be imaged with a microscopic lens (Figure 5.1). The window was positioned at a height of $h_w = 23$ mm above the base of the ring, and had a length and width of $l_w = 5$ mm and $w_w = 4$ mm respectively. The distance of the ratchet tips to the window's bottom is $\Delta h = 2$ mm. These dimensions minimised the disturbance to the droplets as they transited across this viewing window.

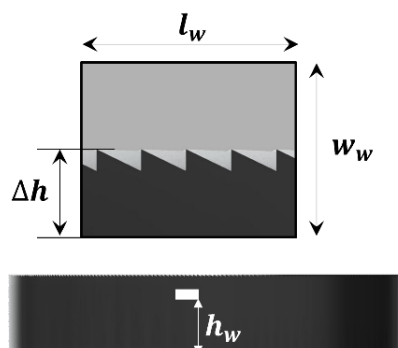


Figure 5.1 – Design of the side-viewing window, allowing for the observation of droplet deformation

5.1.2 Droplet Height

As already described by Quéré [65], a large Leidenfrost droplet on a flat surface will be flattened by gravity. On a ratcheted surface the total energy of a flattened droplet is the sum of the gravitational, kinetic and surface tension effects, as described in equation 5.1a. Here, A' is the side-view contact area and w is the width of the droplet (normal to the direction of motion). The surface energy term includes contributions from both the top-down and side-view interfaces since both are curved in this system. Equation 5.1a can be rewritten as equation 5.1b for a constant droplet volume, where $V = AH_L = A'w$. If the energy is minimised with respect to the droplet height (equation 5.2), the solution predicts a constant droplet height of $H_L = 2\sqrt{\gamma/\rho_L g}$, which is around 5 mm for water [15, 65].

$$E = \rho_L A g \frac{H_L^2}{2} + \frac{1}{2} \rho_L A' w v^2 + 2\gamma(A + A') \quad (5.1a)$$

$$E = \frac{1}{2} \rho_L g H_L V + \frac{1}{2} \rho_L V v^2 + 2\gamma \left(\frac{V}{H_L} + \frac{V}{w} \right) \quad (5.1b)$$

$$\frac{\partial E}{\partial H_L} = \frac{1}{2} \rho_L g V - \frac{2\gamma V}{H_L^2} = 0 \quad (5.2)$$

Experimental measurements of the droplet height are shown in figure 5.2, which were approximated as the ratio of the droplet volume (controlled variable) to the corresponding top-down contact area (measured through image analysis): $H_L = V/A$. Figure 5.2a shows that the height of regularly shaped droplets on ring designs 2, 3 and 4 gradually plateaus as the volume increases, and indeed approaches the value of 5 mm predicted by equation 5.2. Similarly, Figure 5.2b shows that the heights of irregular droplets on ring design 1 also plateau, but appear to be slightly flatter at the same volume. This was because these irregular droplets had a larger top-down contact area due to an enhanced shear force (see 5.1.3 for clarification). Empirical correlations of the droplet height (H_L) were created based on these volume-contact area measurements. These correlations describe the droplet height as a function of droplet volume, which were obtained by a simple regression analysis. The regular droplets are described by equation 5.3 (plotted as line in figure 5.2a, where $R^2 = 83\%$), whilst a separate correlation was defined for the irregular droplets in equation 5.4 (plotted as line in figure 5.2b, where $R^2 = 98\%$).

$$H_L = 0.001 \cdot 1.34(V - 21.9)^{0.161} \quad (5.3)$$

$$H_L = 0.001 \cdot 1.50(V - 25.5)^{0.110} \quad (5.4)$$

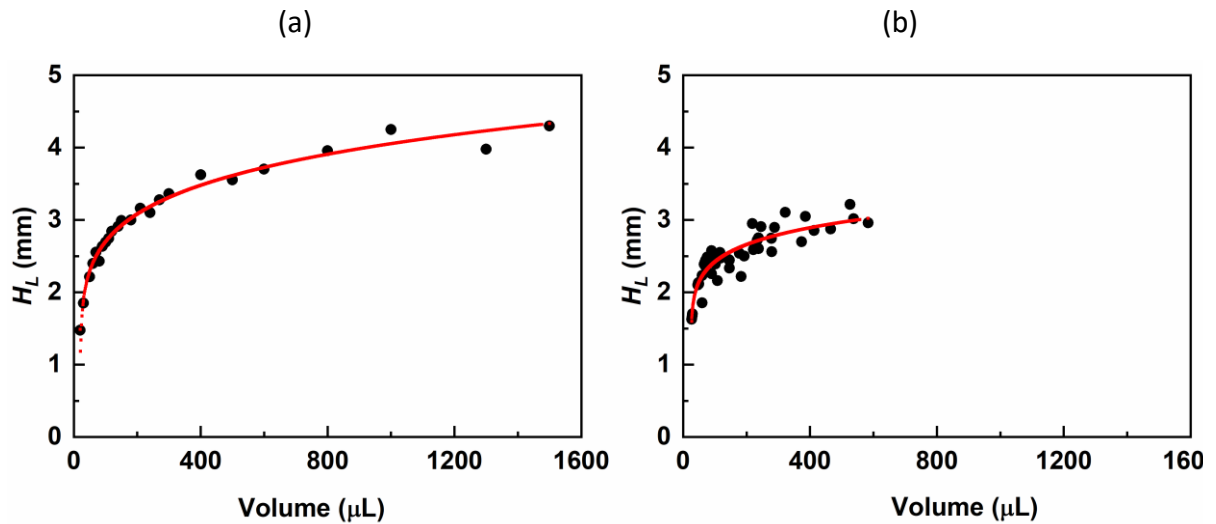


Figure 5.2 – Droplet height plotted as a function of volume. The solid (red) line is fitted by Origin[®]; (a) regularly-shaped droplets on ring designs 2, 3 and 4, (b) irregularly-shape droplets on ring design 1

5.1.3 Droplet Width

Small droplets (defined by volumes smaller than $\sim 300 \mu\text{L}$) were initially observed to be circular after being deposited onto the rings as shown in figure 5.3 a-*i*. Larger droplets however were constrained by the width of the channel ($W = 10 \text{ mm}$), which caused them to become slightly distorted and elongated as shown in figure 5.4 b-*i*. As the droplets accelerated they all tended to spread in the direction of self-propulsion in accordance with the direction of the shear force generated beneath the droplet (see *Chapter 4*). This was then accompanied by a decrease in the droplet width due to a combination of conservation of mass, and an increase of the centripetal force as the velocity increased (see figures 5.3 and 5.4). In particular, on ring design 1 the high driving force caused the droplets to become elongated and flattened during the initial acceleration period resulting in irregular shapes (figures 5.5 (c-*i*)–(c-*iii*)). Here, the top-down contact area was increased resulting in the smaller droplet heights shown in figure 5.2b. The droplet shape then became regular after a short time period under the action of surface tension (figures 5.5 (c-*iv*)–(c-*vi*)).

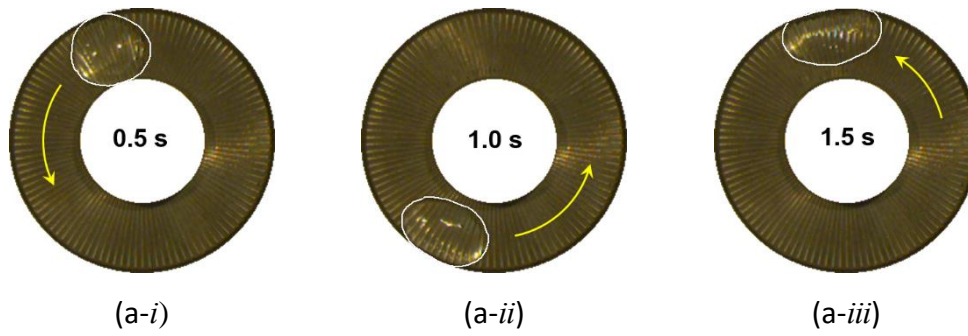


Figure 5.3 – A small $\sim 300 \mu\text{L}$ droplet is observed to be initially circular. Example on ring 4

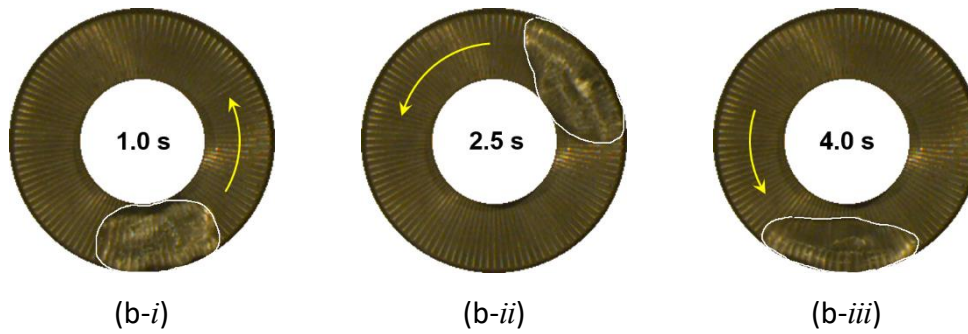


Figure 5.4 – A larger $\sim 600 \mu\text{L}$ droplet is slightly elongated since it fills the entire channel.

Example on ring 4

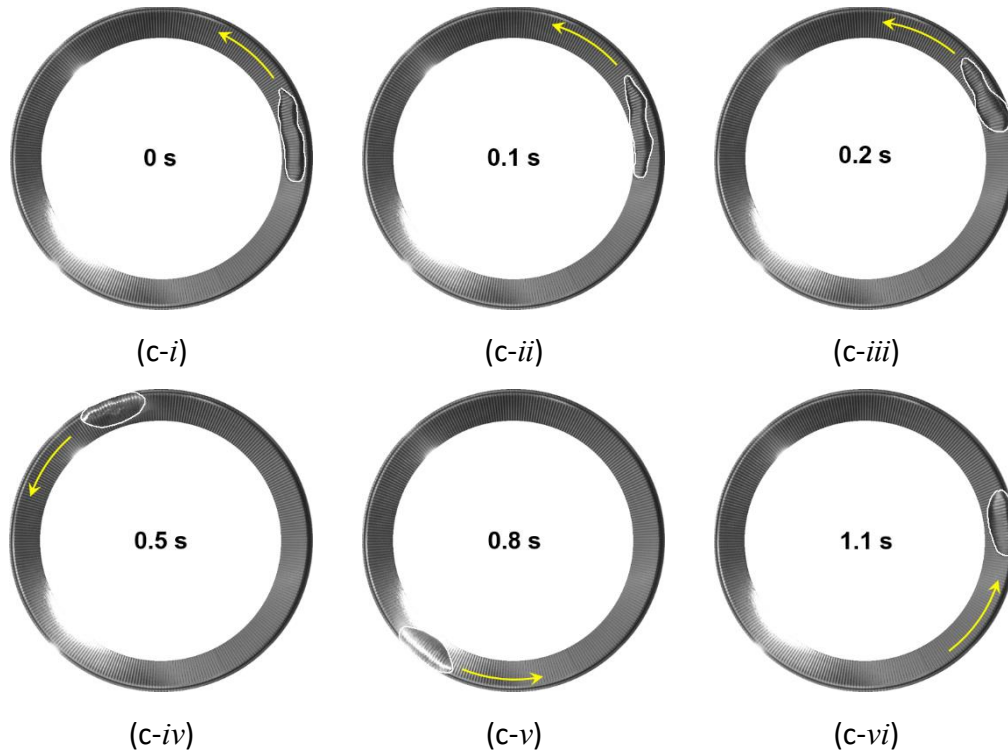


Figure 5.5 – A $\sim 600 \mu\text{L}$ droplet on ring design 1 with an initial irregular shape due to an enhanced shear force, which is then gradually overcome by surface tension restoring it to a more regular size/shape

Experimental measurements of the droplet width were subsequently performed using equation 5.5. Here, R_n is the effective radius of the droplet's circular motion (measured by the custom programme described in Section 3.2), and R_r is the radius of the ring ($R_r = D_o/2$). Figure 5.6 shows an example of the droplet width measured over time; surface tension acts to resist the applied forces to the droplet, resulting in the width plateauing over time.

$$w_{e,n} = 2(R_r - R_n) \quad (5.5)$$

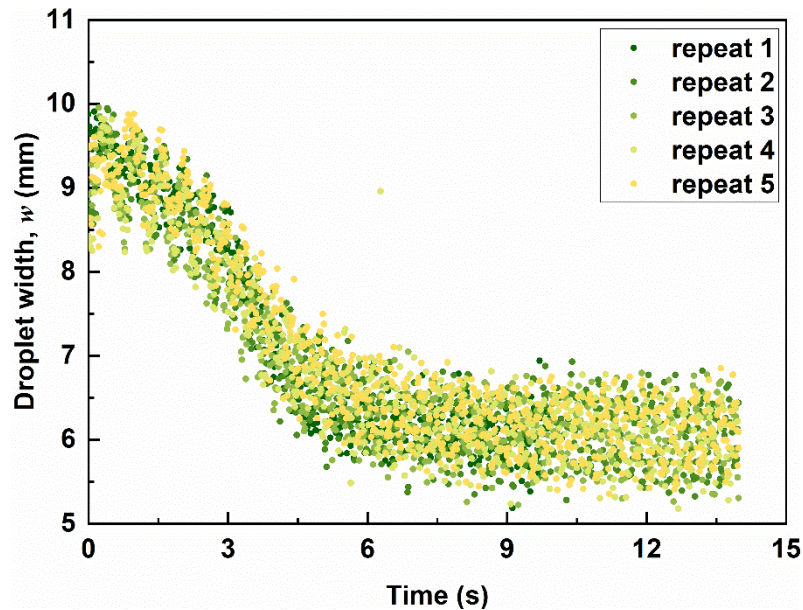


Figure 5.6 – Droplet width measurement. Example for a water droplet with a 1300 μL volume on ring design 4 at a surface temperature of 400 $^{\circ}\text{C}$

An expression for the terminal droplet width can be obtained by minimising the total energy in equation 5.1b with respect to the droplet width (see equation 5.6). Equation 5.8 defines the droplet width as a negative in this system because the flattened direction of the droplet width represents the increase of the radius of the circular motion. Substitution of equations 5.7 and 5.8 into equation 5.6 leads to the solution in equation 5.9 (for more deviation steps, see *Appendix D*). Equation 5.9 implies that the droplet width is expected to plateau.

$$\frac{\partial E}{\partial w} = \rho_L V v \frac{\partial v}{\partial w} - \frac{2\gamma V}{w^2} = 0 \quad (5.6)$$

$$v = \omega R_n \quad (5.7)$$

$$w = 2(R_n - R_r) \quad (5.8)$$

$$w = \sqrt{\frac{2\gamma D_o}{\rho_L v^2}} \quad (5.9)$$

The measured terminal droplet widths on all four ring designs are summarized in figure 5.7, showing no dependence of the droplet volume as predicted by equation 5.9, and the results to be described later in figure 5.11 (terminal velocity became independent of the volume). Equation 5.9 is also plotted in figure 5.7, showing a close agreement with the experimental data. Here, liquid properties at the boiling point were used in the model ($\gamma \sim 59$ mN/m and $\rho_L \sim 960$ kg/m³) [65, 79]. The largest deviation occurred for ring design 1, and it is speculated that the large driving force on ring design 1 accounted for the decreased droplet width measurements from the experiments as already discussed. Note, the model for ring design 3 actually predicted $w \sim 13.7$ mm, which exceeds the annular thickness of the ring ($W = 10$ mm), so this was just plotted at 10 mm.

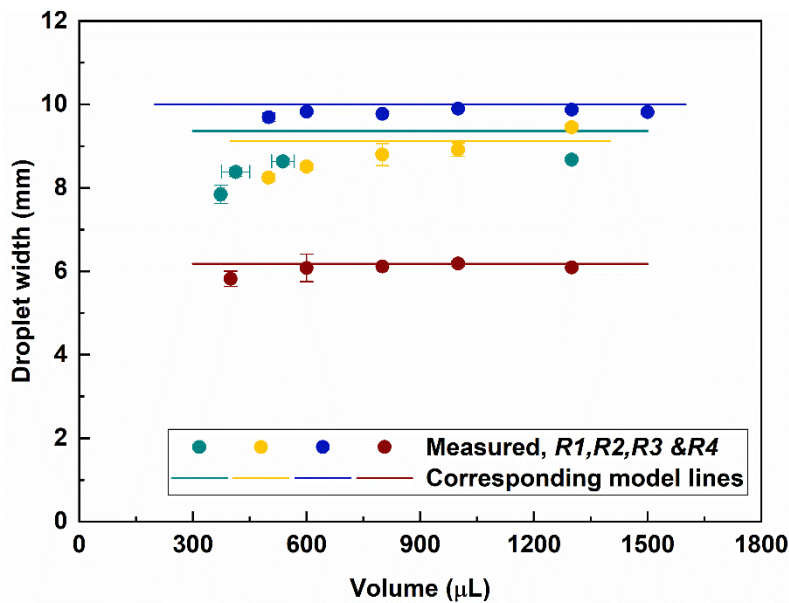


Figure 5.7 – Terminal droplet width prediction using the model in equation 5.9

5.1.4 Droplet Deformation

Under film boiling conditions on a flat surface, a vapour pocket will become trapped beneath the droplet making it unstable [65]. In contrast, the ratcheted texture of the rings enables this vapour to escape laterally within the grooves which improves the stability of the droplets. Droplet deformation at the presence of the ratchet topology is a result of a weight force causing the droplet to follow the topology, and surface tension that acts to restore a spherical shape. These effects are described in equations 4.30.

Figure 5.8 shows the deformation observed using the modified ring mentioned in 5.1.1. Figure 5.8a corresponds to ring design 1 with triangular shaped ratchets, whilst figure 5.8b corresponds to ring design 2 with trapezium shaped ratchets (with $\lambda_{e,o} \sim \varepsilon$). On the triangular ratchets, the period (λ_o) is apparently larger than the ratchet height (ε), and the deformation proportion length was found to be $C_1 \sim 0.67$ (see figure 4.1 for reference). Alternatively, on the trapezium shaped ratchets, it was found that $C_1 \sim 0.5$ where the ratchets were narrow/deep. Using equation 4.30, the deformation length C_1 for the four rings are predicted to be 0.50, 0.46, 0.78 and 0.40 respectively. If the dynamic pressure is included, these then increase to 0.66, 0.63, 0.83 and 0.57 respectively. These predictions are mostly in the range of the experimental observations.

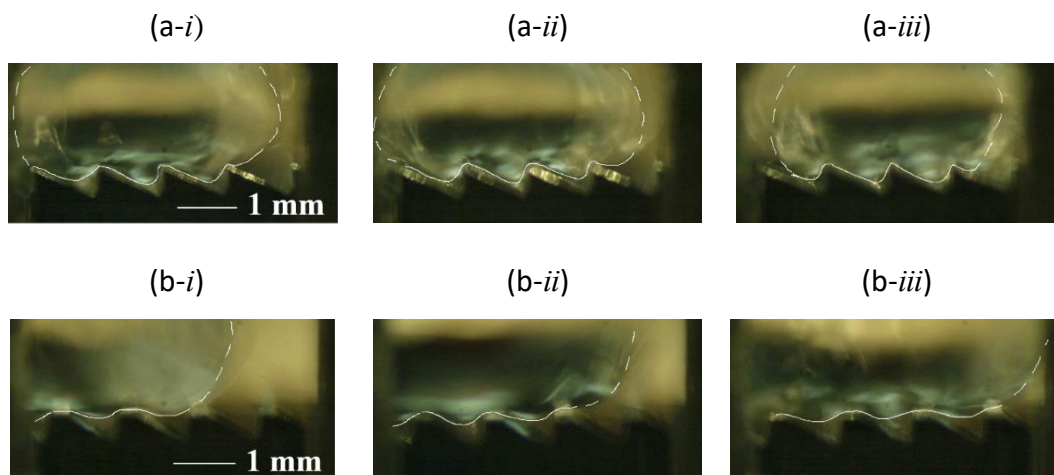


Figure 5.8 – Microscope images showing liquid deformation on ratcheted substrates at various times: (a) $\lambda_o > \varepsilon$, and (b) $\lambda_{e,o} \sim \varepsilon$

5.1.5 Volume Calibration

As described in Section 3.1.2, the self-propulsion phenomenon was studied from the point where the droplet began its positive motion following its injection into the ring. Because the droplets evaporate (slowly) over time, a simple calibration of the volume against the measurable top-down contact area was performed to confirm that the measured acceleration of the droplets was accurate. *I.e.* if the droplet took a long time to decelerate upon injection into the ring, the volume might have decreased enough to influence its acceleration, causing a deviation from the model. A solution to the problem was to simply calibrate the volume by manually measuring the initial contact areas of Leidenfrost droplets at different volumes as shown in figure 5.9. A linear correlation was observed for volumes $> 200 \mu\text{L}$, where the

droplets exhibited a stable height as they were flattened through a combination of gravity and surface tension. This calibration also showed that the droplet height and contact area remained constant across a broad range of different experiment conditions (*e.g.* movement direction, ratchet surface geometry, and operating temperature).

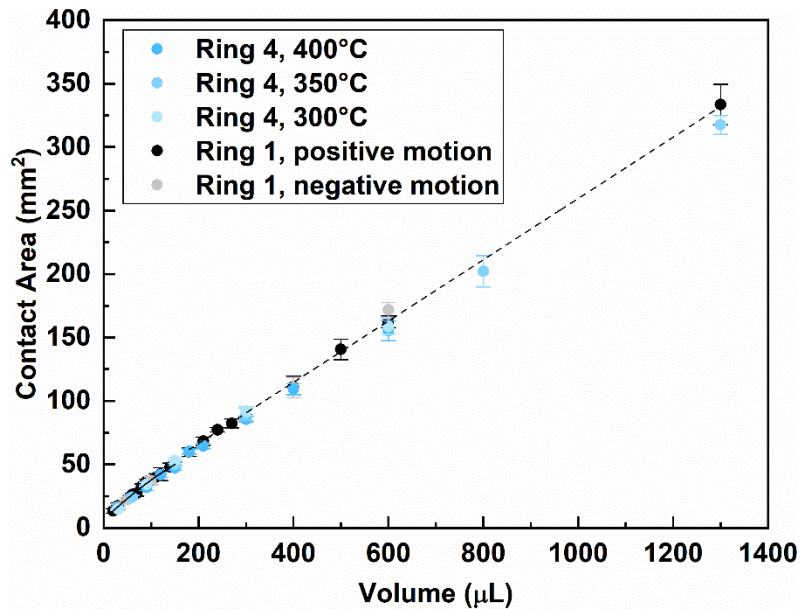


Figure 5.9 – Volume-contact area calibrations. The calibration was repeated on a heated ratcheted surface for different directions of motion, at different surface temperatures and for different diameter rings, showing that the calibration can be used at all conditions required for the self-propulsion study

5.2 Dynamics

5.2.1 Droplet Velocity

Figure 5.8a shows a typical example of the self-propelling velocity obtained from processing the high-speed camera videos using the custom programme described in Section 3.2. The velocity profile follows the typical trend observed in the literature [24]. It is assumed that the friction is zero during the initial period of acceleration, because the loss of kinetic energy is very small at such small velocities [100]. The droplet accelerates until steady state is achieved, where the driving force is matched by friction, resulting in a terminal velocity. The initial slope of this profile therefore corresponds to the acceleration caused by the driving force (a , figure 5.10a). The contact area measurement in figure 5.10b confirms that the droplet evaporation is negligible in the first few seconds.

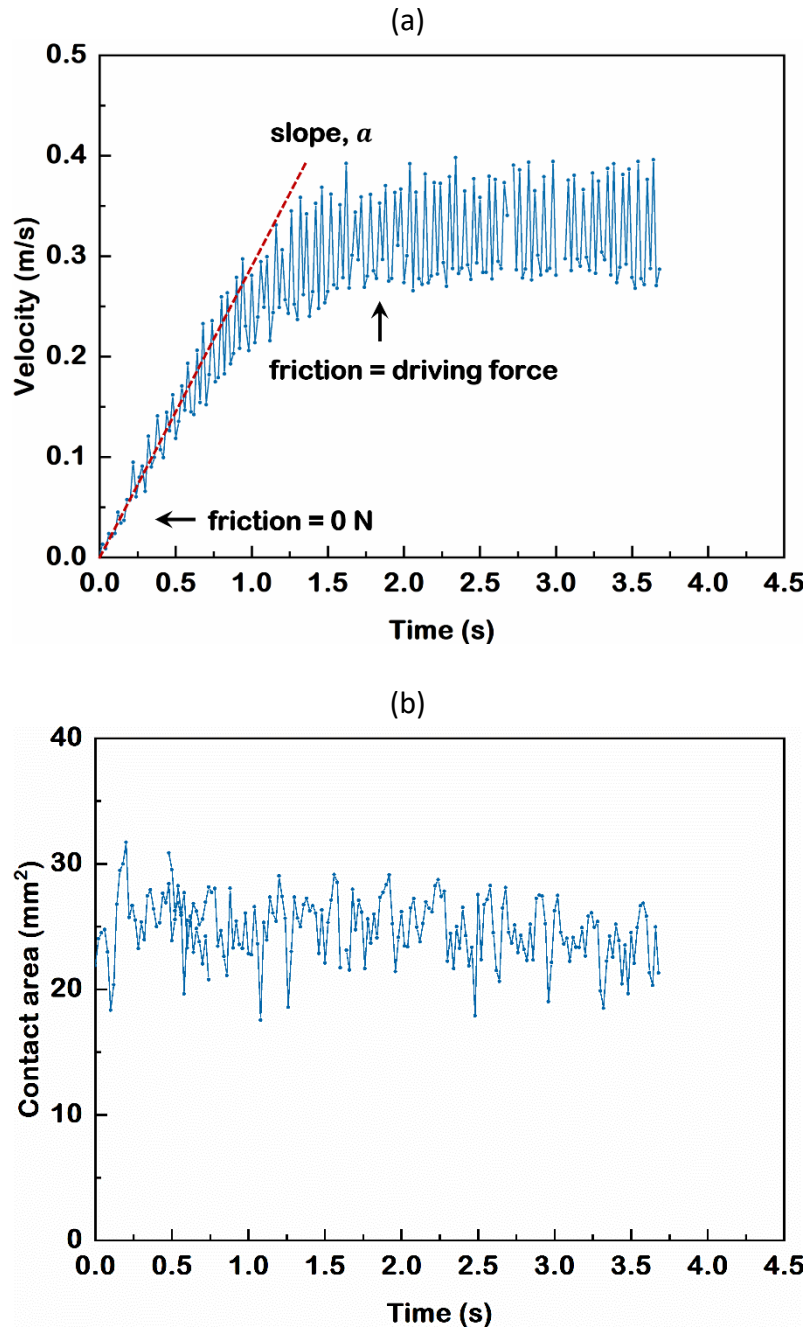


Figure 5.10 – Droplet velocity and top-down contact area measurement. Example corresponds to a water droplet 60 μL volume on ring design 4, at a surface temperature of 400 $^{\circ}\text{C}$

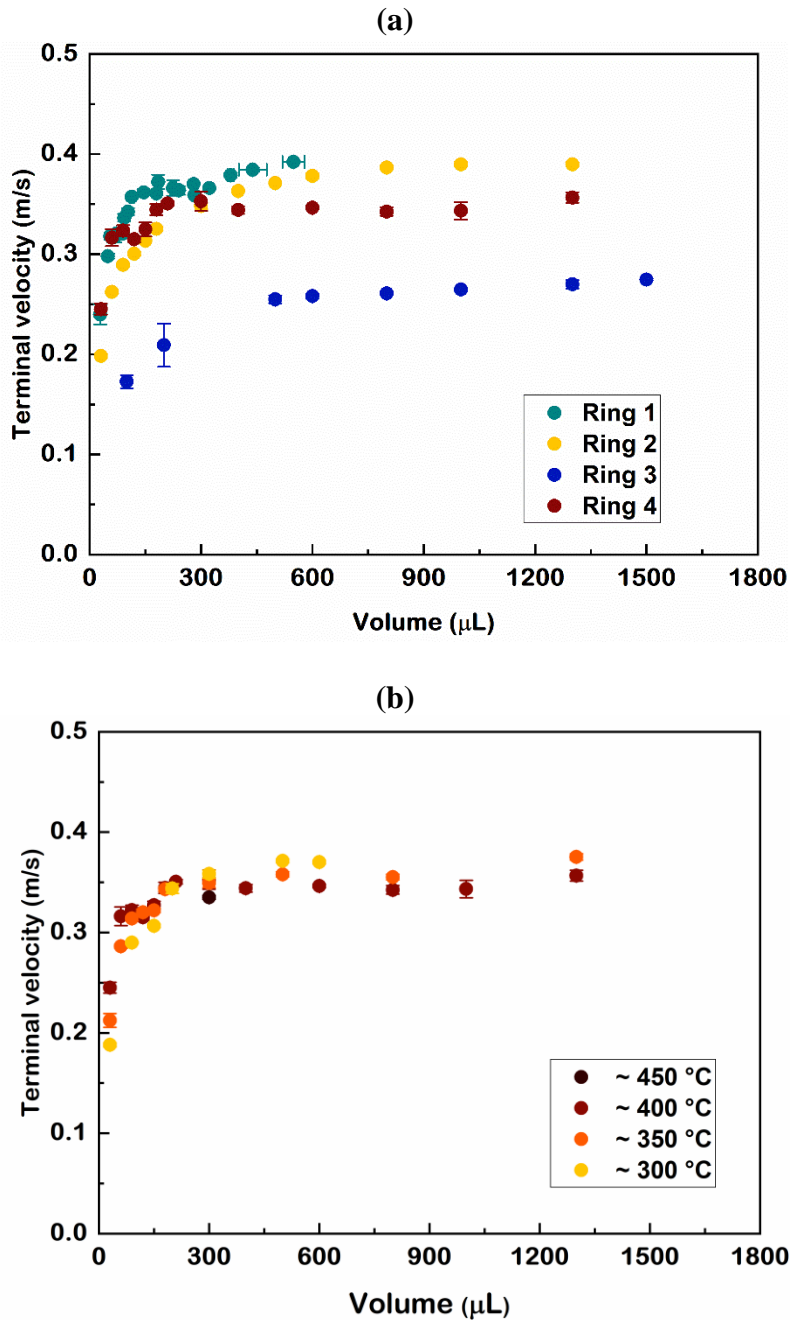


Figure 5.11 – Terminal velocity measurement; (a) data from all four ring designs at a surface temperature of 400 °C, (b) data from ring design 4 at different surface temperatures

Figure 5.11a plots the terminal velocities against the corresponding droplet volumes. Each condition was run at least in triplicate, so each data point represents an average value where the error bars (representing the random error) were taken as the standard deviation. It can be seen that the terminal droplet velocities initially increased as the droplet volume increased, and then plateaued at ~ 0.39 m/s. Previous studies found a maximum velocity of ~ 0.35 m/s for a small droplet (40 μL), whereas the values decreased to 0.18–0.25 m/s when the volume

increased to 600 μL [76, 84, 123]. However, these literature values may not represent the true terminal velocity. According to the experiments presented in this thesis, a total travel distance of ~ 242 mm was necessary for a 50 μL droplet to reach its terminal velocity (~ 0.30 m/s), whilst a displacement of ~ 358 mm was needed for a 385 μL droplet (~ 0.38 m/s). This is much longer than the plates used by Arter *et al.* [123] and Dodd *et al.* [84]. Therefore, one of the advantages of the annular ring design used in this research is droplets over a wider range of volumes are able to be propelled to their terminal velocity, where the effects of the ratchet design parameters (which heavily influence the terminal velocity according to equation 4.37) can then be elucidated. Overall, figure 5.11a and 5.11b indicate that the terminal velocities are dependent on the ratchet design and independent of the surface temperature, in line with the model prediction in equation 4.37.

As the model in equation 4.37 describes, the terminal velocity for a particular ring design is mainly influenced by the droplet height term ($H_L^{0.375}$). According to the droplet height study in Section 5.1.2, large droplets tended to plateau at around 5 mm, which then explains why the terminal velocity also plateaued for large droplet volumes.

To further understand the terminal velocities, the numerical friction coefficient d_1 (from equation 4.36b) is considered. Here, d_1 can be estimated by a simple force balance: $F_f = F_b = Ma$, where a is the measured acceleration, M is the droplet mass, and F_f is shown in equation 4.36b. Table 5.1 summarises the friction coefficients obtained by averaging the results of several large droplets (~ 300 - 1500 μL), where only ring design 1 and 3 with triangular ratchets were considered. The measurement on ring design 1 closely matches the measurement from the literature [100]. Ring designs 3 has a larger deviation, which may be explained by the apparent difference of its ratchet period (see table 3.1).

Table 5.1 – Measured numerical coefficient for droplet’s friction analysis

	Dupeux <i>et al.</i> [100]	Ring 1	Ring 3
$C_1 d_1$	0.029 ± 0.007	0.025 ± 0.003	0.069 ± 0.005

5.2.3 Droplet Motion and Model Validation

Droplet acceleration caused by the shear stress induced driving force was measured by studying the velocity profiles of the droplets over time, as already illustrated in figure 5.8a.

Figures 5.12, 5.13, 5.15 and 5.16 compare the measured acceleration against the model prediction for all four ring designs, which shows a good general agreement. In figures 5.12, 5.13, 5.15 and 5.16, the empirical droplet height models in equations 5.2 and 5.3 were used to replace the $(A/M)^{1/4}$ terms in equation 4.29. Though the deformation distribution was experimentally analysed according to figure 5.8, the model was nevertheless plotted with the predicted values of C_1 to demonstrate the validity of the first-principles analysis. For reference, the model was also plotted with $\beta = 0$ and $\theta = 0$ (equating to a non-deformable body such as a dry ice disc) to further emphasise the role of liquid deformation on the dynamics. In summary, it can indeed be seen that the droplet deformation noticeably impacts the model prediction, clearly demonstrating the novelty of the model work in practice.

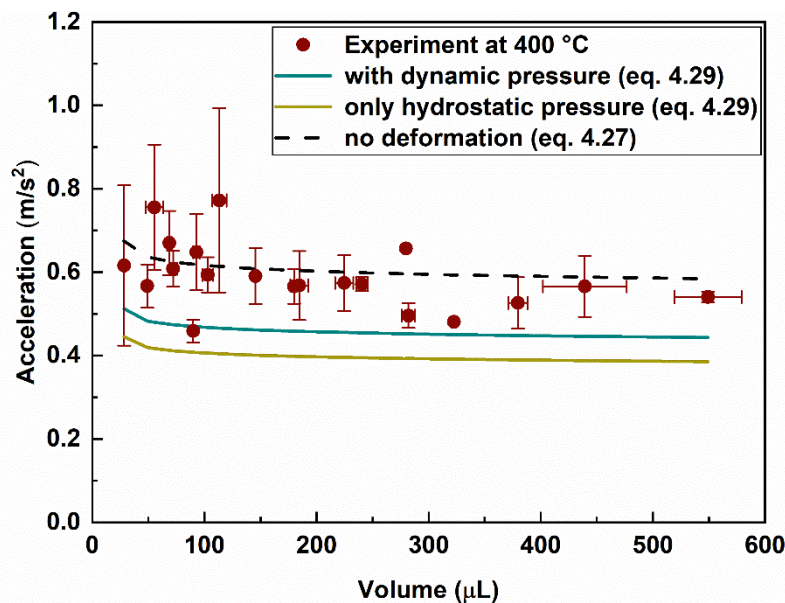


Figure 5.12 – Droplet acceleration on ring design 1. Experiments were run at surface temperature of 400 °C. Horizontal error bars come from the volume calibration. Each line represents a different plot of the model

Individually, the largest deviation between experimental data and model occurred for ring design 1 (figure 5.12), and it is speculated that the elongation effect observed in figure 5.5c might account for this behaviour. *I.e.* the droplets initially spread out in the direction of motion causing them to flatten and increase their contact area, thus increasing the surface energy. The surface tension takes a dominant role in maintaining a stable droplet height since the shear force only acts beneath the droplet. For example, for a droplet with $R \sim 3$ mm, the shear force and surface tension are ~ 25 μN and ~ 354 μN respectively [79]. Surface tension and

gravity are mainly responsible for restoring the ‘normal’ droplet shape [65], especially for small droplets that do not have a constant height.

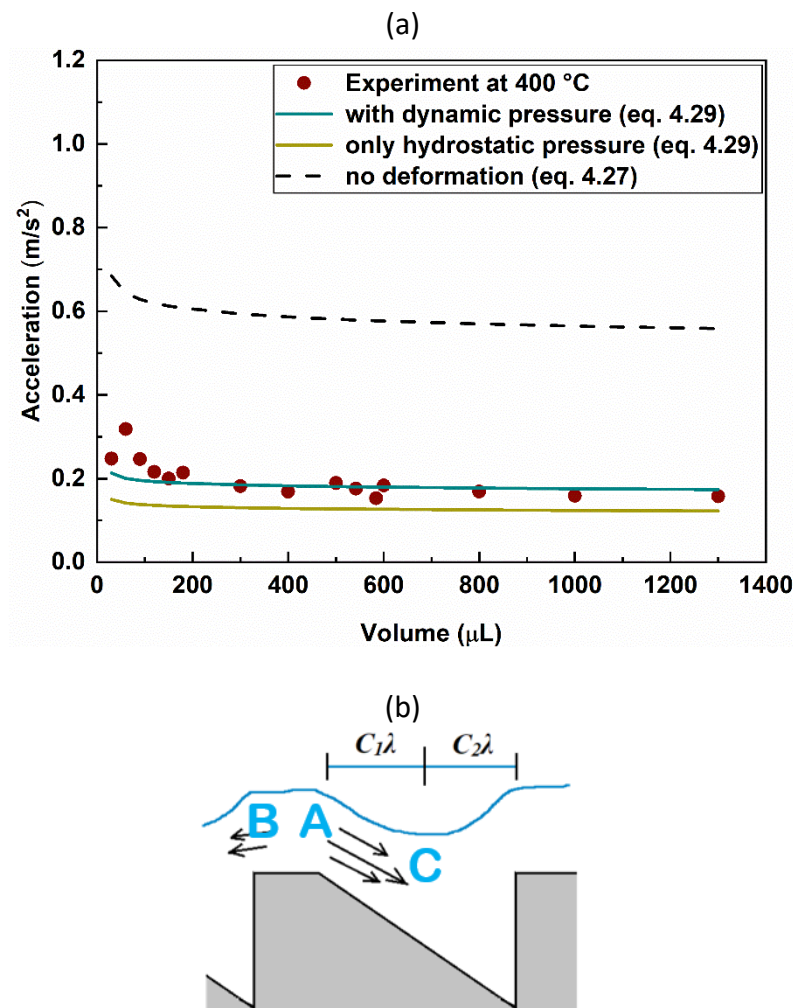


Figure 5.13 – Droplet acceleration on ring design 2; (a) acceleration results at surface temperature of 400 °C. Each line represents a different plot of the model; (b) vapour flow analysis on a trapezoidal ratchet

When the ratchets have a comparable period and height (such that $\lambda_{e,o} \sim \varepsilon$), the driving force and acceleration will become weaker because the droplet deformation becomes more symmetrical (*i.e.* where $C_1 \approx 0.5$), which reduces the AC vapour flow distance, and therefore also reduces the shear force acting on the droplet. This can be seen by comparing figures 5.13a to 5.12. Additionally, trapezoidal ratchet designs further reduce the effective driving force acting on the droplet. Figure 5.13b shows a schematic of the vapour flows. On the flat top of a trapezoidal ratchet, the vapour flows ‘backwards’ from A to B, since the large space at the bottom of the previous slope creates a lower flow resistance compared to the desirable

‘forward’ direction (from B to A) [79]. Therefore, the net driving force is the result of combining the two opposing vapour flows (equation 5.9). For the non-deformable model line, a single forward flow was simply plotted.

$$a = \frac{g}{2} C(T)^{\frac{1}{4}} \left(\frac{A}{M} \right)^{\frac{1}{4}} \left(C_1^{\frac{1}{2}} \frac{\lambda_e}{\lambda} \left(\frac{1}{\lambda_e^2 + \varepsilon^2} \right)^{\frac{1}{4}} - \frac{(\lambda - \lambda_e)^{\frac{1}{2}}}{\lambda} \right) \quad (5.9)$$

When small droplets were deposited on the ring, they tended to settle at the inner edge as they transitioned from the initial negative velocity to a positive velocity. Then, as these started to accelerate in the ‘positive’ direction, centrifugal force caused them to move to the outer edge following the trajectory sketched in figure 5.14a. Thus, it is possible that the driving force continuously changed during this short period because of the changing ratchet parameters (as described above, the ratchets were narrower at the inner edge). In contrast, the larger droplets tended to fill the full annular width of the ring (figure 5.14b), so the average ratchet properties did not change.

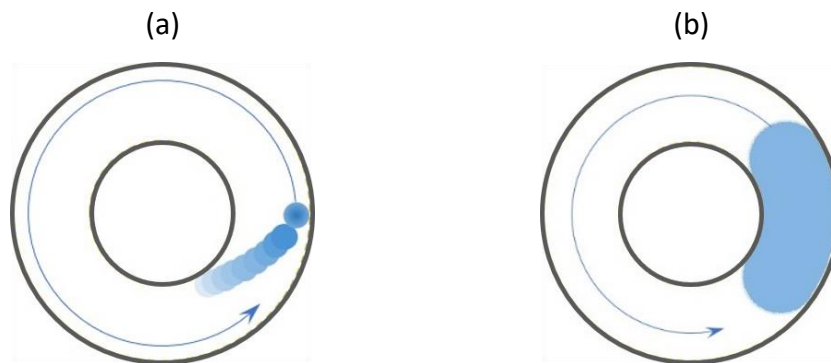


Figure 5.14 – Droplet's trajectory

Figure 5.15 shows the acceleration observed on ring design 4. As just discussed, small droplets changed their trajectories as they accelerated (figure 5.14a). Since ring design 4 transitioned from triangular to trapezoidal ratchets between the inner and outer edges respectively (table 3.1), there was a large deviation between the prediction of the model and experimental results. Therefore, the model was plotted separately with respect to the inner and outer peripheries of the ring. It can be seen that the experimental results reside between these two limits. Further, it can be seen that the larger volumes more closely matched the prediction of the model, since these larger droplets were pinned at the same radius, so did not experience the transition from inner to outer edge dimensions like the smaller droplets. Generally, the

temperature had little effect on the acceleration of the droplets, which matches the limited effect of temperature in the derived model.

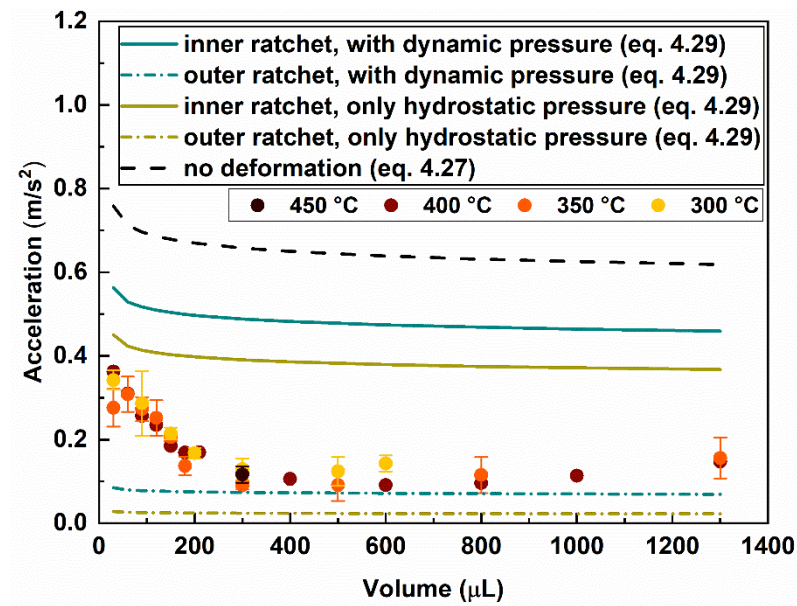


Figure 5.15 – Acceleration on ring design 4 at surface temperatures of 450 °C, 400 °C, 350 °C and 300 °C. Each line represents a different plot of the model

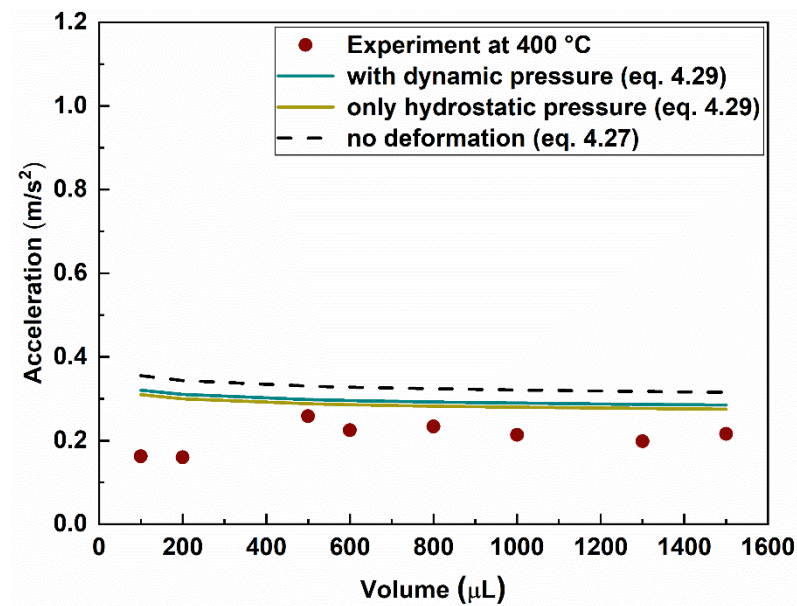


Figure 5.16 – Effect of droplet volume on initial acceleration on ring design 3, at surface temperature of 400 °C. Each line represents a different plot of the model

Figure 5.16 finally shows the acceleration observed on ring design 3. For small droplets, only a small number of ratchets were covered because of the larger ratchet period compared to the other designs. Here the energy loss/friction caused when the small droplets attempted to

overcome the potential energy to self-propel became dominant [100], explaining the deviation at volumes $\leq 200 \mu\text{L}$ as observed in figure 5.16. Generally, the model matched the other volumes more closely.

Generally, the model (equation 4.29) and experimental data reported above show that the acceleration is largely insensitive to the droplet volume. It was difficult to experimentally observe the effects of the ratchet parameters, but the new model can be exploited to predict the effects of ratchet period and ratchet height on acceleration nevertheless. Figures 5.17 and 5.18 plot the effect of ratchet period on acceleration for the triangular-shaped ratchets (including ring design 1 and 3, see table 3.1) and trapezoidal-shaped ratchets (including ring design 2 and 4, see table 3.1) respectively. Note, these are plotted for large droplets ($> 300 \mu\text{L}$) where the droplet height is stabilised.

Figure 5.17 plots the acceleration predicted by the model as a function of the ratchet period for triangular-shaped and trapezoidal-shaped ratchets. As clearly shown, for triangular ratchets, a smaller ratchet period improves the driving force and acceleration. This is because a shorter period increases the steepness of the slope. The experimental result from two different designs follows the model prediction to a reasonable degree, given that the acceleration measurement on ring design 1 was influenced by the initial elongated droplet shape (see figure 5.5c). For trapezoidal ratchets, the model predicts a much smaller effect of the ratchet period, which still agrees with the experimental observations. Here the model was plotted with the same flat top ratio of $(\lambda - \lambda_e)/\lambda = 0.145$ (ring design 2 had a mean value of 0.145 and ring design 4 had an average of 0.13). Applying the design parameters into the model (equation 5.9), equation 5.10 was plotted. The first term in the brackets accounts for the forward driving force and the negative term accounts for the backward driving force (see figure 5.13b). As λ increases, eventually the first term starts to dominate, then the acceleration begins to decrease, which explains the appearance of the maximum in the acceleration for the trapezoidal ratchets. The negative term explains the smaller acceleration values observed on the trapezoidal ratchets.

$$a = \frac{g}{2} C(T)^{\frac{1}{4}} \left(\frac{A}{M} \right)^{\frac{1}{4}} \left(0.855 C_1^{\frac{1}{2}} \left(\frac{1}{(0.855\lambda)^2 + \varepsilon^2} \right)^{\frac{1}{4}} - \frac{\sqrt{0.145}}{\lambda^{\frac{1}{2}}} \right) \quad (5.10)$$

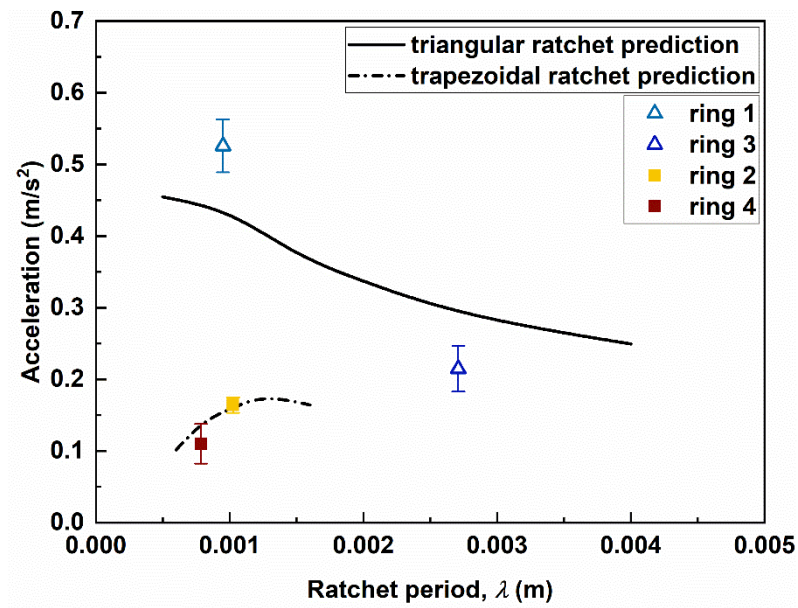


Figure 5.17 – Acceleration as a function of the ratchet period

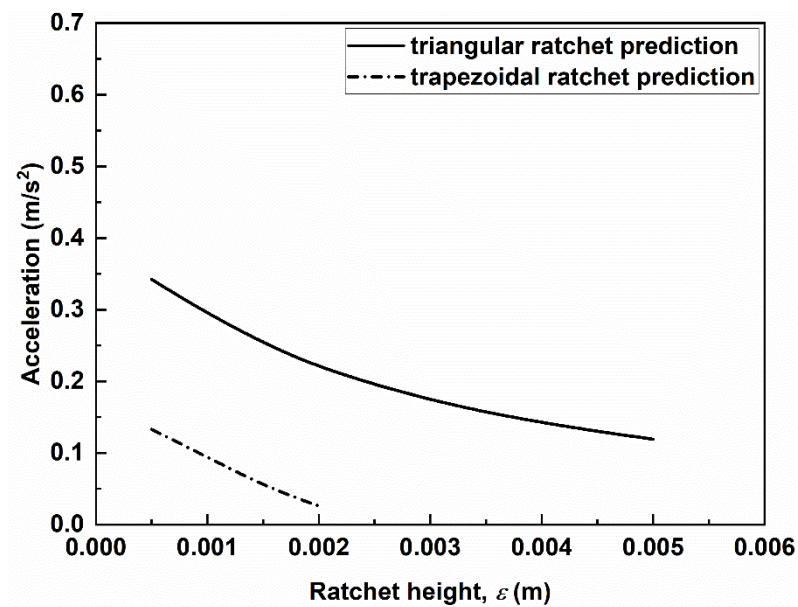


Figure 5.18 – Acceleration as a function of the ratchet height

Figure 5.18 plots the predicted acceleration as a function of the ratchet height, showing a similar decreasing acceleration for both triangular-shaped and trapezoidal-shaped ratchets when the ratchet period was kept the same. This is likely because as the ratchet height decreases the gradient of the slope also decreases, which then reduces the driving force.

5.3 Energy Conversion Efficiency

5.3.1 Latent Heat of the Phase Transition

A large liquid slug with a volume of $V \sim 5000 \mu\text{L}$ is now considered for a simple scaling analysis to characterise the energy conversion efficiency. This volume provides a sufficient lifetime for experimental observations to be made before significant evaporation occurs. The heat transfer between the solid and the liquid is dominated by conduction according to the literature [124], therefore the rate of heat transfer is calculated by equation 5.11a. Here, ΔQ_{in} represents the heat transferred during a time interval Δt . This large droplet volume will be significantly flattened by gravity so will have a constant droplet height H_L (see Section 5.1.2). Applying this then enables the heat transfer rate to be expressed according to equation 5.11b. This means the rate of heat transfer can now be predicted by the measurable top-down contact area (A), since the latent heat (L_L) is known and the height will be $H_L \sim 5 \text{ mm}$.

$$\frac{\Delta Q_{in}}{\Delta t} = L_L \frac{dM}{dt} \quad (5.11a)$$

$$\frac{\Delta Q_{in}}{\Delta t} = L_L \rho_L H_L \frac{dA}{dt} \quad (5.11b)$$

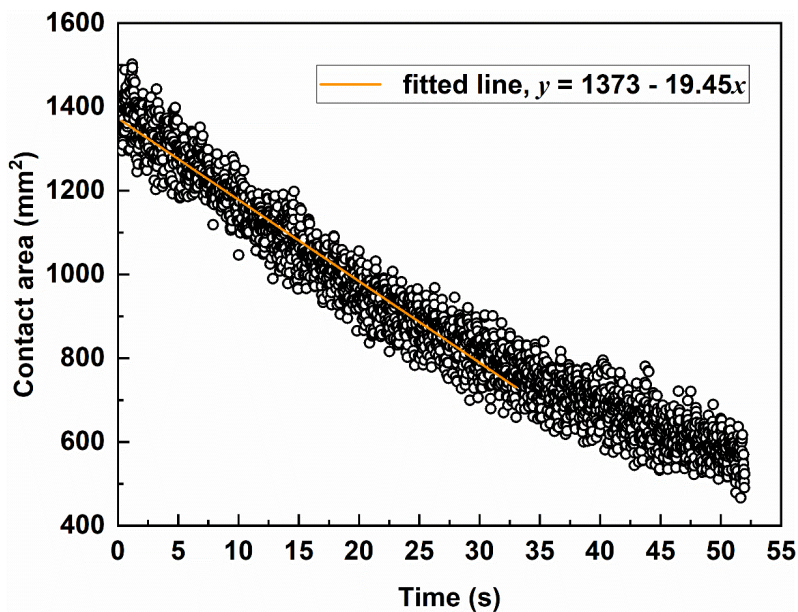


Figure 5.19 – Experimental measurement of the rate of mass declining. Measurement for a large slug ($5000 \mu\text{L}$) on ring design 1, at a surface temperature of $400 \text{ }^\circ\text{C}$

Image analysis was conducted using the custom programme in Section 3.2, producing the tracked top-down contact area (A) shown in figure 5.19. The gradient of the measured top-down contact area against time was determined using linear regression (orange line in figure

5.17), yielding $dA/dt = 19.45 \text{ mm}^2/\text{s}$ in this case. Using $H_L \sim 5 \text{ mm}$ according to equation 5.2 gives a heat transfer rate of $\Delta Q_{in}/\Delta t \sim 222.1 \text{ J/s}$.

The power needed to drive the self-propulsion (P_v) is equal to the driving force multiplied by the velocity, the scale analysis of which is expressed in equation 5.12. Here, the driving force is largely independent of the velocity, as already discussed in the model analysis in *Chapter 4*.

$$P_v \sim F_f v \quad (5.12)$$

According to the velocity and acceleration measurements in figures 5.11a and 5.12, a 5000 μL slug will attain a terminal velocity of $v \sim 0.386 \text{ m/s}$ and achieve an initial acceleration of $a \sim 0.544 \text{ m/s}^2$. Therefore, the driving force determined from $F_f = Ma$ yields a power of $P_v \sim 1.0 \times 10^{-3} \text{ J/s}$.

The energy conversion from the latent heat of the phase transition into the self-propulsion can finally be evaluated using equation 5.13. The efficiency is clearly very low: $\eta_{e,v} \sim 4.5 \times 10^{-6}$. This is mainly due to the excess heat needed for droplet to be in its Leidenfrost state, where there is a high energy cost due to the latent heat/phase change according to Wells *et al.* and Agrawal *et al.* [32, 125]. However, they also suggest that alternative Leidenfrost bodies such as ices of H_2O , CO_2 and CH_4 (*i.e.* solids), in extremely low pressure and high temperature difference conditions, are helpful to reduce the energy cost of levitation, particularly in low gravity environments.

$$\eta_{e,v} \sim \frac{P_v}{\frac{\Delta Q_{in}}{\Delta t}} \quad (5.13)$$

5.3.2 Viscous Dissipation

The energy generated from the shear stress driving force will only be partially converted to kinetic energy (*i.e.* droplet motion); the rest will be lost due to friction (described in Section 4.2) and possibly rotational kinetic energy of the droplet. The energy conversion efficiency in this case can be evaluated by considering the acceleration of the droplet. First, the total energy generated by the driving force can be described by equation 5.14, where s represents the displacement of the droplet during the acceleration process. This can be calculated as an integration of the droplet velocity with respect to time, as described in equation 5.15 (see

Appendix E). Here, an empirical function of the time-dependent droplet velocity was fitted in MATLAB, as shown in figure 5.20.

$$W_f = F_f s \quad (5.14)$$

$$s = \int v dt \quad (5.15)$$

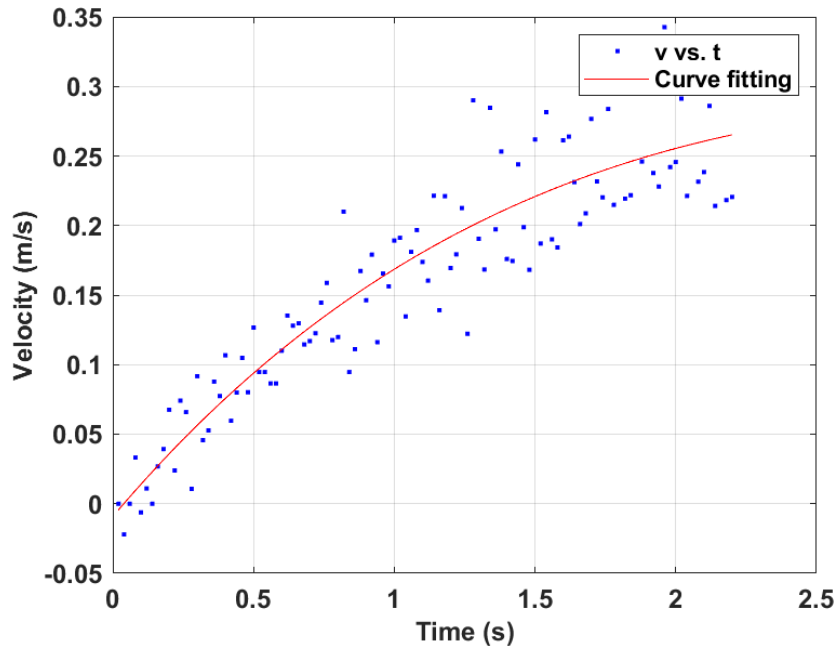


Figure 5.20 – Curve fitting for the droplet velocity against time

The droplet kinetic energy from self-propulsion is simply calculated according to equation 5.16, where the measured terminal velocities (*e.g.* figure 5.9) were applied.

$$E_v = \frac{1}{2} \rho_L V v^2 \quad (5.16)$$

Thus, the energy conversion efficiency from the driving force to the kinetic energy from self-propulsion is evaluated according to equation 5.17. Figure 5.21 summarises the calculations, indicating a maximum energy conversion efficiency of only $\sim 50\%$. The rest of the heat energy will be dissipated by the deformed liquid in the ratchet cavity, and is possibly converted to rotational kinetic energy of the droplet. Both will be beneficial for droplet mixing applications in flow chemistry.

$$\eta_v = \frac{E_v}{W_f} \quad (5.17)$$

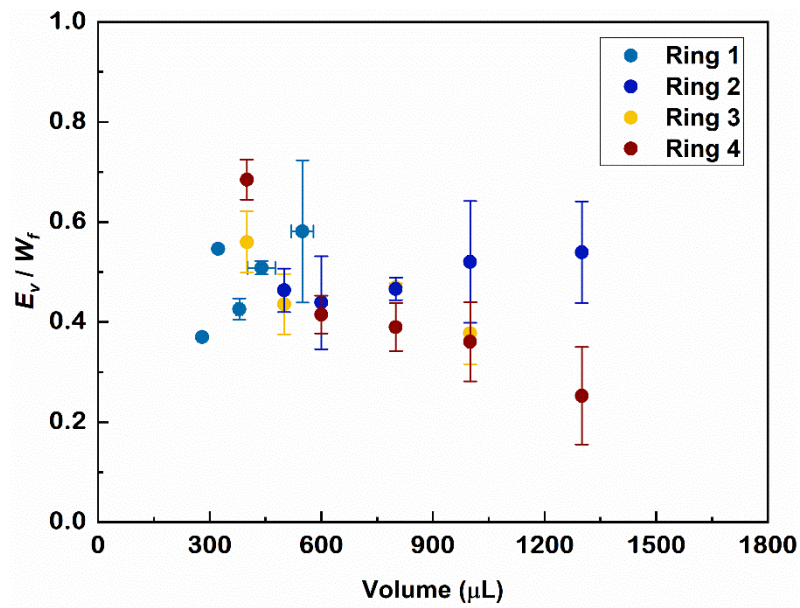


Figure 5.21 – Energy conversion efficiency from the driving force to the droplet kinetic energy from self-propulsion

The frictional energy loss can then be evaluated according to equation 5.18 (see *Appendix E*). Here, the friction model in equation 4.36b and the measured friction coefficient d_1 in table 5.1 were adopted.

$$W_b = \int F_b v dt \quad (5.18)$$

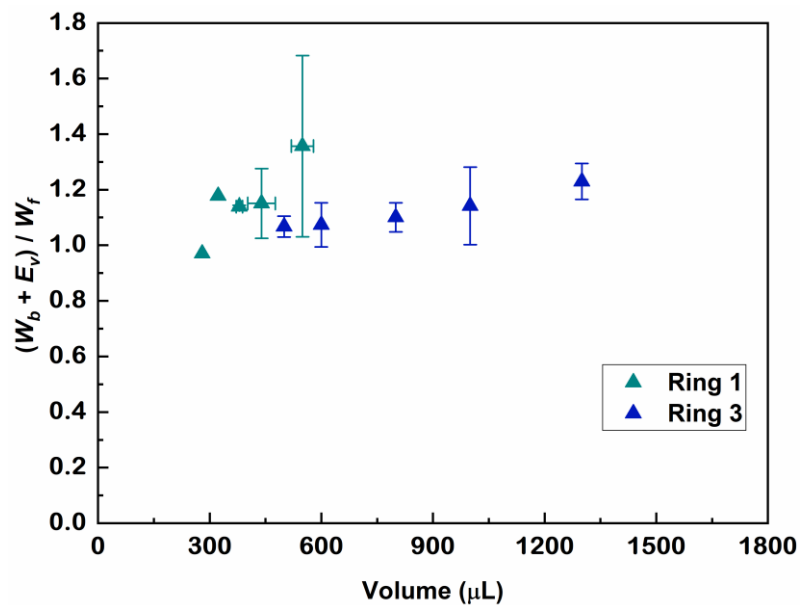


Figure 5.22 – Energy conversion analysis indicates that nearly zero energy is converted to droplet rotation

The sum of the dissipated energy by friction and the gained kinetic energy together account for $\sim 100\%$ of the total energy generated by the driving force, as shown in figure 5.22. Note, data for ring design 1 appears to mostly exceed 100%, though this can be explained by the approximations used in the scaling analysis; for instance, the increased surface energy due to the elongated droplet shapes (see figure 5.5c) was not considered in the estimation of the efficiency. Generally, the result in Figure 5.22 implies that droplet rotation is hardly generated during the self-propulsion process, similar to the large droplet behaviour on a flat surface [22].

5.4 Chapter Summary

Leidenfrost self-propulsion on four different rings have been fundamentally studied. Droplets are observed to self-propel at high terminal velocities (~ 0.4 m/s), which is higher than values previously observed in the literature. Droplets were influenced by gravity (causing them to spread out in all directions) and the centripetal force (causing them to become narrowed). The droplets were also observed to deform around the ratchets, demonstrating the importance of including droplet deformation in the model. Surface tension then acted to balance the effects of gravity, centripetal force, and deformation. The droplet velocity and acceleration measurements showed good agreements with the model predictions, emphasising the role that the ratchet parameters (ratchet period and height) have on the dynamics. The energy conversion efficiency to overcome the latent heat and produce the phase transition was very low ($\sim 10^{-6}$). The energy converted from the shear stress driving force to the droplet's kinetic energy was $\sim 50\%$, with the remainder being used to overcome frictional losses. This simple energy conversion estimation implies that droplet rotation is hardly generated during the self-propulsion phenomenon.

Chapter 6. Droplet Mixing under Leidenfrost State

Mixing in micro channels is typically restricted to pure diffusion due to the laminar flow characteristics; this is a consequence of the low Reynolds numbers that dominate these microfluidic systems. Therefore, the internal flow patterns must be altered in order to enhance mixing. One approach is to modify the physical pattern of the channel to induce turbulent-like features into the internal flows [35]. Alternatively, the flow itself can be modulated, *e.g.* by separating the flow into separate smaller droplets. By rolling the droplets using electrical control of the surface tension [120, 121, 126, 127] or using a winding channel [128], the interfacial area of different fluids will be exponentially increased wherein the diffusion distance will be reduced via the process of engulfment (where exponentially more of the fluid is incorporated into the diffusion environment) [129]. Recirculating internal flows can also be generated in stationary water droplets when they are placed on a hot nonwetting surfaces, leading to an 8–15 fold reduction in mixing time for surface temperatures of 40–60 °C [130, 131].

As discussed in previous chapters and the literature, a Leidenfrost droplet will develop internal convective vortices [22, 132] that stretch and fold the liquid, heavily implying a potential to enhance mixing. When a Leidenfrost drop is placed on a ratcheted surface, it gains further opportunities for mixing enhancement. The Leidenfrost regime by itself induces counter-rotating cells as shown in figure 6.1. Then as the droplet self-propels, it repeatedly collides with the ratchets which induces further internal disturbances [24, 100] that creates continuous and spontaneous fluctuations to the internal flow field. Finally, rotation of the self-propelling droplets provides a further mixing mechanism via the generation of recirculating layers because of the no-slip boundary condition [126].

This chapter aims to study the droplet mixing characteristics under the Leidenfrost and self-propelling Leidenfrost states. The results will demonstrate a significant enhancement over diffusive mixing (a 2 order of magnitude reduction in the mixing time), which establishes this as a potential new device for flow chemistry and mixing applications.

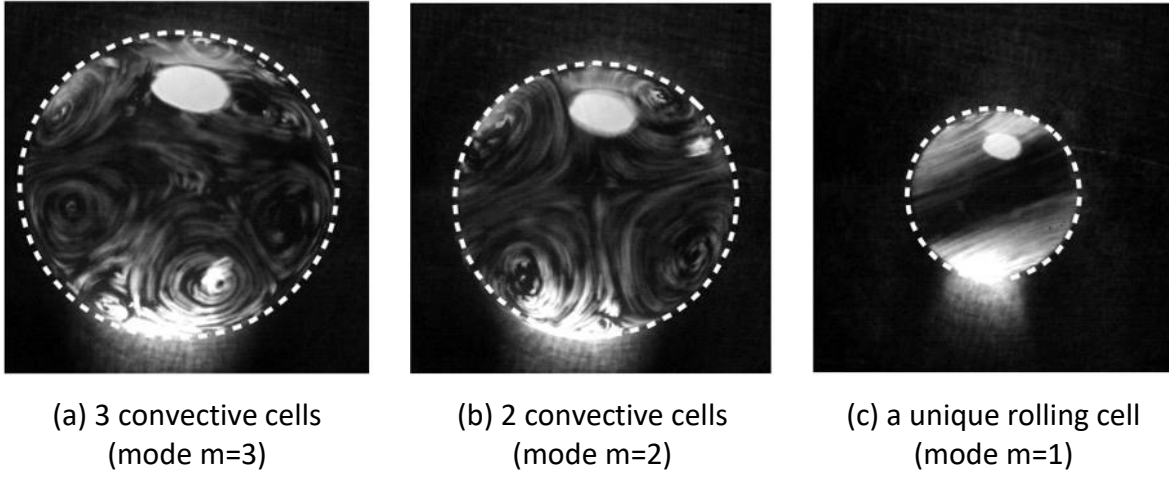


Figure 6.1 – Internal convective cells for Leidenfrost droplets with different radius. Figure taken from Yim et al. [133]

6.1 Assumptions and Preliminary Mixing Analysis

It can be assumed that the internal fluid flows were not impacted by the coloured dyes because a negligible amount was used for each experiment; typically, $\sim 60 \mu\text{L}$ of coloured dye ($\rho_b = 3 \text{ g/L}$) was added to a water droplet of $\sim 400\text{--}1500 \mu\text{L}$ volume ($\rho_L \sim 958.3 \text{ g/L}$).

Next, it is speculated that the convective mixing is dominated by the Leidenfrost regime and repeated collisions between the deformed liquids and the rigid ratchets, which is based on the energy analysis presented in *Chapter 5* (which implied minimal droplet rotation). Given a small amount of deformed liquid, the velocity field of the convective cells from the Leidenfrost regime (on the order of 5 cm/s [22]) is assumed to be independent of the repeated collisions.

In line with this non-rolling assumption, the convective flows are then assumed to be axisymmetric [22]. The convective cell number in each droplet is denoted as m (see the definition in figure 6.1), which is approximately the ratio of the droplet length l and the size of a convective cell r :

$$m = \frac{l}{2r} \quad (6.1)$$

Here, it is assumed that each convective cell has a similar radius r . According to previous experimental studies, the critical radius of a convective cell is $r_c = 1.5 \text{ mm}$. A larger cell tends to break into smaller cells when exceeding the critical size [22, 132, 133].

Once the droplet reaches its terminal velocity, the convective flow pattern is assumed to remain steady. According to Ottino's theory [134], the stretching and folding liquid volumes create more layer interfaces to reduce the diffusion distance, which he defined as the striation thickness Δs . Applying the same theory here (see figure 6.2), the diffusion distance is reduced to $\Delta s = r/\chi_1$, with χ_1 being denoted as the number of the layer interfaces in each convective cell. This leads to a reduced diffusion time in each cell:

$$t_{m,i} = \frac{\Delta s^2}{2D_{diff}} \quad (6.2)$$

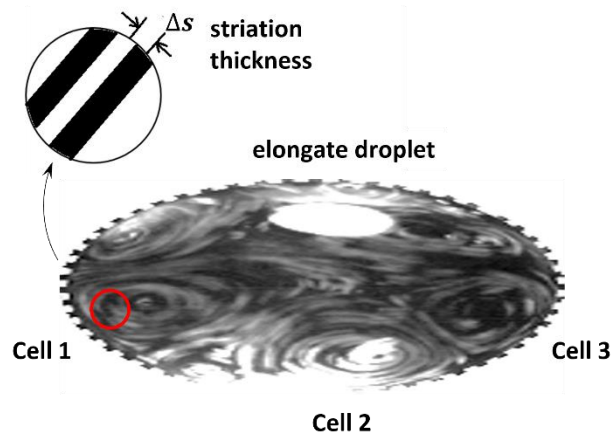


Figure 6.2 – Sketch of the internal convective cells in a self-propelling droplet. The droplet self-propelled along the outer edge of the ring due to a centripetal force, having an elongated shape. Figure reproduced from [133]

Here, D_{diff} is a single particle diffusion coefficient at the liquid's boiling point. The flow within the convective cells in the direction of the droplet's length is assumed to be analogous to an electric current passing through resistors in series. Here the mixing time can be calculated as a sum of the resistances of each cell:

$$t_m = mt_{m,i} + t_D \quad (6.3)$$

where $t_{m,i}$ is the mixing time within each convective cell and t_D is the mixing time between convective cells.

When self-propelling on a ratcheted ring, a large droplet is flattened in both the vertical (by gravity) and radial (by centripetal force) direction as described in *Chapter 5*. Therefore, the

droplet length is approximately the ratio of the droplet top-down contact area and the droplet width: $l = A/(\tilde{c}_1 w) = V/[(\tilde{c}_1 w)(\tilde{c}_2 H_L)]$. Here, \tilde{c}_1 and \tilde{c}_2 are numerical coefficients to account for any deviation caused by the dye. As reported, the evaporation rate of an impure droplet could be prohibited [135], leading to a thinner vapour thickness to influence the self-propulsion dynamics. Applying the droplet width model in equation 5.9 yields:

$$l = \frac{V}{\tilde{c}_1 \tilde{c}_2 H_L} \sqrt{\frac{\rho_L}{2\gamma D_o}} v \quad (6.4)$$

Combining equations 6.1–6.4 then gives the mixing time in terms of the experimental parameters:

$$t_m = \frac{V}{4\tilde{c}_1 \tilde{c}_2 D_{diff} H_L} \sqrt{\frac{\rho_L}{2\gamma D_o}} \frac{r}{\chi_1^2} v + t_D \quad (6.5)$$

Equation 6.5 intuitively implies that the mixing time largely depends on the droplet volume (V), droplet height (H_L), ring scale (D_o) and self-propulsion velocity (v). As seen from figure 5.2, the droplet height (H_L) will gradually plateau as the droplet size increases (critical volumes are $\sim 300\text{--}400 \mu\text{L}$). In this point of view, the mixing time is expected to increase linearly against the droplet volume as the droplet velocity (v) also plateaus (see figure 5.11), in agreement with the result shown in figure 6.6. The result in figure 5.11 shows measurement for large droplet volumes ($>400 \mu\text{L}$). For smaller droplet size, the droplet height begins to reduce (see figure 5.2), implying that the corresponding increasing rate for the mixing time with respect to the droplet volume is lower. This may explain the offset on the x-axis in figure 5.11. When the droplet volume is below $\sim 200 \mu\text{L}$, both the droplet height and velocity will be reduced significantly (see figures 5.2 and 5.11). Droplets smaller than the ratchet period will be stuck, hence no self-propulsion [24, 79]; the mechanism in equation 6.5 is inappropriate whereas the Leidenfrost regime still generates convective swirls to enhance droplet mixing [22, 115].

Mixing between the convective cells may picture two scenarios. If the dye defuses across the droplet width, the diffusion distance is $s_D = (w - 4r)/2$ according to the sketch in figure 6.2. The diffusion time is:

$$t_D = \frac{s_D^2}{2D_{diff}} \quad (6.6)$$

It is also possible to generate some turbulent-like features in the cross section of the droplet owing to the repeated collisions [35]. The diffusion distance then decreases to $s_D = (w - 4r)/(2\chi_2)$, where χ_2 is denoted as the number of the interface layers. The diffusion distance could be exponentially decreased than the initial transverse diffusion distance $(w - 4r)/2$ [35, 128].

6.2 Mixing Time Results

Chapter 3 describes the experimental methodology used for studying droplet mixing; this consisted of the *experimental devices* in Section 3.1.1, *experimental procedures* in Section 3.1.3, and *data analysis* in Section 3.3.

6.2.1 Diffusion at Room Temperature

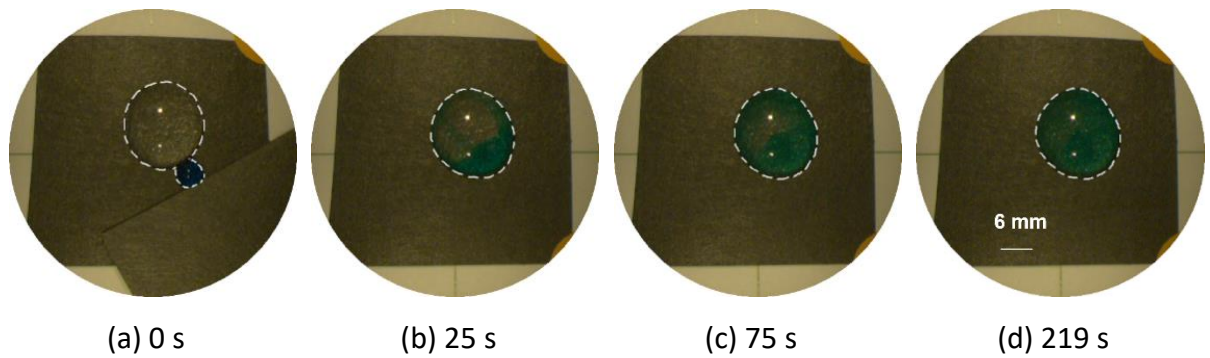


Figure 6.3 – Pure diffusion at room temperature. Example for the dye spread in an $800 \mu\text{L}$ water droplet. The standard deviation of the pixel numbers within the droplet region decreased by 95% at 219 s

Figure 6.3 shows the diffusion process on hydrophobic paper (to mimic the droplet shape produced in the Leidenfrost regime). Figure 6.4 shows the time taken for dye to diffuse in stationary droplets of varying volume. Expectedly, a considerable time (1-10 min) was needed for pure diffusion to take place at room temperature.

The diffusion time, t_{diff} , can be related to the diffusion coefficient at room temperature ($D_{diff,0}$) and diffusion distance (which is on the order of the droplet diameter, or $\sim 2R$; where $2R \gg H_L$) using equation 6.7 [126, 128, 136]:

$$t_{diff} = \frac{(2R)^2}{2D_{diff,0}} \quad (6.7)$$

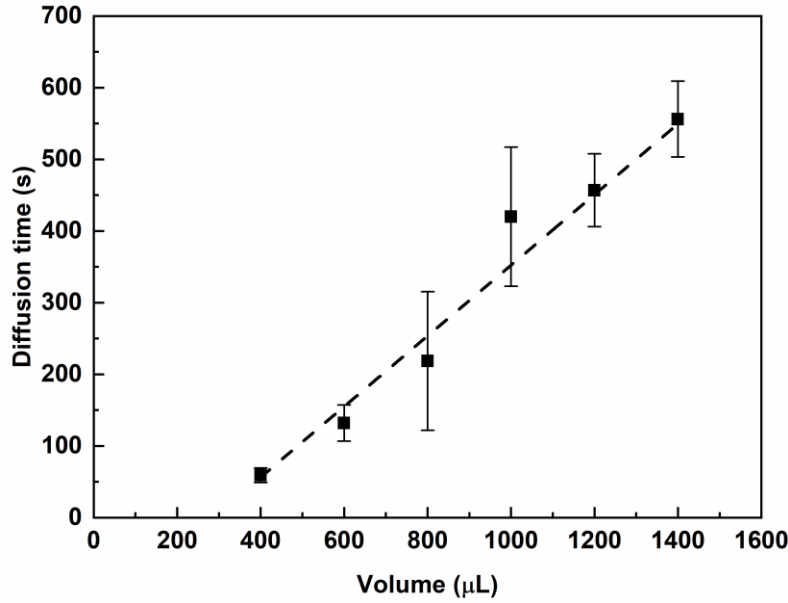


Figure 6.4 – Diffusion time in stationary droplets at room temperature

Since large droplets are flattened by gravity (such that their heights, H_L , remain stable), their droplet volumes will scale linearly with the top-down contact area: $V = \pi R^2 H_L$. Since t_{diff} is also proportional to R^2 , this explains the linear correlation between the diffusion time and the droplet volume in figure 6.4.

Using the data in figure 6.4 and equation 6.7, the diffusion coefficient at room temperature can thus be measured: $D_{diff,0} = 4.1 \times 10^{-7} \text{ m}^2/\text{s}$. Equation 6.8 then calculates the diffusion coefficient for a Leidenfrost droplet [126], yielding $D_{diff} \sim 6.3 \times 10^{-7} \text{ m}^2/\text{s}$. This means increase in mixing due to increase of temperature would be considerable (around 50%) but not dramatic. Here, $T_{L,0} \sim 8\text{-}10 \text{ }^\circ\text{C}$ and $T_L \sim 100 \text{ }^\circ\text{C}$ represent the droplet temperatures at room environment and Leidenfrost state [113] respectively. $\mu_{L,0} \sim 1.34 \text{ mPa}\cdot\text{s}$ and $\mu_L \sim 0.2825 \text{ mPa}\cdot\text{s}$ are the droplet viscosity properties at the two status.

$$\frac{D_{diff,0}}{D_{diff}} = \frac{\mu_L T_{L,0}}{\mu_{L,0} T_L} \quad (6.8)$$

6.2.2 Convection on ratcheted rings

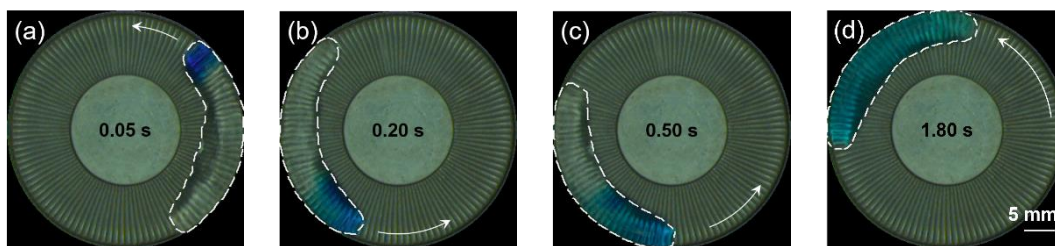


Figure 6.5 – Convective mixing in Leidenfrost self-propelling droplets. Example for the dye collided with an 800 μL DI water droplet on ring design 4 (400 $^{\circ}\text{C}$). The standard deviation within the droplet region decreased by 95% at 1.80 s

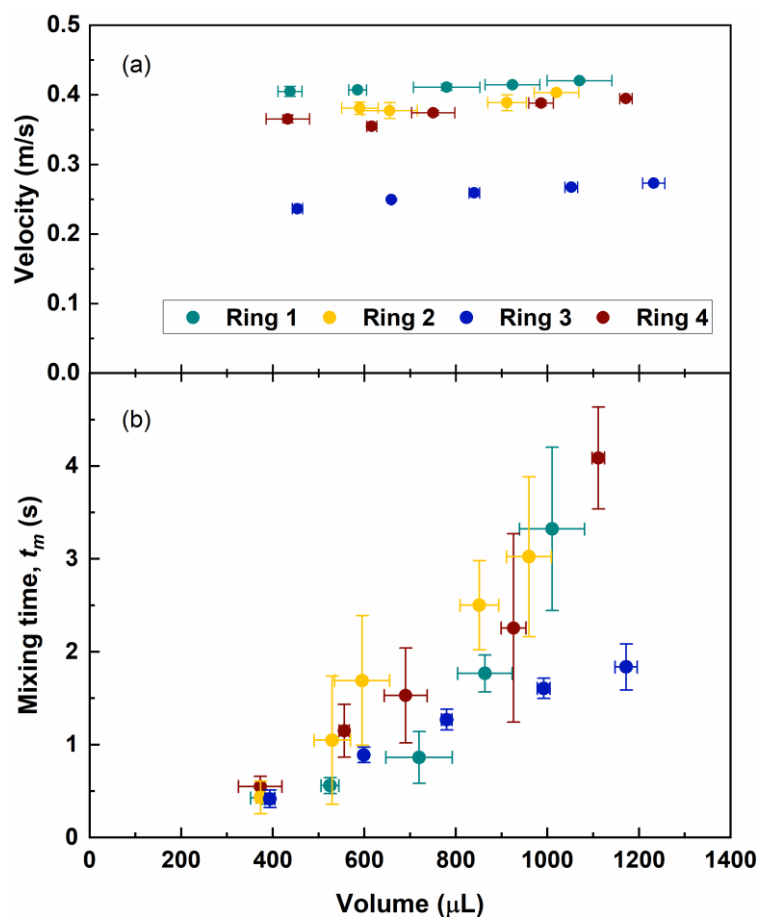


Figure 6.6 – Effect of droplet volume on the mixing time and droplet velocity; surface temperature of 400 $^{\circ}\text{C}$

Figure 6.5 shows the mixing process in a self-propelling droplet on the heated Leidenfrost rings. One can see the dye gradually spread from the collision edge to the receding edge of the droplet, indicating a scenario of non-rolling propulsion. Figure 6.6a and 6.6b show the droplet velocities and mixing times as the droplet volume was varied. Overall, it took less than

5 s at all conditions for complete mixing to be observed on all four ratcheted rings. These mixing times are over 100 times smaller than those observed by pure diffusion at room temperature (see figure 6.4), demonstrating a significant improvement. The temperature effect cannot explain this though effective improvement by taking the temperature into account is still considerable (on the order of 0.5). The mixing time also increases linearly as the droplet volume increased, which agrees with equation 6.5. Note, the large vertical error bars on some of the data points were caused by differences in the initial collision of the large droplet and small droplet containing the dye, which was difficult to control in practice (e.g. different relative velocities and collision positions).

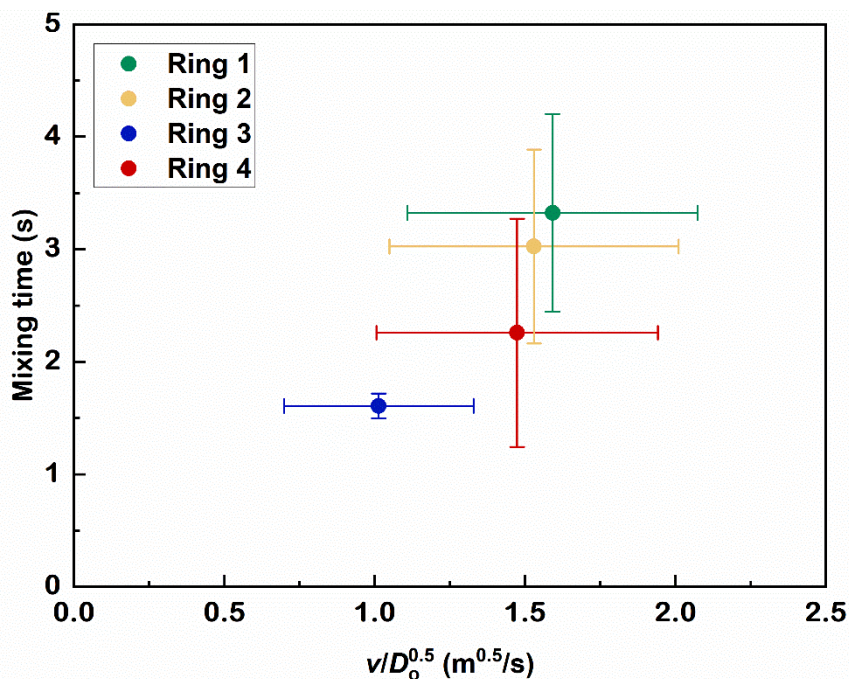


Figure 6.7 – Effect of droplet velocity on the mixing time; surface temperature of 400 °C.

Measurements were taken from similar droplet volumes (986-1070 μL)

Figure 6.7 plots the mixing time as a function of the droplet velocity, which shows a clear increasing trend even though measurements were collected from different devices. This again agrees with the prediction in equation 6.5, where the difference of devices is reflected by the scale of the ring diameter (D_o).

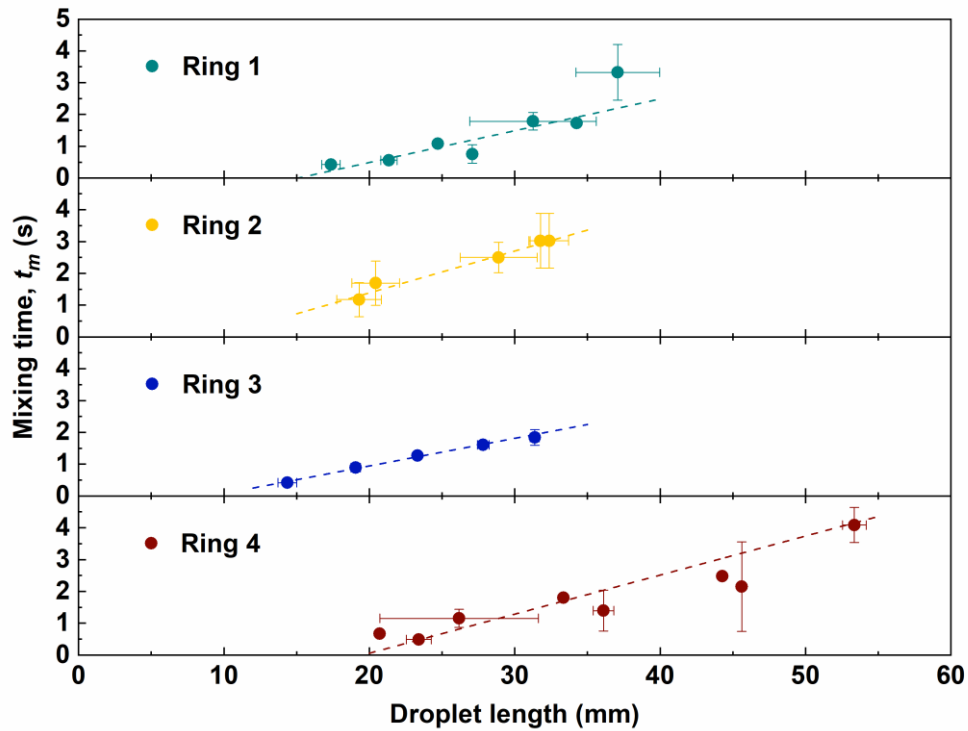


Figure 6.8 – Mixing time as a function of the droplet length

Among the four ring designs, ring design 3 demonstrated the most efficient mixing. Counter-intuitively, ring 3 also produced the smallest droplet velocities as shown in figure 6.6a. However, this is still in agreement with the analysis in equation 6.5: a smaller droplet velocity implies a reduced convection time (t_m). This is reasonable because the droplet centripetal force will be diminished at smaller droplet velocities, leading to a less narrowed droplet width and shorter droplet length. Herein, the dye went through fewer convective cells and the flow time will be reduced. As seen from figure 6.8, the mixing times increase linearly against the droplet length, which also verifies the assumption in equation 6.3 that the convective cells behave as resistors in series. Note, the droplet length is taken as the ratio of the top-down contact area and the droplet width, $l = A/w$.

On ring designs 1 and 2, both the droplet velocities and the mixing time are similar, because both the ring design (see table 3.1) and the droplet velocities (see figure 6.6a) are similar. On ring design 4, the mixing time is comparable to the result on ring designs 1 and 2, though it was designed with a smaller diameter D_o (see table 3.1). This seems to disagree with the analysis in equation 6.5, which suggests that a smaller diameter increases the convection time by raising the centripetal force to further elongate droplet length. However, an increased

centripetal force also implies a narrowed droplet width that helps to reduce the diffusion distance (which is s_D in equation 6.5).

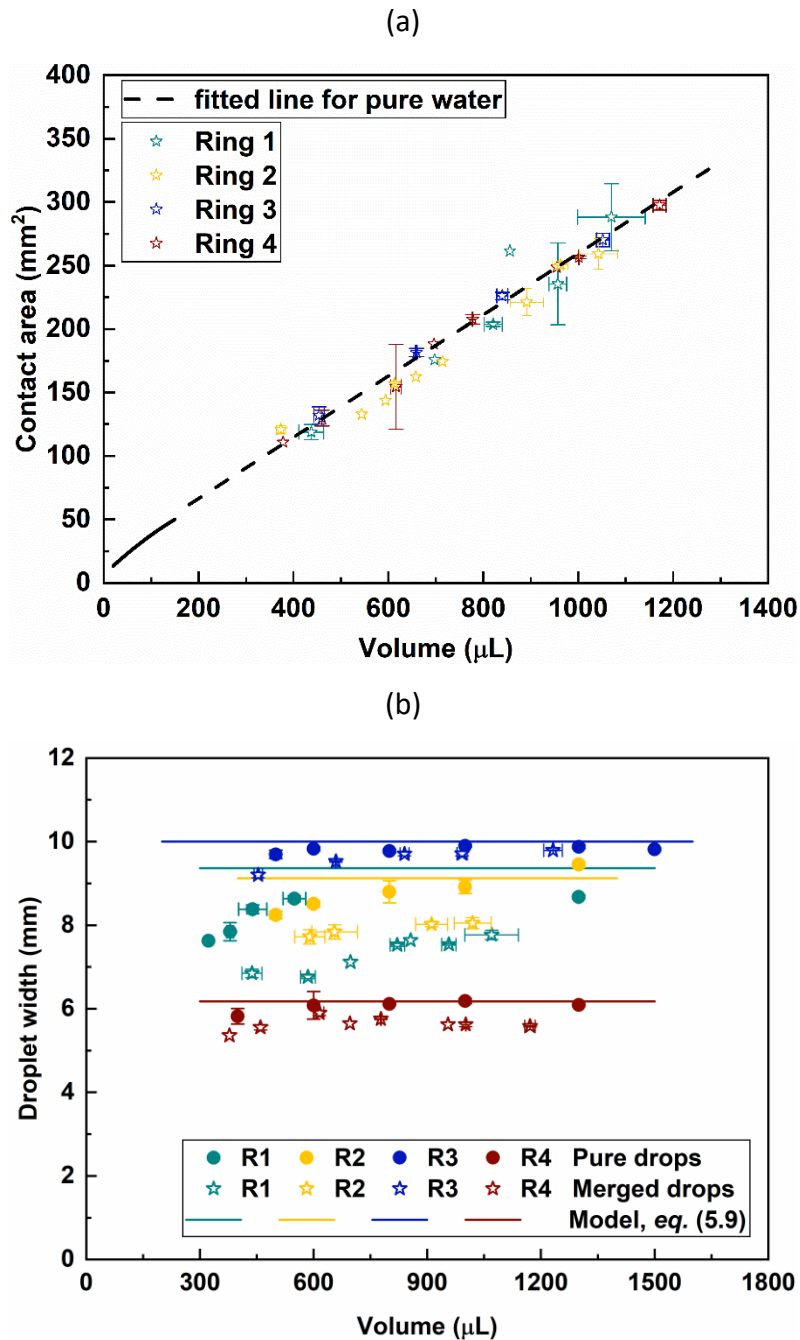


Figure 6.9 – Droplet shape study of the merged droplets; (a) Top-down contact area measurement, (b) Droplet width measurement. Data for pure water droplets is taken from figures 5.5 and 5.7 respectively

Figure 6.9 shows the experimentally measured droplet height and droplet width following the merger of two droplets. The top-down contact area of the combined droplet still followed the benchmark area measurement for pure water droplets (figure 6.9a), implying the droplet

height did not change when dye was added, where $\tilde{c}_2 \sim 1$. However, there is a noticeable deviation of the measured width from pure water droplets (figure 6.9b), suggesting $0 < \tilde{c}_1 < 1$. As speculated, droplet impurity may prohibit the evaporation rate [135] to produce a thinner vapour layer. This may stimulate the self-propulsion by increasing the pressure gradient in the vapour layer, leading to slightly increased droplet velocities than pure droplets, which in turn further narrowed the droplet width in response to the increased centripetal force.

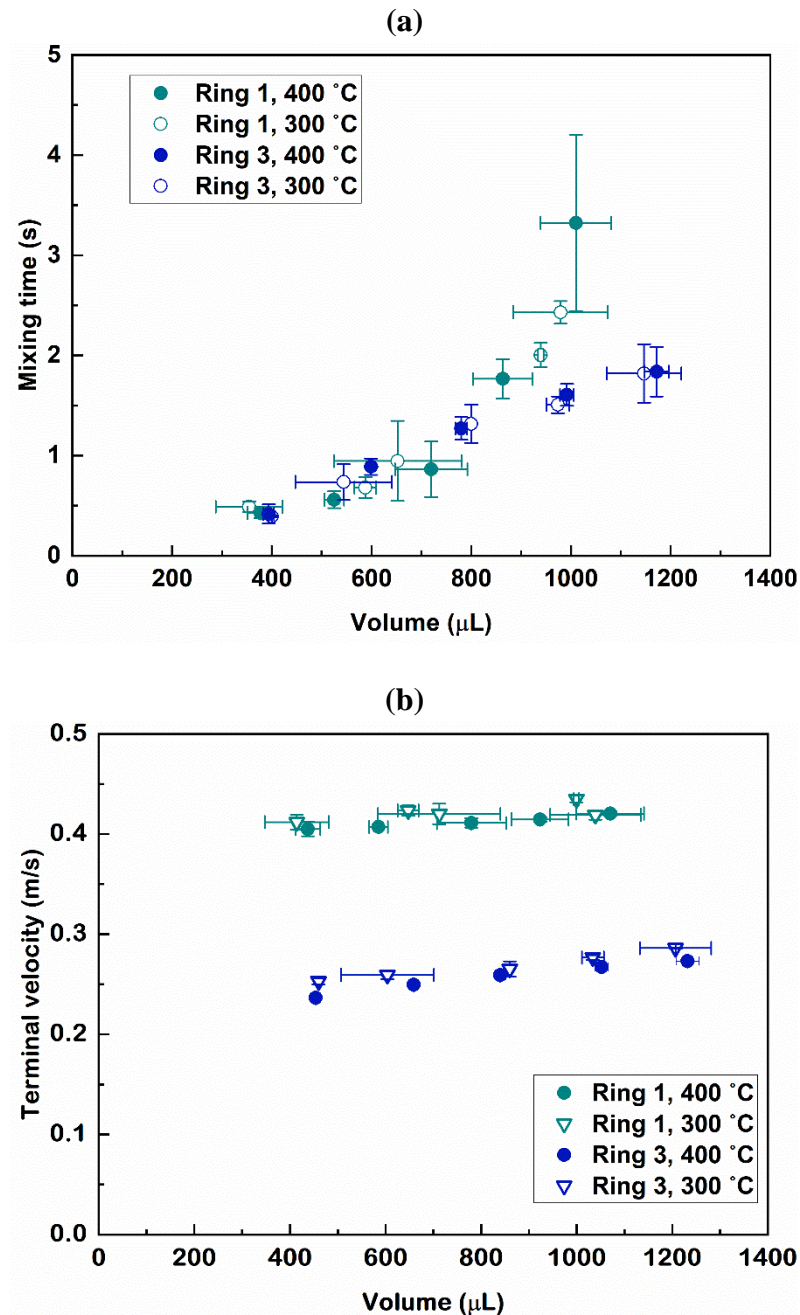


Figure 6.10 – Impact of surface temperatures on (a) mixing time and (b) droplet velocity

In figure 6.10a, the mixing time, and by implication the internal fluid flow patterns, showed little dependence of the surface temperature. This is correlated with the observation that surface temperature has little effect on the droplet velocity as shown in figure 6. 10b. Here the droplet encounters a similar number of collisions with the ratchets regardless of surface temperature.

6.2.3 Convection on a Flat Surface

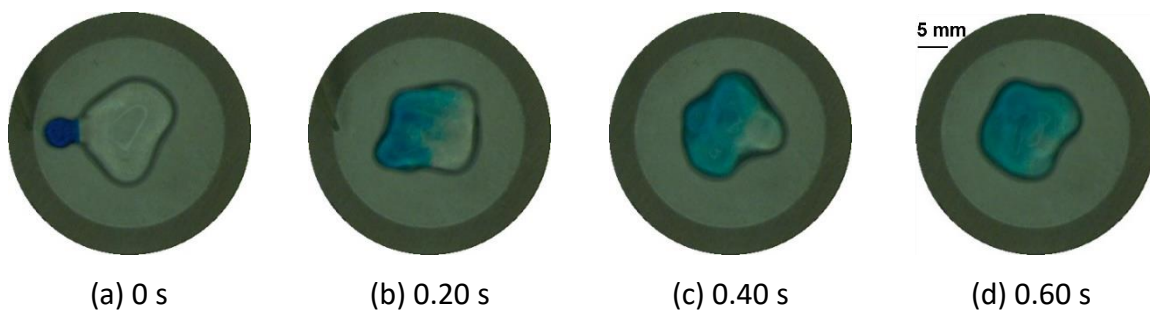


Figure 6.11 – Star-shaped oscillation for Leidenfrost drops on a flat surface. Example for a water droplet of 800 μL at surface temperature of 400 $^{\circ}\text{C}$

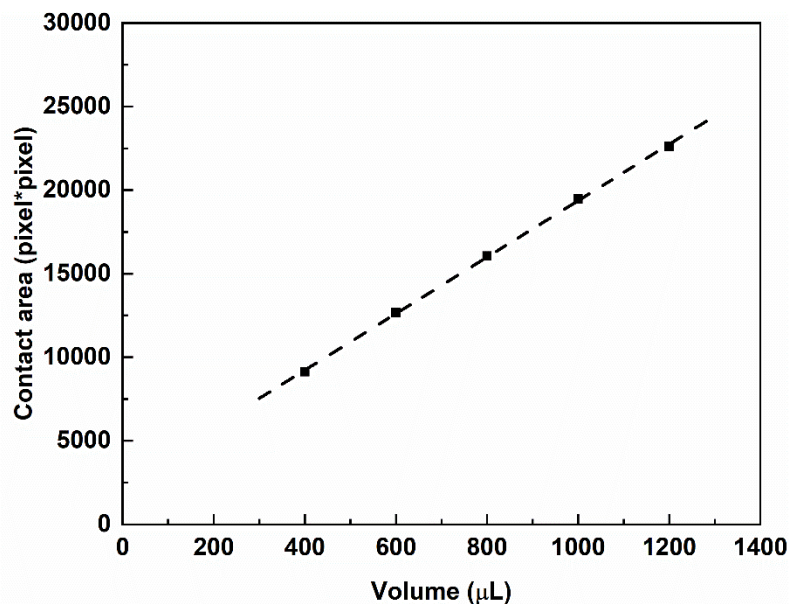


Figure 6.12 – Volume-contact area calibrations for droplets on a flat surface

To further benchmark the performance of the Leidenfrost mixing phenomena, additional experiments were performed on a heated flat surface. This also required an updated volume calibration (in figure 6.12) because a thick vapour pocket forms beneath the droplet to alter the droplet geometry [15, 137].

As seen from figure 6.13 the flat surface produced mixing time directly comparable to the best mixing times observed on the ratcheted Leidenfrost ring result (obtained on design 3). Here, instead of collisions with the ratchets driving the improved mixing, it was droplet oscillations (figure 6.11) that induced more turbulence within the internal fluid flow. Oscillations are commonly observed for Leidenfrost droplets on a flat surfaces, which are often referred to as star-shaped oscillations because the droplet develops distinct lobes [25, 68, 69, 138, 139].

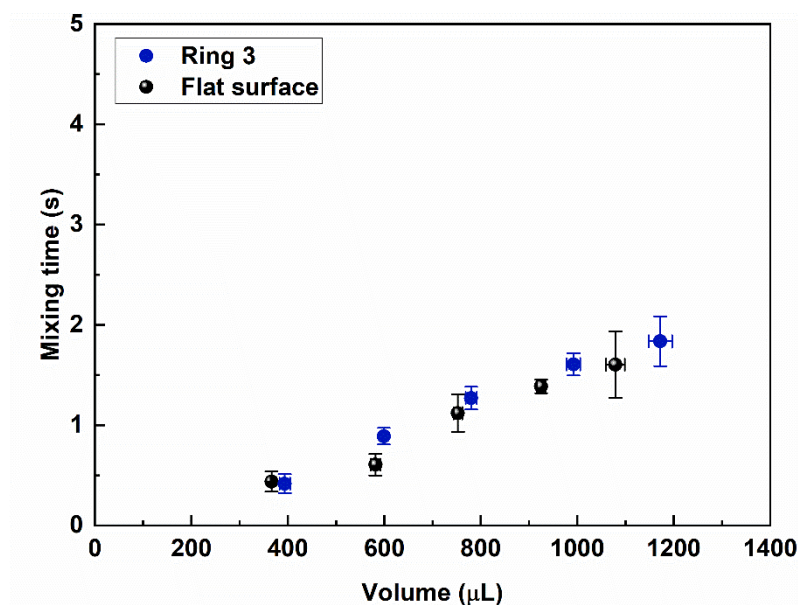


Figure 6.13 – Droplet mixing times observed on a heated flat surface (400 °C)

More frequent oscillations were observed after droplet collision, where the lobe mode N was on a range of 2-6 as shown in figure 6.14. But shortly, the oscillation became less violent with a declined lobe mode. The violent oscillation is interpreted to arise from the momentum of the coloured dye: The dye slid down the basin by gravity, then collided with the water droplet at the lowest point, where energy conversion took place in accordance with the law of conservation of momentum. The extra energy made an ultramobile Leidenfrost droplet undergo highly frequent oscillations until the energy is diminished. Consequently, the mixing efficiency was further improved. Note, droplet rotation also took place after the collision, which happened to be in a clockwise direction.

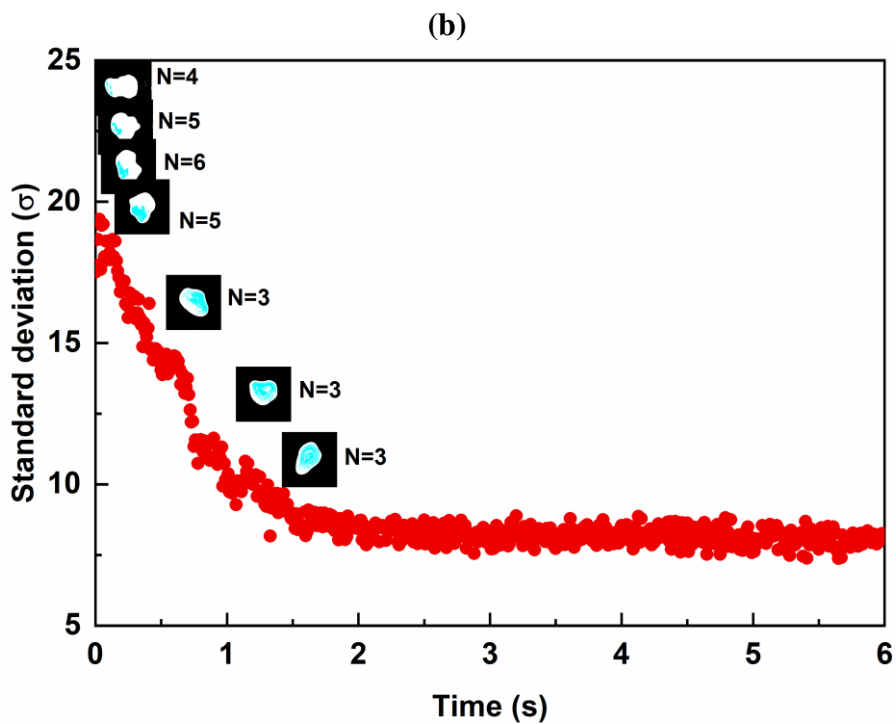
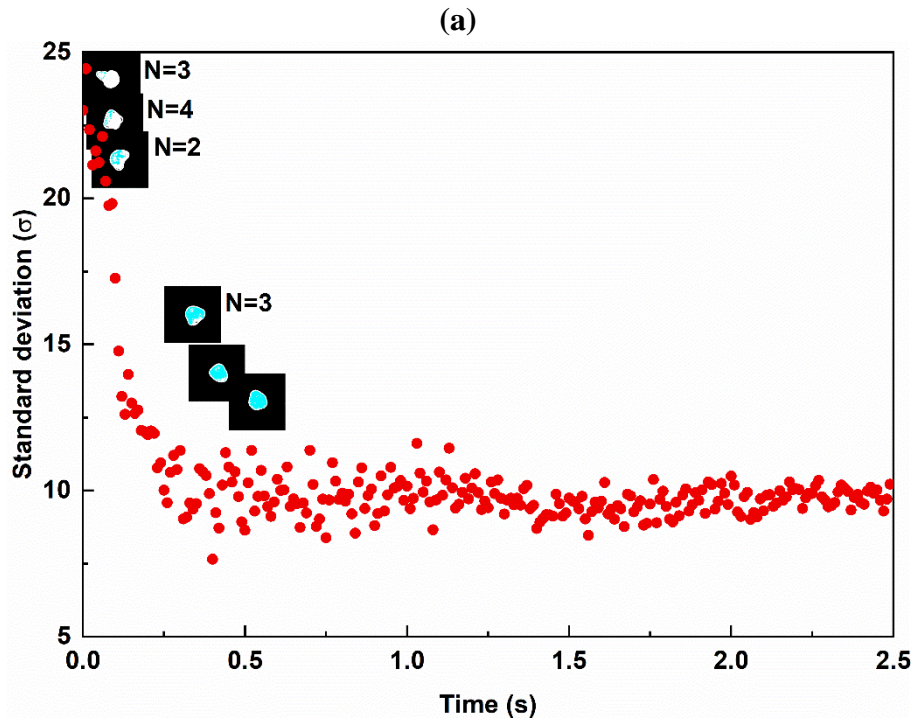


Figure 6.14 – Violent droplet oscillation after initial collisions; (a) and (b) are the standard deviation of the pixel values within the droplet region (region of interest, ROI), showing a small water droplet ($400\ \mu\text{L}$) and a large one ($1200\ \mu\text{L}$) respectively. Extracted images are attached. Surface was heated at $400\ ^\circ\text{C}$

6.3 Energy Loss by the Deformed Liquid

The repeated collisions between the deformed liquid and the rigid ratchets play an important role in the enhancement of mixing based on the analysis presented in Sections 6.1 and 6.2. The deformed liquid takes up only a small amount of the entire droplet, as shown in figure 6.15. Here, the volume is estimated according to equation 6.9, which is based on the deformation analysis in equation 4.30. Therefore, it is assumed that the bulk of the rolling cell is not influenced by the deformed region.

$$V_b \sim \sum \frac{1}{2} \lambda_e \phi w_i \sim \frac{1}{2} \frac{\lambda_e}{\lambda} C_1 \varepsilon A \quad (6.9)$$

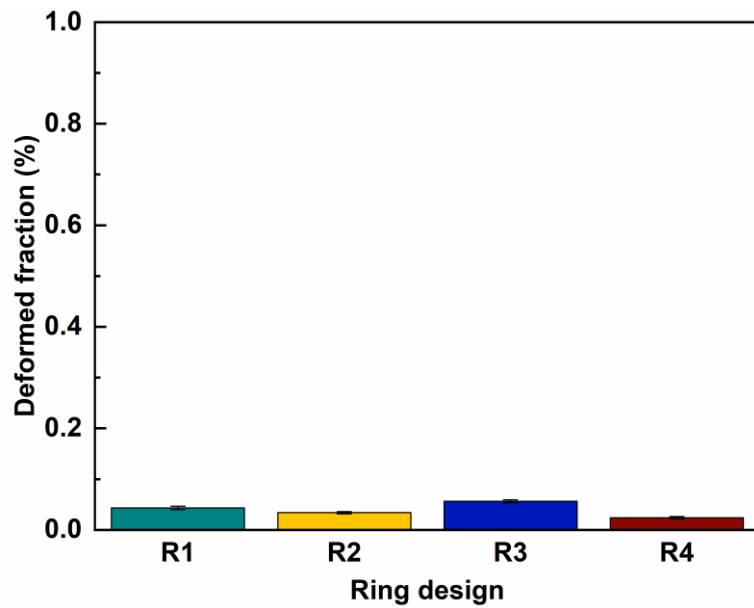


Figure 6.15 – Liquid volume trapped by the ratchet cavity

The small, deformed volumes cause significant friction to motion as analysed in 5.4.2. Assuming no rotation occurs, the energy loss caused by the friction (W_b) is then shown in figure 6.16, denoting W_f as the work from the driving force and E_v as the kinetic energy from droplet self-propulsion. This energy increased the turbulence within the deformed regions to enhance mixing. Assuming pure diffusion between the convective cells, at droplet width $w = 10$ mm and radius of convective cells $r = 1.5$ mm, the mixing time would take few seconds, $t_D = (w - 4r)^2 / (2D_{diff})$, which greatly dominates the mixing and opposes the mixing time measurement in figure 6.6b. Hence, it is speculated the field between the convective cells also has turbulent-like features.

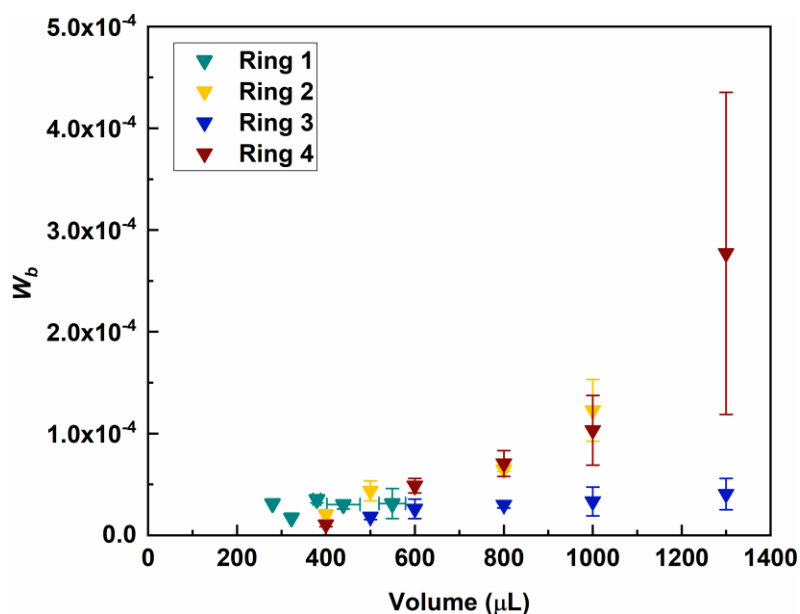


Figure 6.16 – Energy loss under the assumption of no droplet rotation

6.4 Chapter Conclusion

Using Leidenfrost self-propulsion dynamics, droplet mixing is greatly enhanced by convective internal flows. The convective flows originate from the Leidenfrost regime and the repeated collisions between the deformed liquids and the rigid ratchets. Mixing time has been remarkably reduced by over 100 times in comparison with pure diffusion at room temperature. The mixing time strongly depends on the droplet shape, which is determined by the ratchet designs. A larger ratchet ratio produces a smaller droplet velocity that comes along with a shorter droplet length, yielding a reduced mixing time. Larger ratchet cavity causes more liquid to be trapped, which further reduces the mixing time. According to previous report, a cold Leidenfrost regime also generates self-propulsion [38], suggesting that Leidenfrost self-propulsion dynamics could be a useful and efficient way for droplet mixing.

A slightly curved surface also demonstrates fast droplet mixing due to the onset of droplet oscillation at Leidenfrost state. Droplet oscillation becomes more violent after the Initial collision of the coloured dye with the water droplet, which further improves droplet mixing. However, a cold Leidenfrost regime may prohibit the oscillation due to insufficient vapour thickness.

Chapter 7 Conclusions and Future Work

7.1 Overall Aims

A Leidenfrost droplet is one that levitates on a vapour cushion, which allows the droplet to move in a frictionless manner whilst also displaying several interesting dynamical behaviours, *e.g.* convective internal fluid flow, droplet oscillation (on a flat surface) and droplet self-propulsion (on a ratcheted surface). The internal convection suggests an alternative way of droplet mixing, especially in diffusion dominated microfluidics. The remarkable speed of Leidenfrost self-propulsion then implies a promising technique for energy recovery and applications in flow chemistry. Based upon the gaps identified in the literature, four research themes were developed that aimed to form a fundamental understanding of the propulsion dynamics and to explore potential applications in droplet mixing. The main themes were:

- I. Scripting a code in MATLAB for automated image processing for droplet motion and colour detection.
- II. Developing a model to describe the propulsion dynamics in a quantitative manner.
- III. Performing experimental studies to test the robustness of the model.
- IV. Exploration of droplet mixing under the Leidenfrost state.

7.2 Main Outcomes

7.2.1 A General Model for Leidenfrost Self-Propulsion

This thesis presents a new general model that can be used to describe the propulsion dynamics of a Leidenfrost liquid on a ratcheted surface (*Chapter 4*). Based upon the viscous mechanism proposed in the literature, the model further considers droplet deformation at the presence of the ratchets for the first time. It therefore supersedes the previous and limited scaling analysis conducted in the literature by deducing a quantitative expression for the driving force. Apart from the dependence on the droplet size as proposed by the literature, the model also suggests that the driving force is also apparently impacted by the droplet deformation and ratchet parameters but has little dependence on the surface temperature. Further, a terminal velocity model is proposed through the extension of the driving force model, showing the dominant role of the ratchet ratio in determining the droplet terminal velocities.

7.2.2 Ratcheted Rings for Leidenfrost Self-Propulsion

Four ratcheted rings were purchased for conducting experimental studies of the Leidenfrost self-propulsion phenomena, where the droplet motion was captured by the use of a high-speed camera (*Chapter 5*). The ring shape allows droplets to self-propel in a shorter footprint whilst also enabling droplets to reach a terminal velocity. Both liquid streams and droplets can propel in these channel. The droplet velocity was observed to plateau in agreement with the predictions of the velocity model. These rings also show a unique feature of droplet self-propulsion: in addition to a steady state terminal velocity, the droplet width was also observed to plateau over time because of the stabilized centripetal force.

Droplet acceleration rates were observed to dramatically increase from 0.2 m/s^2 to 0.6 m/s^2 when the ratchet ratios decreased from 6.0 (*e.g.* ring design 3) to 2.1 (*e.g.* ring design 1). This can be explained by the model developed in *Chapter 4*. The flat ratchet top on ring designs 2&4 also prohibited droplet acceleration due to increased energy loss and a negative vapour flow that diminishes the ‘forward’ driving force.

By measuring the decreasing rate of the top-down contact area of a large self-propelling droplet, the energy conversion efficiency from the latent heat of phase transition into the droplet self-propulsion is evaluated to be very small: $\sim 4.5 \times 10^{-6}$. This is because most energy has been used to levitate the droplet. It is expected that energy conversion could be properly improved in a lower pressure ambient (*e.g.* outer space) and using alternative substances such as ices of H_2O , CO_2 and CH_4 .

7.2.3 Droplet Mixing under the Leidenfrost State

The thesis also presents a new method for fluid mixing using the Leidenfrost effect (*Chapter 6*). The mixing process was observed using a high-speed camera, showing a significant reduction of the mixing time of over 100 times in comparison to pure diffusion at room temperature (from a few minutes to no more than 5 s). Several mechanisms explain this improved mixing performance: convective cells inside the Leidenfrost droplet, repeated collisions during droplet self-propulsion and droplet oscillations on a flat surface. These dynamical activities bring more turbulence into the internal fluid flow, leading to a reduction in the diffusion distance.

Among the four ratcheted rings, the maximum mixing time reduced from ~ 5 s (on ring designs 1, 2, and 4) to ~ 2 s (on ring design 3). The lower diffusion resistance on ring design 3 results from the shorter droplet length, which arises from the less narrowed droplet width as discussed in *Chapter 5*.

7.2.4 Automated Image Processing

A custom programme is presented in this thesis, which is used to process the numerous experimental images in association with the open-source software ImageJ (Fiji). Manual analysis has also been carried out to test the accuracy of the programme, with a difference of only 0.75–3.82%. The programme is used to detect the droplet position, top-down contact area and mixing process. Simple centre-of-mass tracking in a limited space yields considerable errors for linear velocity analysis. This study provides a simple but efficient method to correct the error by integrating the effective radius distance using programme analysis.

7.3 Further Work

Extending the experimental verification of the model may start with studies on how the ratchet parameters (ratchet period and height) can affect the propulsion dynamics. For example, figures 5.15 and 5.16 provide limited experimental data to support the statement in terms of the driving force as a function of the ratchet parameters. A broader range of design will further test the robustness of the model presented in this reaserach, *e.g.* ratchet periods 1-1.5 mm and ratchet heights 0.3-0.5 mm (these are proposed based on the parameters shown in the literature).

From a practical perspective, it is worthwhile to explore droplet mixing/energy generation in a lower temperature regime. According to previous studies, the threshold temperature for Leidenfrost self-propulsion has been shifted to ~ 77 °C. However, the pinning effect arising from the contact angle hysteresis may prohibit droplet oscillation on a flat surface, which plays a negative role in the mixing process.

In terms of energy conversion applications, *e.g.* from thermal to kinetic and then to electric, the low conversion efficiency from heat to motion ($\sim 10^{-6}$) is a tough question to face with. In regards to chemical processes which commonly require ‘high’ temperatures (*e.g.* chemical reactions and/or mixing), the excellent result in droplet mixing then provides useful evidence

for applications of the Leidenfrost effect associated phenomenon to chemical engineering field. A further direction is to explore in what way the fast droplet mixing under the Leidenfrost effect could affect chemical reactions, in particular for those restricted by the mixing process, *e.g.* solution-phase AgNP synthesis. This will provide a fundamental basis for applications in flow chemistry.

Droplet mixing at micro scales will link potential applications to microfluidic systems, *e.g.* lab-on-a-chip field. Corresponding experiments require the fabrication of a microscaled ratcheted channel, whilst chronophotography using a camera with higher resolutions is also required. In order to have a clear map of the turbulent features that influence the mixing process, particle image velocimetry (PIV) is a useful tool to measure the internal fluid velocities.

References

1. Leidenfrost, J.G., *De Aquae Communis Nonullis Qualitatibus Tractatus - On the fixation of water in diverse fire. A Tract about some Qualities of Common Water (translated into English by Wares C 1966 International Journal of Heat and Mass Transfer* **9** 1153-1166).
2. Walker, J., *Boiling and the Leidenfrost Effect*. Fundamentals of Physics, 2010: p. E10-1.
3. Thimbleby, H., *The Leidenfrost Phenomenon*. Physics Education, 1989. **24**(5): p. 300-303.
4. Stewart, S.M., *Leidenfrost Drop Dynamics: a Forgotten Past and Modern Day Rediscoveries*. European Journal of Physics, 2022. **43**(2): p. 023001.
5. Hall, R.S., et al., *Inverse Leidenfrost Phenomenon*. Nature, 1969. **224**(5216): p. 266-267.
6. Snezhko, A., E. Ben Jacob, and I. S Aranson, *Pulsating–Gliding Transition in the Dynamics of Levitating Liquid Nitrogen Droplets*. New Journal of Physics, 2008. **10**(4): p. 043034.
7. Adda-Bedia, M., et al., *Inverse Leidenfrost Effect: Levitating Drops on Liquid Nitrogen*. Langmuir, 2016. **32**(17): p. 4179-4188.
8. Janssens, S.D., S. Koizumi, and E. Fried, *Behavior of Self-Propelled Acetone Droplets in a Leidenfrost State on Liquid Substrates*. Physics of Fluids, 2017. **29**(3): p. 32103.
9. Gauthier, A., et al., *Self-Propulsion of Inverse Leidenfrost Drops on a Cryogenic Bath*. Proceedings of the National Academy of Sciences - PNAS, 2019. **116**(4): p. 1174-1179.
10. Scott, R.W., et al., *Coupling the Leidenfrost Effect and Elastic Deformations to Power Sustained Bouncing*. Nature Physics, 2017. **13**(11): p. 1095-1099.
11. Bernardin, J.D. and I. Mudawar, *The Leidenfrost Point: Experimental Study and Assessment of Existing Models*. Journal of Heat Transfer, 1999. **121**(4): p. 894-903.
12. Cai, C., et al., *Theoretical Leidenfrost Point (LFP) Model for Sessile Droplet*. International Journal of Heat and Mass Transfer, 2020. **146**: p. 118802.
13. Talari, V., et al., *Leidenfrost Drops on Micro/Nanostructured Surfaces*. Frontiers in Energy, 2018. **12**(1): p. 22-42.
14. Lee, G.C., et al., *Measurement of the Vapor Layer under a Dynamic Leidenfrost Drop*. International Journal of Heat and Mass Transfer, 2018. **124**(C): p. 1163-1171.
15. Anne-Laure, B., C. Clanet, and D. Quéré, *Leidenfrost Drops*. Physics of Fluids, 2003. **15**(6): p. 1632-1637.
16. Kwon, H.-M., J.C. Bird, and K.K. Varanasi, *Increasing Leidenfrost Point Using Micro-Nano Hierarchical Surface structures*. Applied Physics Letters, 2013. **103**(20): p. 201601.

17. Ng, B.T., Y.M. Hung, and M.K. Tan, *Suppression of the Leidenfrost Effect via Low Frequency Vibrations*. *Soft Matter*, 2014. **11**(4): p. 775-784.
18. Jiang, M., et al., *Inhibiting the Leidenfrost Effect above 1,000 °C for Sustained Thermal Cooling*. *Nature*, 2022. **601**(7894): p. 568-572.
19. Vakarelski, I., U., et al., *Stabilization of Leidenfrost Vapour Layer by Textured Superhydrophobic Surfaces*. *Nature*, 2012. **489**(7415): p. 274-277.
20. Bianco, A.-L., et al., *On the Elasticity of an Inertial Liquid Shock*. *Journal of Fluid Mechanics*, 2006. **554**: p. 47-66.
21. Graeber, G., et al., *Leidenfrost Droplet Trampolining*. *Nature Communications*, 2021. **12**(1): p. 1727-1727.
22. Bouillant, A., et al., *Leidenfrost Wheels*. *Nature Physics*, 2018. **14**(12): p. 1188-1192.
23. Bouillant, A., et al., *Thermophobic Leidenfrost*. *Soft Matter*, 2021. **17**(39): p. 885-889.
24. Linke, H., et al., *Self-propelled Leidenfrost Droplets*. *Physical Review Letters*, 2006. **96**(15): p. 154502.
25. Ma, X., J.-J. Liétor-Santos, and J.C. Burton, *Star-Shaped Oscillations of Leidenfrost Drops*. *Physical Review Fluids*, 2017. **2**(3): p. 031602.
26. Holter, N.J. and W.R. Glasscock, *Vibrations of Evaporating Liquid Drops*. *The Journal of the Acoustical Society of America*, 1952. **24**(6): p. 682-686.
27. Strier, D.E., et al., *Nitrogen Stars: Morphogenesis of a Liquid Drop*. *Physica A*, 2000. **283**(1): p. 261-266.
28. Celestini, F., et al., *Two Dimensional Leidenfrost Droplets in a Hele-Shaw Cell*. *Physics of Fluids*, 2014. **26**(3): p. 32103.
29. Hardt, S., S. Tiwari, and T. Baier, *Thermally Driven Flows Between a Leidenfrost Solid and a Ratchet Surface*. *Physical Review E*, 2013. **87**(6): p. 063015.
30. Marín, Á.G., et al., *Capillary Droplets on Leidenfrost Micro-Ratchets*. *Physics of Fluids*, 2012. **24**(12): p. 122001.
31. Wells, G.G., et al., *A Sublimation Heat Engine*. *Nature Communications*, 2015. **6**(1): p. 6390.
32. Agrawal, P., et al., *Leidenfrost Heat Engine: Sustained Rotation of Levitating Rotors on Turbine-Inspired Substrates*. *Applied Energy*, 2019. **240**: p. 399-408.
33. Caballero, D., et al., *Motion in Microfluidic Ratchets*. *Lab on a Chip*, 2016. **16**(23): p. 4477-4481.
34. Pease, R., *Scientists Make Water Run Uphill*. 2006, BBC News.

35. Stroock, A.D., et al., *Chaotic Mixer for Microchannels*. Science., 2002. **1066238**(647): p. 647-651.
36. Ling-Chin, J., et al., *State-of-the-Art Technologies on Low-Grade Heat Recovery and Utilization in Industry*. Energy Conversion-Current Technologies and Future Trends, 2018. **21**.
37. EU, I.-C. *Low-Grade Waste Heat Utilization in the European Union*. 2017 [cited 2022 12 December]; Available from: <https://www.interreg-central.eu/Content.Node/CE-HEAT/Low-grade-waste-heat-utilization-in-the-European-Union.html>.
38. Dupeux, G., et al., *Propulsion on a Superhydrophobic Ratchet*. Scientific Reports, 2014. **4**(1): p. 5280.
39. Arnaldo del Cerro, D., et al., *Leidenfrost Point Reduction on Micropatterned Metallic Surfaces*. Langmuir, 2012. **28**(42): p. 15106-15110.
40. Vakarelski, I.U., D.Y.C. Chan, and S.T. Thoroddsen, *Leidenfrost Vapour Layer Moderation of the Drag Crisis and Trajectories of Superhydrophobic and Hydrophilic Spheres Falling in Water*. Soft Matter, 2014. **10**(31): p. 5662-5668.
41. Saranadhi, D., et al., *Sustained Drag Reduction in a Turbulent Flow using a Low-Temperature Leidenfrost Surface*. Science Advances, 2016. **2**(10): p. e1600686-e1600686.
42. Dupeux, G., et al., *Viscous Mechanism for Leidenfrost Propulsion on a Ratchet*. EPL (Europhysics Letters), 2011. **96**(5): p. 58001.
43. Cousins, T.R., et al., *A Ratchet Trap for Leidenfrost Drops*. Journal of Fluid Mechanics, 2012. **696**: p. 215-227.
44. Vakarelski, I.U., et al., *Drag Reduction by Leidenfrost Vapor Layers*. Physical Review Letters, 2011. **106**(21): p. 214501-214501.
45. Malouin, B.A., et al., *Directed Rebounding of Droplets by Microscale Surface Roughness Gradients*. Applied Physics Letters, 2010. **96**(23): p. 234103.
46. Wu, J., et al., *Do Droplets Always Move Following the Wettability Gradient?* Applied Physics Letters, 2011. **98**(20): p. 204104.
47. Lafuma, A. and D. Quéré, *Superhydrophobic States*. Nature Materials, 2003. **2**(7): p. 457-460.
48. Richard, D., C. Clanet, and D. Quéré, *Contact Time of a Bouncing Drop*. Nature, 2002. **417**(6891): p. 811.

49. Agapov, R.L., et al., *Asymmetric Wettability of Nanostructures Directs Leidenfrost Droplets*. ACS Nano, 2014. **8**(1): p. 860-867.
50. Agapov, R.L., et al., *Length scale of Leidenfrost Ratchet Switches Droplet Directionality*. Nanoscale, 2014. **6**(15): p. 9293-9299.
51. Chu, K.-H., R. Xiao, and E. Wang, N., *Uni-Directional Liquid Spreading on Asymmetric Nanostructured Surfaces*. Nature Materials, 2010. **9**(5): p. 413-417.
52. Reyssat, M., F. Pardo, and D. Quéré, *Drops onto Gradients of Texture*. EPL (Europhysics Letters), 2009. **87**(3): p. 36003.
53. Malvadkar, N., A., et al., *An Engineered Anisotropic Nanofilm with Unidirectional Wetting Properties*. Nature Materials, 2010. **9**(12): p. 1023-1028.
54. Sobac, B., et al., *Self-Propelled Leidenfrost Drops on a Thermal Gradient: A Theoretical Study*. Physics of Fluids, 2017. **29**(8): p. 82101.
55. Buguin, A., L. Talini, and P. Silberzan, *Ratchet-Like Topological Structures for the Control of Microdrops*. Applied Physics A, 2002. **75**(2): p. 207-212.
56. John, K., P. Hänggi, and U. Thiele, *Ratchet-Driven Fluid Transport in Bounded Two-Layer Films of Immiscible Liquids*. Soft Matter, 2008. **4**(6): p. 1183-1195.
57. Thiele, U. and K. John, *Transport of Free Surface Liquid Films and Drops by External Ratchets and Self-Ratcheting Mechanisms*. Chemical Physics, 2010. **375**(2-3): p. 578-586.
58. Prakash, M., D. Quéré, and J.W.M. Bush, *Surface Tension Transport of Prey by Feeding Shorebirds the Capillary Ratchet*. Science (New York, N.Y.), 2008. **320**(5878): p. 931-934.
59. Feng, S., et al., *Three-Dimensional Capillary Ratchet-Induced Liquid Directional Steering*. Science, 2021. **373**(6561): p. 1344-1348.
60. Scriven, L.E. and C.V. Sternling, *The Marangoni Effects*. Nature, 1960. **187**(4733): p. 186-188.
61. Brochard, F., *Motions of Droplets on Solid Surfaces Induced by Chemical or Thermal Gradients*. Langmuir, 1989. **5**(2): p. 432-438.
62. Chaudhury, M.K. and G.M. Whitesides, *How to Make Water Run Uphill*. Science (New York, N.Y.), 1992. **256**(5063): p. 1539-1541.
63. Ichimura, K., S.-K. Oh, and M. Nakagawa, *Light-Driven Motion of Liquids on a Photoresponsive Surface*. Science, 2000. **288**(5471): p. 1624-1626.
64. Bico, J. and D. Quéré, *Self-Propelling Slugs*. Journal of Fluid Mechanics, 2002. **467**: p. 101-127.

65. Quéré, D., *Leidenfrost Dynamics*. Annual Review of Fluid Mechanics, 2013. **45**(1): p. 197-215.
66. Bonn, D., et al., *Wetting and Spreading*. Reviews of Modern Physics, 2009. **81**(2): p. 739-805.
67. Quéré, D., *Wetting and Roughness*. Annual Review of Materials Research, 2008. **38**(1): p. 71-99.
68. Ma, X. and J.C. Burton, *Self-Organized Oscillations of Leidenfrost Drops*. Journal of Fluid Mechanics, 2018. **846**: p. 263-291.
69. Bouillant, A., et al., *Self-Excitation of Leidenfrost Drops and Consequences on Their Stability*. Proceedings of the National Academy of Sciences, 2021. **118**(26): p. 1.
70. Choi, C.Q. *250-year-old Leidenfrost Effect May Help Design Future Self-Propelled Devices*. 2018 [cited 12 December, 2022]; Available from: <https://www.insidescience.org/news/250-year-old-leidenfrost-effect-may-help-design-future-self-propelled-devices>.
71. Chiu, Y.-t. and C.-I. Sun. *Excellent Mixing with Coalescence of Leidenfrost Drops*. 2019; Available from: <https://www.youtube.com/watch?v=Z6PUMxWykoY>.
72. Harvey, D., J.M. Harper, and J.C. Burton, *Minimum Leidenfrost Temperature on Smooth Surfaces*. Physical Review Letters, 2021. **127**(10): p. 104501-104501.
73. Pham, J.T., et al., *Spontaneous Jumping, Bouncing and Trampolining of Hydrogel Drops on a Heated Plate*. Nature communications, 2017. **8**(1): p. 905.
74. Schutzius, T.M., et al., *Spontaneous Droplet Trampolining on Rigid Superhydrophobic Surfaces*. Nature, 2015. **527**(7576): p. 82-85.
75. Khattak, H.K., S.R. Waitukaitis, and A.D. Slepko, *Microwave Induced Mechanical Activation of Hydrogel Dimers*. Soft Matter, 2019. **15**(29): p. 5804-5809.
76. Ok, J., et al., *Propulsion of Droplets on Micro- and Sub-Micron Ratchet Surfaces in the Leidenfrost Temperature Regime*. Microfluidics and Nanofluidics, 2011. **10**(5): p. 1045-1054.
77. Grounds, A., R. Still, and K. Takashina, *Enhanced Droplet Control by Transition Boiling*. Scientific Reports, 2012. **2**(1): p. 720.
78. Bradfield, W.S., *Liquid-Solid Contact in Stable Film Boiling*. Industrial and Engineering Chemistry Fundamentals, 1966. **5**(2): p. 200-204.
79. Lagubeau, G., et al., *Leidenfrost on a Ratchet*. Nature Physics, 2011. **7**(5): p. 395-398.

80. Würger, A., *Leidenfrost Gas Ratchets Driven by Thermal Creep*. Physical Review Letters, 2011. **107**(16): p. 164502.
81. Mrinal, M., X. Wang, and C. Luo, *Self-Rotation-Induced Propulsion of a Leidenfrost Drop on a Ratchet*. Langmuir, 2017. **33**(25): p. 6307-6313.
82. Soto, D., et al., *Surfing on a Herringbone*. Physical Review Fluids, 2016. **1**(1): p. 013902.
83. Dupeux, G., et al., *Self-Propelling Uneven Leidenfrost Solids*. Physics of Fluids, 2013. **25**(5): p. 051704.
84. Dodd, L.E., et al., *Low-Friction Self-Centering Droplet Propulsion and Transport Using a Leidenfrost Herringbone-Ratchet Structure*. Physical Review Applied, 2019. **11**(3): p. 034063.
85. Soto, D., et al., *Air-Levitated Platelets: from Take off to Motion*. Journal of Fluid Mechanics, 2017. **814**: p. 535-546.
86. Kruse, C., et al., *Self-Propelled Droplets on Heated Surfaces with Angled Self-Assembled Micro/Nanostructures*. Microfluidics and Nanofluidics, 2015. **18**(5-6): p. 1417-1424.
87. Kim, H., et al., *Effects of Micro/Nano-Scale Surface Characteristics on the Leidenfrost Point Temperature of Water*. Journal of Thermal Science and Technology, 2012. **7**(3): p. 453-462.
88. Kim, H., et al., *On the Effect of Surface Roughness Height, Wettability, and Nanoporosity on Leidenfrost Phenomena*. Applied Physics Letters, 2011. **98**(8): p. 083121.
89. Rodrigues, J. and S. Desai, *The Nanoscale Leidenfrost Effect*. Nanoscale, 2019. **11**(25): p. 12139-12151.
90. Kruse, C., et al., *Extraordinary Shifts of the Leidenfrost Temperature from Multiscale Micro/Nanostructured Surfaces*. Langmuir, 2013. **29**(31): p. 9798-9806.
91. Ok, J.T., et al., *Effect of Different Fluids on Rectified Motion of Leidenfrost Droplets on Micro/Sub-Micron Ratchets*. Microelectronic Engineering, 2016. **158**: p. 130-134.
92. Ok, J.T., et al., *Effect of Surface Wetting of Micro/Nano Ratchets on Leidenfrost Liquid Drop Motion*, in *ASME 2009 7th International Conference on Nanochannels, Microchannels, and Minichannels*. 2009. p. 1037-1041.
93. Tran, T., et al., *Drop Impact on Superheated Surfaces*. Physical Review Letters, 2012. **108**(3): p. 036101-036101.
94. Tran, T., et al., *Droplet Impact on Superheated Micro-Structured Surfaces*. Soft Matter, 2013. **9**(12): p. 3272.

95. Bourrienne, P., C. Lv, and D. Quéré, *The Cold Leidenfrost Regime*. Science Advances, 2019. **5**(6): p. eaaw0304.
96. Feng, R., et al., *Ratchet Composite Thin Film for Low-Temperature Self-Propelled Leidenfrost Droplet*. Journal of Colloid and Interface Science, 2012. **367**(1): p. 450-454.
97. De Gennes, P.G., *Wetting: Statics and Dynamics*. Reviews of Modern Physics, 1985. **57**(3): p. 827-863.
98. Dubnack, O., et al., *Laser-Induced Leidenfrost Surfaces*. Applied Surface Science, 2020. **532**: p. 147407.
99. Baier, T., et al., *Propulsion Mechanisms for Leidenfrost Solids on Ratchets*. Physical Review E, 2012. **87**(2): p. 021001.
100. Dupeux, G., et al., *Trapping Leidenfrost Drops with Crenelations*. Physical Review Letters, 2011. **107**(11): p. 114503.
101. Hashmi, A., et al., *Leidenfrost Levitation: Beyond Droplets*. Scientific Reports, 2012. **2**(1): p. 797.
102. Edalatpour, M., et al., *Three-Phase Leidenfrost Effect*. Physical Review Fluids, 2022. **7**(1): p. 014004.
103. Bird, R.B., W.E. Stewart, and E.N. Lightfoot, *Transport Phenomena*. 2007, Chichester, New York: Wiley.
104. Lagubeau, G., et al., *Leidenfrost on a ratchet*. Nature Physics, 2011. **7**(5): p. 395-398.
105. Jia, Z.-H., M.-Y. Chen, and H.-T. Zhu, *Reversible Self-Propelled Leidenfrost Droplets on Ratchet Surfaces*. Applied Physics Letters, 2017. **110**(9): p. 091603.
106. Mahadevan, L. and Y. Pomeau, *Rolling Droplets*. Physics of Fluids, 1999. **11**(9): p. 2449-2453.
107. Richard, D. and D. Quéré, *Viscous Drops Rolling on a Tilted Non-Wettable Solid*. EPL (Europhysics Letters), 1999. **48**(3): p. 286-291.
108. Abdelaziz, R., et al., *Green Chemistry and Nanofabrication in a Levitated Leidenfrost Drop*. Nature communications, 2013. **4**(1): p. 2400.
109. Westphall, M.S., K. Jorabchi, and L.M. Smith, *Mass Spectrometry of Acoustically Levitated Droplets*. Analytical chemistry (Washington), 2008. **80**(15): p. 5847-5853.
110. Saha, S., et al., *Direct analysis of anabolic steroids in urine using Leidenfrost phenomenon assisted thermal desorption-dielectric barrier discharge ionization mass spectrometry*. Analytica chimica acta, 2014. **839**: p. 1-7.

111. Lee, D.-W., et al., *Straightforward Synthesis of Metal Nanoparticles and Hierarchical Porous Metals Assisted by Partial Film Boiling Phenomena*. Chemistry of materials, 2015. **27**(15): p. 5151-5160.
112. Bain, R.M., et al., *Accelerated Chemical Reactions and Organic Synthesis in Leidenfrost Droplets*. Angewandte Chemie (International ed.), 2016. **55**(35): p. 10478-10482.
113. Wciślik, S., *Thermal Infrared Mapping of the Leidenfrost Drop Evaporation*. 2016.
114. Sugioka, H., S. Segawa, and M. Kubota, *High-Speed Side-Shooter Using Leidenfrost Phenomena*. Journal of Applied Physics, 2019. **125**(13): p. 134502.
115. Sugioka, H., M. Kubota, and S. Segawa, *Leidenfrost Mixer*. Japanese Journal of Applied Physics, 2019. **58**(4): p. 048001.
116. Guillaume, L., et al., *Leidenfrost on a Ratchet*. Nature Physics, 2011. **7**(5): p. 395.
117. Marín, Á.G., et al., *Capillary Droplets on Leidenfrost Micro-Ratchets*. Physics of Fluids, 2012. **24**(12).
118. Schindelin, J., et al., *Fiji: An Open-Source Platform for Biological-Image Analysis*. Nature Methods, 2012. **9**(7): p. 676-682.
119. Mahmud, F. and K.F. Tamrin, *Method for Determining Mixing Index in Microfluidics by RGB Color Model*. Asia-Pacific Journal of Chemical Engineering, 2020. **15**(2): p. e2407.
120. Paik, P., et al., *Electrowetting-Based Droplet Mixers for Microfluidic Systems*. Lab on a Chip, 2003. **3**(1): p. 28-33.
121. Paik, P., V.K. Pamula, and R.B. Fair, *Rapid Droplet Mixers for Digital Microfluidic Systems*. Lab on a Chip, 2003. **3**(4): p. 253-259.
122. Avedisian, C.T. and J. Koplik, *Leidenfrost Boiling of Methanol Droplets on Hot Porous/Ceramic Surfaces*. International Journal of Heat and Mass Transfer, 1987. **30**(2): p. 379-393.
123. Arter, J.M., et al., *Self-Propelling Leidenfrost Droplets on a Variable Topography Surface*. Applied physics letters, 2018. **113**(24): p. 243704.
124. B. S. Gottfried, C. J. Lee, and K.J. Bell, *The Leidenfrost Phenomenon: Film Boiling of Liquid Droplets on a Flat Plate*. Int. J. Heat Mass Transfer., 1966. **9**: p. 1167-1187.
125. Gary, G.W., et al., *A Sublimation Heat Engine*. Nature Communications, 2015. **6**(1).
126. Fowler, J., H. Moon, and C.-J. Kim, *Enhancement of Mixing by Droplet-based Microfluidics*. MEMS 2002 : the Fifteenth IEEE International Conference on Micro Electro Mechanical Systems : technical digest : Las Vegas, Nevada, USA, January 20-24, 2002, 2002: p. 97-100.

127. Lee, J., et al., *Addressable Micro Liquid Handling by Electric Control of Surface Tension*. The 14th IEEE International Conference on Micro Electro Mechanical Systems : MEMS 2001 : Interlaken, Switzerland, January 21-25, 2001, 2001: p. 499-502.
128. Song, H., et al., *Experimental Test of Scaling of Mixing by Chaotic Advection in Droplets Moving through Microfluidic Channels*. Applied Physics Letters, 2003. **83**(22): p. 4664-4666.
129. McDonough, J.R., et al., *Micromixing in Oscillatory Baffled Flows*. Chemical Engineering Journal, 2019. **361**: p. 508-518.
130. Dash, S., et al., *Buoyancy-Induced on-the-Spot Mixing in Droplets Evaporating on Nonwetting Surfaces*. Physical Review E, 2014. **90**(6): p. 062407-062407.
131. Yim, E., A. Bouillant, and F. Gallaire, *Buoyancy-Driven Convection of Droplets on Hot Nonwetting Surfaces*. Physical Review E, 2021. **103**(5): p. 053105-053105.
132. Bouillant, A., et al., *Symmetry Breaking in Leidenfrost Flows*. Physical Review Fluids, 2018. **3**(10): p. 100502.
133. Yim, E., et al., *Stability of Leidenfrost Drop Inner Flows*. 2020.
134. Ottino, J.M., *the Kinematics of Mixing: Stretching and Chaos, and Transport*. 1989, Cambridge, New York: Cambridge University Press.
135. Maquet, L., P. Colinet, and S. Dorbolo, *Organization of Microbeads in Leidenfrost Drops*. Soft Matter, 2014. **10**(23): p. 4061-4066.
136. Gommès, C.J. and J. Tharakan, *The Péclet Number of A Casino: Diffusion and Convection in A Gambling Context*. American Journal of Physics, 2020. **88**(6): p. 439-447.
137. Burton, J.C., et al., *Geometry of the Vapor Layer Under a Leidenfrost Drop*. Physical Review Letters, 2012. **109**(7): p. 074301-074301.
138. Singla, T. and M. Rivera, *Sounds of Leidenfrost Drops*. Physical Review Fluids, 2020. **5**(11): p. 113604.
139. Bergen, J.E., B.C. Basso, and J.B. Bostwick, *Leidenfrost Drop Dynamics: Exciting Dormant Modes*. Physical Review Fluids, 2019. **4**(8): p. 083603.

Appendix A. Image Processing

```

%%%%%%%%%%%%%%%%%%%%%%%%%%%%%%%%%%%%%%%%%%%%%%%%%%%%%%%%%%%%%%%%%%%%%%%% Import images %%%%%%%%%%%%%%%%%%%%%%%%%%%%%%%%%%%%%%%%%%%%%%%%%%%%%%%%%%%%%%%%%%%%%%%%%

img_path_list = dir('*.tif');
img_num = length(img_path_list); % number of images

if img_num > 0
    for pn = 1:img_num
        image_name = img_path_list(pn).name; % name the images by orders
        img_origin = imread(image_name);
        I[75] = double(img_origin);
        fprintf('%d %s\n',pn,image_name);
    end
end

%%%%%%%%%%%%%%%%%%%%%%%%%%%%%%%%%%%%%%%%%%%%%%%%%%%%%%%%%%%%%%%%%%%%%%%% Filter noises %%%%%%%%%%%%%%%%%%%%%%%%%%%%%%%%%%%%%%%%%%%%%%%%%%%%%%%%%%%%%%%%%%%%%%%%%

for k = 1:(img_num-1)
    Ibw{1,k} = im2bw(I{1,k},graythresh(I{1,k}));
    [height1,width1] = size(Ibw{1,k}); % Image size
    R1 = fix((height1-1)/2);
end

I0bw = im2bw(I{1,img_num},graythresh(I{1,img_num}));
[height0,width0] = size(I0bw); % Ring center, no ratchets
R0 = fix((height0-1)/2);

i0 = fix((1+height1)/2); % Edges, containing ratchets
j0 = fix((1+width1)/2);
imin = i0-R0;
imax = i0+R0;
jmin = j0-R0;
jmax = j0+R0;

%%%%%%%%%%%%%%%%%%%%%%%%%%%%%%%%%%%%%%%%%%%%%%%%%%%%%%%%%%%%%%%%%%%%%%%% Filter definition %%%%%%%%%%%%%%%%%%%%%%%%%%%%%%%%%%%%%%%%%%%%%%%%%%%%%%%%%%%%%%%%%%%%%%%%%
%%%%%%%%%%%%%%%%%%%%%%%%%%%%%%%%%%%%%%%%%%%%%%%%%%%%%%%%%%%%%%%%%%%%%%%% 0 is droplet & noise, and 1 is background %%%%%%%%%%%%%%%%%%%%%%%%%%%%%%%%%%%%%%%%%%%%%%%%%%%%%%%%%%%%%%%%%%%%%%%%%

for m = 1:(img_num-1)

    %% Filter noise in the ring centre
    for i = imin:imax
        for j = jmin:jmax
            if ((i-i0).^2 + (j-j0).^2) <= (R0^2)
                Ibw{1,m}(i,j) = 1;
            end
        end
    end

    %% Filter noise in the edges
    for i = 1:35
        for j = 35:(width1-34) % Top
            if Ibw{1,m}(i,j) == 0
                if sum(sum(Ibw{1,m}(1:69,(j-34):(j+34)))) >= 4730
                    Ibw{1,m}(i:(i+6),(j-3):(j+3)) = ones(7,7);
                end
            end
        end
    end
end

```

```

end

for i = (height1-34):height1
    for j = 35:(width1-34) % Bottom
        if Ibw{1,m}(i,j) == 0
            if sum(sum(Ibw{1,m}...
                ((height1-68):height1,(j-34):(j+34)))) >= 4730
                Ibw{1,m}((i-6):i,(j-3):(j+3)) = ones(7,7);
            end
        end
    end
end

for j = 1:35
    for i = 35:(height1-34) % Left
        if Ibw{1,m}(i,j) == 0
            if sum(sum(Ibw{1,m}((i-34):(i+34),1:69))) >= 4730
                Ibw{1,m}((i-3):(i+3),j:(j+6)) = ones(7,7);
            end
        end
    end
end

for j = (width1-34):width1
    for i = 35:(height1-34) % Right
        if Ibw{1,m}(i,j) == 0
            if sum(sum(Ibw{1,m}...
                ((i-34):(i+34),(width1-68):width1))) >= 4730
                Ibw{1,m}((i-3):(i+3),(j-6):j) = ones(7,7);
            end
        end
    end
end

%% Filter noise in the main field
for i = 36:(height1-35)
    for j= 36:(width1-35)
        if Ibw{1,m}(i,j) == 0
            if sum(sum(Ibw{1,m}...
                ((i-34):(i+34),(j-34):(j+34)))) >= 4730
                Ibw{1,m}((i-3):(i+3),(j-3):(j+3)) = ones(7,7);
            end
        end
    end
end

%%%%%%%%%%%%%%%%%%%%%%%%%%%%%%%%%%%%%%%%%%%%%%%%%%%%%%%%%%%%%%%%%%%%%%%%%% Second pass %%%%%%%%%%%%%%%%%%%%%%%%%%%%%%%%%%%%%%%%%%%%%%%%%%%%%%%%%%%%%%%%%%%%%%%%%%%

for i = 1:10
    for j = 11:(width1-10) % Top edge
        if Ibw{1,m}(i,j) == 0
            if sum(sum(Ibw{1,m}(1:21,(j-10):(j+10)))) >= 426
                Ibw{1,m}(1:13,(j-6):(j+6)) = ones(13,13);
            end
        end
    end
end

```

```

for i = (height1-9):height1
    for j = 11:(width1-10) % Bottom edge
        if Ibw{1,m}(i,j) == 0
            if sum(sum(Ibw{1,m}...
                ((height1-20):height1,(j-10):(j+10)))) >= 426
                Ibw{1,m}...
                ((height1-12):height1,(j-6):(j+6)) = ones(13,13);
            end
        end
    end
end

```

```

for j = 1:10
    for i = 11:(height1-10) % Left edge
        if Ibw{1,m}(i,j) == 0
            if sum(sum(Ibw{1,m}((i-10):(i+10),1:21))) >= 426
                Ibw{1,m}((i-6):(i+6),1:13) = ones(13,13);
            end
        end
    end
end

```

```

for j = (width1-9):width1
    for i = 11:(height1-10) % Right edge
        if Ibw{1,m}(i,j) == 0
            if sum(sum(Ibw{1,m}((i-10):(i+10),...
                (width1-20):width1))) >= 426
                Ibw{1,m}...
                ((i-6):(i+6),(width1-12):width1) = ones(13,13);
            end
        end
    end
end

```

```

for i = 11:(height1-10)
    for j = 11:(width1-10) % Main field
        if sum(sum(Ibw{1,m}...
            ((i-10):(i+10),(j-10):(j+10)))) >= 426
            Ibw{1,m}...
            ((i-6):(i+6),(j-6):(j+6)) = ones(13,13);
        end
    end
end

```

%%%%%%%%%% Connect Droplet Area %%%%%%%%%%

%% Horizontal connection

```

for i = 1:height1
    for j = 1:width1-30
        if Ibw{1,m}(i,j) == 0
            if Ibw{1,m}(i,j+30) == 0
                Ibw{1,m}(i,j:(j+30)) = zeros(1,31);
            end
        end
    end
end

```

```

    end
end

%% Vertical connection
for i = 1:height1-15
    for j = 1:width1
        if Ibw{1,m}(i,j) == 0
            if Ibw{1,m}(i+15,j) == 0
                Ibw{1,m}(i:(i+15),j)=zeros(16,1);
            end
        end
    end
end
end

end

%%%%%%%%%%%%%%%%%%%%%%%%%%%%%%%%%%%%%%%%%%%%%%%%%%%%%%%%%%%%%%%%%%%%%%%% Fill the Lost %%%%%%%%%%%%%%%%%%%%%%%%%%%%%%%%%%%%%%%%%%%%%%%%%%%%%%%%%%%%%%%%%%%%%%%%%

%% Define the boundary where the droplet rotates
for m = 30:(img_num-1)
    for i = 1:height1
        for j = 1:width1
            if fix(((i-i0)^2+(j-j0)^2)^0.5) == R1
                I1{1,m}(i,j) = 0;
            end
        end
    end
end

for m = 1:(img_num-1)
% Label the white regions in 8-connection region
[L_1{1,m},num] = bwlabel(Ibw{1,m},8);
% Calculate the areas for the labelled white regions
S_1 = regionprops(L_1{1,m}, 'area');
% Remove the white regions
I1{1,m} = ismember(L_1{1,m}, find([S_1.Area]>=5000));
end

%% Remove the boundary
for m = 1:(img_num-1)
    for i = 1:height1
        for j = 1:width1
            if fix(((i-i0)^2+(j-j0)^2)^0.5) == R1
                I2{1,m}(i,j) = 1;
            end
        end
    end
end
end
end

```


Appendix B. Droplet Detection

```
%%%%%%%%%% Calculate the Centre-of-Mass and Droplet Area %%%%%%%%%%%

x = zeros(1,img_num-1);
y = zeros(1,img_num-1);
r = zeros(1,img_num-1); % Radius for circular motion
area = zeros(1,img_num-1);

for n = 1:(img_num-1)
    sum_x=0; sum_y=0; sum_r=0; sum_area=0;

    for i = 1:height1
        for j = 1:width1
            if I2{1,n}(i,j) == 0
                sum_x = sum_x+j;
                sum_y = sum_y+i;
                sum_r = sum_r+((i-i0).^2 + (j-j0).^2).^0.5;
                sum_area = sum_area+1;
            end
        end
    end

    x(1,n) = fix(sum_x/sum_area);
    y(1,n) = fix(sum_y/sum_area);
    area(1,n) = sum_area;
    r(1,n) = sum_r/sum_area;

end

%%%%%%%%%% Plot trajectory %%%%%%%%%%%

for m = 1:(img_num-1)
    imwrite(I2{1,m},[num2str(m), '.tif']);
    imshow(I1{1,m});

    hold on
    plot(x(1,m),y(1,m), '*');
end

%%%%%%%%%% Compute Data %%%%%%%%%%%
X = x'; Y = y'; R = r'; CA = area'
```


Appendix C. Coloured Droplet Detection

```

%%%%%%%%%%%%%% Image process after Appendix I %%%%%%%%%%%%%%%

for k = 1:(img_num-1)
    I2{1,k} = I2{1,k}+0;
end

%%%%%%%%%%%%%% Import Original Images %%%%%%%%%%%%%%%

img_path_list_2 = dir('*.tif');
img_num_2 = length(img_path_list_2);

if img_num_2 > 0
    for pn_2 = 1:img_num_2
        image_name_2 = img_path_list_2(pn_2).name; % Name the images
        img_origin_2 = imread(image_name_2);
        I_2{pn_2} = double(img_origin_2);
        I_red{pn_2} = double(img_origin_2(:,:,1)); % Extract the red-channel
        I_green{pn_2} = double(img_origin_2(:,:,2)); % Green-channel
        I_blue{pn_2} = double(img_origin_2(:,:,3)); % Blue-channel

        % Convert the original images into grey model
        I_2_gray{pn_2}=(I_red{pn_2}+I_green{pn_2}+I_blue{pn_2})./3;

        fprintf('%d %s\n',pn_2,image_name_2);
    end
end

%%%%%%%%%%%%%% Extract the Droplet in a Coloured Model %%%%%%%%%%%%%%%

for k = 1:img_num_2

    % Background matrices
    M_red{1,k} = I_red{1,k}.*I2{1,k}; % Red-channel
    M_green{1,k} = I_green{1,k}.*I2{1,k}; % Green-channel
    M_blue{1,k} = I_blue{1,k}.*I2{1,k}; % Blue-channel

    % Droplet matrices
    Iw_red{1,k} = I_red{1,k} - M_red{1,k}; % Red-channel
    Iw_green{1,k} = I_green{1,k} - M_green{1,k}; % Green-channel
    Iw_blue{1,k} = I_blue{1,k} - M_blue{1,k}; % Blue-channel
    Iw{1,k}(:,:,1) = Iw_red{1,k};
    Iw{1,k}(:,:,2) = Iw_green{1,k};
    Iw{1,k}(:,:,3) = Iw_blue{1,k};
end

%%%%%%%%%%%%%% Extract the Droplet in a Grayscale Model %%%%%%%%%%%%%%%

for k = 1:img_num_2
    Iw_gray{1,k} = I_2_gray{1,k} - I_2_gray{1,k}.*I2{1,k};
end

%%%%%%%% Calculate the Standard Deviation in the Droplet Region (ROI) %%%%%%

for k = 1:img_num_2

    N(1,k) = 0;

```

```
for i = 1:height1
    for j = 1:width1
        if Iw_gray{1,k}(i,j) > 0    % Count the points in the ROI
            N(1,k) = N(1,k)+1;
        end
    end
end
```

```
mean_gray(1,k) = (sum(sum(Iw_gray{1,k}))/N(1,k)); %% Average
```

```
sum_gray(1,k) = 0;
for i = 1:height1
    for j = 1:width1
        if Iw_gray{1,k}(i,j) > 0
            sum_gray(1,k) = ...
                sum_gray(1,k) + ...
                (Iw_gray{1,k}(i,j) - ...
                mean_gray(1,k))^2; %% Standard deviation
        end
    end
end
```

```
SD_gray(1,k) = sqrt(sum_gray(1,k)/N(1,k));
```

```
end
```

```
SD = SD_gray'; %% Compute the data
```

Appendix D. Function Derivation (eq. 5.6)

As described in Section 5.1.2, the total energy of the droplet contains contributions from gravitational, kinetic, and surface tension effects:

$$E = \frac{1}{2}\rho_L g H_L V + \frac{1}{2}\rho_L V v^2 + 2\gamma \left(\frac{V}{H_L} + \frac{V}{w} \right) \quad (5.1b)$$

At a constant droplet volume (V), the gravity term and surface tension term corresponding to height in equation 5.1b do not depend on the droplet width (w). However, the kinetic energy term and surface tension term corresponding to width will depend on the width. The velocity of the droplet's circular motion is calculated as the angular velocity (ω) multiplied by the radius of motion of the droplet (equation 5.7), where the radius (R_n) is a function of the droplet width (w_n) according to equation 5.5.

$$v = \omega R_n \quad (5.7)$$

$$w_n = 2(R_r - R_n) \quad (5.5)$$

Equations 5.7 and 5.5 can be combined and substituted into equation 5.1b:

$$E = \frac{1}{2}\rho_L g H_L V + \frac{1}{2}\rho_L V \omega^2 R_n^2 + 2\gamma \left(\frac{V}{H_L} + \frac{V}{w} \right) \quad (VI.1)$$

When the effective radius of the circular motion is increased from R_n^- to R_n^+ , the droplet width will be decreased from w^+ to w^- . Minimising the increase with $(R_n^+ - R_n^-) \rightarrow 0$:

$$\lim_{(R_n^+ - R_n^-) \rightarrow 0} \frac{\Delta E}{R_n^+ - R_n^-} = 0 \quad (VI.2)$$

Applying equation VI.2 to equation 5.1b:

$$\lim_{(R_n^+ - R_n^-) \rightarrow 0} \frac{\left[\frac{1}{2}\rho_L V \omega^2 (R_n^+)^2 + \frac{2\gamma V}{w^-} \right] - \left[\frac{1}{2}\rho_L V \omega^2 (R_n^-)^2 + \frac{2\gamma V}{w^+} \right]}{R_n^+ - R_n^-} = 0 \quad (VI.3)$$

$$\lim_{(R_n^+ - R_n^-) \rightarrow 0} \frac{\frac{1}{2}\rho_L V \omega^2 (R_n^+)^2 - \frac{1}{2}\rho_L V \omega^2 (R_n^-)^2}{R_n^+ - R_n^-} + \lim_{(R_n^+ - R_n^-) \rightarrow 0} \frac{\frac{2\gamma V}{w^-} - \frac{2\gamma V}{w^+}}{R_n^+ - R_n^-} = 0 \quad (VI.4)$$

$$\lim_{(R_n^+ - R_n^-) \rightarrow 0} \frac{\frac{1}{2}\rho_L V \omega^2 (R_n^+ + R_n^-)(R_n^+ - R_n^-)}{R_n^+ - R_n^-} + \lim_{(R_n^+ - R_n^-) \rightarrow 0} \frac{2\gamma V \frac{w^+ - w^-}{w^- w^+}}{R_n^+ - R_n^-} = 0 \quad (VI.5)$$

Applying equation 5.5 to VI.5:

$$\lim_{(R_n^+ - R_n^-) \rightarrow 0} \frac{\frac{1}{2} \rho_L V \omega^2 (R_n^+ + R_n^-) (R_n^+ - R_n^-)}{R_n^+ - R_n^-} + \lim_{(R_n^+ - R_n^-) \rightarrow 0} \frac{2\gamma V \frac{2(R_n^- - R_n^+)}{w^- w^+}}{R_n^+ - R_n^-} = 0 \quad (VI.6)$$

$$\lim_{(R_n^+ - R_n^-) \rightarrow 0} \left[\frac{1}{2} \rho_L V \omega^2 (R_n^+ + R_n^-) \right] + \lim_{(R_n^+ - R_n^-) \rightarrow 0} \frac{-4\gamma V}{w^- w^+} = 0 \quad (VI.7)$$

At $(R_n^+ - R_n^-) \rightarrow 0$, equation VI. 7 can be simplified with $R_n^+ \sim R_n^-$ and $w^- \sim w^+$:

$$\rho_L V \omega^2 R_n - \frac{4\gamma V}{w^2} = 0 \quad (VI.8)$$

For $R_r \gg w$,

$$w = 2 \sqrt{\frac{\gamma R_r}{\rho_L v^2}} = \sqrt{\frac{2\gamma D_0}{\rho_L v^2}} \quad (5.9)$$

Appendix E. Work Calculation

```
%%%%%%%%%%%%%%%%%%%%%%%%%%%%%%%%%%%%%%%%%%%%%%%%%%%%%%%%%%%%%%%%%%%%%%%%%% Experimental data %%%%%%%%%%%%%%%%%%%%%%%%%%%%%%%%%%%%%%%%%%%%%%%%%%%%%%%%%%%%%%%%%%%%%%%%%%%

v = xlsread('R3_H2O_400C_1300.xlsx',3,'P5:P114'); % droplet velocity
t = xlsread('R3_H2O_400C_1300.xlsx',3,'O5:O114'); % time

%%%%%%%%%%%%%%%%%%%%%%%%%%%%%%%%%%%%%%%%%%%%%%%%%%%%%%%%%%%%%%%%%%%%%%%%%% Curve Fitting %%%%%%%%%%%%%%%%%%%%%%%%%%%%%%%%%%%%%%%%%%%%%%%%%%%%%%%%%%%%%%%%%%%%%%%%%%%

[xData, yData] = prepareCurveData( t, v );

ft = fittype( 'exp2' );
opts = fitoptions( 'Method', 'NonlinearLeastSquares' );
opts.Display = 'Off';
opts.StartPoint = [0.717814231109959 -0.289394786552059 ...
    -0.731495544445136 -1.28396380955242];

[fitresult, gof] = fit( xData, yData, ft, opts );

formula(fitresult);
coeffs = coeffvalues(fitresult);
a = coeffs(1);
b = coeffs(2);
c = coeffs(3);
d = coeffs(4);

%%%%%%%%%%%%%%%%%%%%%%%%%%%%%%%%%%%%%%%%%%%%%%%%%%%%%%%%%%%%%%%%%%%%%%%%%% Droplet displacement over the acceleration process %%%%%%%%%%%%%%%%%%%%%%%%%%%%%%%%%%%%%%%%%%%%%%%%%%%%%%%%%%%%%%%%%%%%%%%%%%%

fun = @(x) a*exp(b*x) + c*exp(d*x); % fitted function
s = integral(fun, min(t), max(t)); % integrate the velocity over time

%%%%%%%%%%%%%%%%%%%%%%%%%%%%%%%%%%%%%%%%%%%%%%%%%%%%%%%%%%%%%%%%%%%%%%%%%% Work done by the driving force %%%%%%%%%%%%%%%%%%%%%%%%%%%%%%%%%%%%%%%%%%%%%%%%%%%%%%%%%%%%%%%%%%%%%%%%%%%

rho_L = 958.4; % liquid density
V = 0.00000001*1300; % droplet volume
a_a = 0.48265; % measured acceleration
Ff = rho_L*V*a_a; % driving force
Wf = Ff*s; % total work

%%%%%%%%%%%%%%%%%%%%%%%%%%%%%%%%%%%%%%%%%%%%%%%%%%%%%%%%%%%%%%%%%%%%%%%%%% Energy loss by the friction work %%%%%%%%%%%%%%%%%%%%%%%%%%%%%%%%%%%%%%%%%%%%%%%%%%%%%%%%%%%%%%%%%%%%%%%%%%%

d1 = 0.104; % numerical coefficient
H_L = 0.001*1.34*((100000000*V-21.9)^0.161); % droplet height
A = V/H_L; % top-down contact area
epsilo = 0.0005; % ratchet height
lambda = 0.00271; % average ratchet period
constant = d1*rho_L*A*(2/3)*epsilo/lambda;

fun_Fb = @(x) constant*(a*exp(b*x) + c*exp(d*x)).*(a*exp(b*x) ...
    + c*exp(d*x)).*(a*exp(b*x) + c*exp(d*x)); % friction model

Wb = integral(fun_Fb,min(t),max(t)); % energy loss

%%%%%%%%%%%%%%%%%%%%%%%%%%%%%%%%%%%%%%%%%%%%%%%%%%%%%%%%%%%%%%%%%%%%%%%%%% Kinetic Energy %%%%%%%%%%%%%%%%%%%%%%%%%%%%%%%%%%%%%%%%%%%%%%%%%%%%%%%%%%%%%%%%%%%%%%%%%%%

v_m = 0.39; % measured terminal velocity
E = 0.5*rho_L*V*v_m*v_m; % kinetic energy
```